Charge Transport in Nanopatterned PbS Colloidal Quantum Dot Arrays

by

Nirat Ray

M. Sc., Indian Institute of Technology, Delhi (2009)

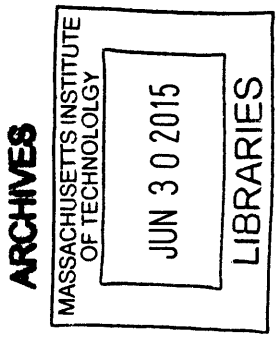

Submitted to the Department of Physics
in partial fulfillment of the requirements for the degree of

Doctor of Philosophy

at the

MASSACHUSETTS INSTITUTE OF TECHNOLOGY

February 2015

Author ..... Signature redacted

Department of Physics
September 24, 2014

Certified by ..... Signature redacted

Marc A. Kastner
Donner Professor of Science
Thesis Supervisor

Accepted by ..... Signature redacted .....

Krishna Rajagopal
Professor and Associate Department Head for Education

Charge Transport in Nanopatterned PbS Colloidal Quantum Dot Arrays

by

Nirat Ray

Submitted to the Department of Physics
on September 24, 2014, in partial fulfillment of the
requirements for the degree of
Doctor of Philosophy

Abstract

In this thesis, we study charge transport in nanopatterned arrays of PbS colloidal quantum dots using conventional two-probe measurements and an integrated charge sensor. PbS dots are synthesized in solution with an organic ligand or cap that serves to passivate the surface of the dot, provide a tunnel barrier as well as colloidal stability. These dots can self assemble into an array as the solvent evaporates from a drop of solution on a surface. The self-assembled arrays can be thought of as tunable artificial solids, where the coupling between the dots can be tuned by changing the ligand.

Using electron beam lithography followed by a lift-off process, we develop a novel technique to nanopattern these arrays and present the first colloidal quantum dot arrays of nanoscale dimensions. Nanopatterning makes it possible to study the electrical properties intrinsic to the dots unimpeded by macroscopic defects, such as cracking and clustering that typically exist in larger-scale arrays. We find that the electrical conductivity of the nanoscale films is higher than that of drop-cast, microscopic films made of the same type of dot. We achieve unprecedented versatility in integrating the patterned films into device structures, which will be valuable both for studying the intrinsic electrical properties of the dots and for nanoscale optoelectronic applications. From two-probe measurements on the nanopatterned arrays that are approximately 15 dots wide, we observe large noise in the current as a function of time. The noise is proportional to the current when the latter is varied by applying source-drain or gate voltage in a field-effect structure or when changing temperature. Owing to the small number of current paths in the system, we often observe telegraph switching, and find that the off times follow non-poissonian statistics. We show that the results can be understood in terms of a model in which a quasi-one-dimensional percolation path is turned on and off, by charging of a dot along the path.

Long organic ligands lead to highly resistive colloidal quantum dot arrays, making the low bias regime inaccessible with conventional two-probe measurements. We use an integrated charge sensor to study transport in the low bias regime as a function of the coupling between the dots. We present transport measurements on butylamine

and oleic acid capped PbS dots. The resistances measured are the highest measured for colloidal quantum dots. For the native oleic acid ligand, and weak coupling between the dots, the conduction mechanism is nearest neighbor hopping, and the conductance is simply activated. At low source-drain bias voltages, the activation energy is given by the energy required to release a carrier from a trap state plus the activation over barriers resulting from site disorder. The barriers from site disorder are eliminated with a sufficiently high source-drain bias. For the shorter ligand, which gives stronger coupling, the data are consistent with Mott's variable range hopping as the conduction mechanism.

Thesis Supervisor: Marc A. Kastner
Title: Donner Professor of Science

Acknowledgments

You know you've reached the end of the long road called 'Ph.D.' when eventually the time comes to write the acknowledgements. The Kastner group has been home to me for the last five years, and it is not without a certain degree of nostalgia that I prepare to hand in my dissertation. I want to take this opportunity to acknowledge all the people who contributed positively to my graduate school experience.

First and foremost, I thank my advisor, Marc Kastner, for accepting me into his group and guiding me at every step. Marc's enthusiasm and unwavering support has been the greatest source of inspiration for me. I admire his deep and intuitive understanding of physics, his unlimited patience, and the faith he has in his students. His mind is like a steel trap and the solution to whatever problem I was facing was, more often than not, something he had read about or experienced years ago. I have particularly enjoyed the last six months that he spent in his building 13 office.

Moungi Bawendi, while not formally an advisor, welcomed me to his group meetings, invited me to present my work, and met me individually to discuss research. I appreciate his deep and sincere value of quality science, and his simultaneous interest in the product market.

I have had the good fortune to work with many talented and fun students and postdocs throughout my time as a graduate student. Kenny MacLean warmly greeted me when I first joined the lab, and was happy to share his knowledge and experience. In the short overlap that we had, he was a fun officemate, and I really enjoyed discussing science and life outside the lab with him. I worked closely with Tamar Mentzel on nanopatterning colloidal quantum dot arrays and part of the noise measurements. I appreciate her enthusiasm, resourcefulness and her extraordinary ability to sell her research. Neal Staley joined our group as a postdoc when I was a third year graduate student. I really enjoyed discussing data with Neal, because he always has good ideas and suggestions for further experiments. He left his office door open for me to barge in with questions, especially while he ate lunch. I am grateful to him for forcing me to think about the story behind data, and appreciate the ingenuity and commitment

he brings to his work. I enjoyed getting to know Jingshi Hu, Colin Dillard, Xi Lin and Andrew Lai.

In the Bawendi group, I worked closely with Darcy Wanger. Darcy has been a joy to work with and I appreciate her integrity and diligence in research. I would also like to thank other people from Moungi's group: Jennifer Scherer, who has been my go to person after Darcy graduated, Gyuweon Hwang (Q1) for making sure the glovebox was in perfect condition and Dorthe for teaching me how to give a good presentation.

The fabrication part for this thesis was done in MITs Microsystems Technology Lab (MTL) and the Scanning electron beam laboratory (SEBL). I would like to thank Vicky Diadiuk and Judy Hoyt for their help and guidance with fabrication. I thank Paul Tierney, Eric Lim, Bernard Alamariu, Paudely Zamora, Bob Bicchieri, Scott Poesse and Dan Adams, not only for training me and helping me in the clean room, but also for being friendly faces (behind the bunny suits). One of the best learning experiences for me has been during the year when I served as a student member of the Process Technology committee (PTC). The nanopatterning aspect of this work would not have been possible without the expert guidance of Mark Mondol. I admire his patience and dedication, as he sat with me for extended periods of time while we perfected the alignment process.

The International Fulbright Science and Technology program and the U.S. Department of State, generously provided my graduate fellowship for the first three years of graduate school. I appreciated the creative and intellectually stimulating gatherings that they organized every year. The last two years of my graduate school were funded by the Schlumberger foundation Faculty for Future fellowship aimed at encouraging women in physics.

While at MIT, I have benefited greatly from the camaraderie and friendship, and many times good food, from the MIT Women in Physics and the the Graduate Women at MIT (GWAMIT). Anne White has been my my faculty mentor for almost two years now. She helped me through some rough patches and I have really enjoyed our long discussions over coffee.

The Physics department has been a welcoming place with great teaching and

faculty who care a great deal about students and research. I really enjoyed the courses taught by Wolfgang Ketterle, Mehran Kardar and Patrick Lee. I am grateful to many staff members at MIT, who helped make life easier at every turn. They include Monica Wolf, Catherine Modica, Jacqueline Carota, Crystal Young, Katie Lewis, Ting Ting Li, Anita Caputo, Annie Lee, Ed Kruzel and Rebecca Maitland.

Much of my initial time at MIT was spent doing problem sets and studying for general exams. I would like to thank Mackenzie Van Camp, Dillon Gardener, Patrick Brown, Laura Popa, Duncan Ralph, and Javier Sanchez-Yamagishi, without whose assistance these times would have been much more difficult, and much less fun.

I must thank my family and my extended family, for their support and encouragement. They may not have had a clue about what I was doing for the last five years, but they were constantly telling me I could do it. Finally, I thank my beloved husband, partner and friend, Guru Saran Mishra, for his constant love and support. None of this would have been possible without him.

Contents

List of Figures

Chapter 1

Introduction

Low-dimensional nanometer-sized systems have defined new research areas in condensed matter physics. When electrons and holes are confined by potential barriers to small regions of space where the dimensions of the confinement are less than the de Broglie wavelength of these charge carriers, pronounced quantization effects develop. The length scale below which strong quantization effects begin to occur ranges from about 5 nm to 25 nm for typical semiconductors. The confinement can take place in one dimension, giving quantum wells, in two dimensions, giving quantum wires, or in all three dimensions, giving quantum dots.

A system of electrons confined in all three dimensions has discrete energy and charge states, just like atoms and molecules, and for this reason quantum dots are also known as artificial atoms. As a simple example, we can think about the particle in a box problem, of a particle free to move in a small space surrounded by impenetrable barriers. By solving the Schrodinger's equation, we get quantized energy levels, and wavefunctions which depend on the details of the confining potential. For a square box of side L with the potential V equal to zero inside the box and infinite outside, the energy levels are given by $n^2\pi^2\hbar^2/2\mathrm{m}^*\mathrm{L}^2$, where, m^* is the effective mass of the particle, and n is a quantum number. In order to observe energy quantization effects in a dot, the thermal energy ($\mathrm{k}_B\mathrm{T}$) must be lower than the internal excitation energy, or the level spacing between the quantized energy levels. For a 10 nm box, the energy level spacing is of the order of an meV, and so to see quantization effects one needs

to go to temperatures below 10 K.

An isolated quantum dot also has a set of well-defined charge states, where each successive charge state corresponds to the addition of one more electron to the dot. Because of the coulomb repulsion between electrons, the energy difference between successive charge states can be very large, and this is given by the charging energy. The charging energy, E_c, can be described by simple electrostatics and is given by $e^2/2C$, where, e is the electron charge, and C is the total electrostatic capacitance of the dot.The charging energy depends on both the size of the dot and the local electrostatic environment. In general, the charging energy must be calculated for the specific geometry. For an isolated sphere of radius r, and dielectric constant ϵ, the charging energy is given by $E_c = e^2/8\pi\epsilon_0\epsilon r$. To observe charge quantization effects, the charging energy must be larger than the thermal energy. For a spherical dot of diameter 10 nm, and dielectric constant of unity, the charging energy comes out to be 0.2 eV. This exceeds $k_BT = 26$ meV at room temperature, indicating that thermal fluctuations in the charge of the dot will be suppressed. Charging effects are also destroyed if the tunneling rate between the dot and the electrodes is too rapid. Simple estimations from the uncertainty principle show that for resistances below h/e^2, where h is the Planck's constant and e the electron charge, quantum fluctuations smear out charging effects.

Broadly speaking, quantum dots can be fabricated in two ways. There are epitaxial quantum dots that are defined by electrostatic gates on substrates, or that self-assemble on surfaces. In the most common approach to form epitaxial dots, we start with a GaAs/AlGaAs heterostructure, in which a 2DEG forms a distance below the surface. The 2DEG is then patterned to form isolated islands, either by etching through the 2DEG, or by electrostatic patterning metal gates on the substrate surface. For the work presented in this thesis, we work with colloidal quantum dots fabricated using 'wet' methods which provide excellent control over size and shape.

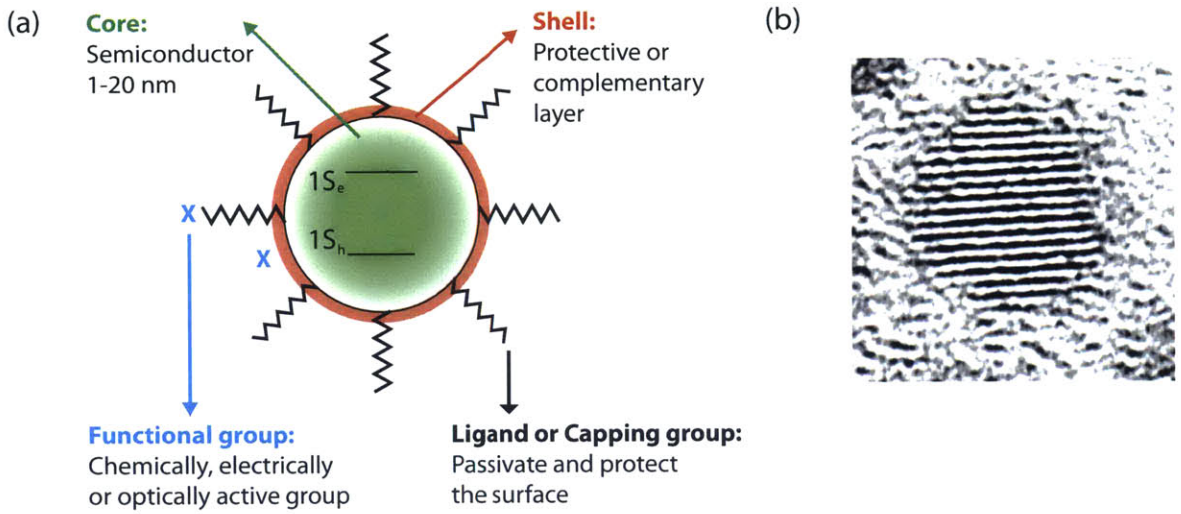

Figure 1-1: (a) Cartoon of a colloidal quantum dot. (b) High resolution Transmission electron micrograph of a PbSe dot showing the crystal structure of the dot. Image taken by Darcy Wanger from Bawendi group.

1.1 Colloidal quantum dots

A single colloidal quantum dot consists of a semiconducting or metallic core with a diameter of a few nanometers, capped by an organic material, or ligand, which serves to passivate the surface of the sphere, and to insulate the dot from its surroundings. The dot may contain a thin complementary shell of another material or other chemically, electrically or optically active groups. Figures 1-1(a) and (b) show a cartoon of a colloidal quantum dot, along with a high resolution transmission electron micrograph of a PbSe colloidal dot.

The core of a colloidal dot may be metallic (such as Al, Au, Fe), or semiconducting (such as CdS, PbSe, PbS). For metallic dots, the spacing between energy levels depends on the Fermi energy of the metal, E_F, and on the number of electrons, N, as:

$$\Delta\epsilon = 1/D(E_F) = 4E_F/3N \tag{1.1}$$

For Au with a work-function of 5.5 eV, a dot with a radius of 2 nm has level spacing of the order of 2 meV, requiring sub-kelvin temperatures for measurement of internal excitation energies. The small level spacing compared to the large charging energy resulting from the small dot size, implies that the addition of electrons in metallic

dots is dominated by the charging energy. A semiconducting dot can be described, to a very good approximation, by a particle in a spherical box. For a spherical well with zero potential inside the box (r < R) and infinite outside, the Hamiltonian gives eigenergies as:

$$E_{n,l,m} = E_{n,l} = \frac{\hbar^2 \beta_{n,l}^2}{2m^* R^2} \tag{1.2}$$

where, m^* is the effective mass of the particle, and R is the radius of the box. The coefficient $\beta_{n,l}$ is the n^{th} zero of the l^{th} spherical Bessel function. The quantum numbers n, l and m are the same as used in the atomic notation of states, for example, n = 0, l = 0 would be the 1S state. For a CdSe dot ($m^* = 0.13\ m_e$), with a radius of 2 nm the estimated spacing between energy levels (1S and 1P) is approximately 1 eV, making it possible to observe quantization effects even at room temperature.

The most common ligand coatings described in literature are based on organic hydrocarbon molecules. The ligands used for synthesis typically have a small head group (such as a carboxylic acid) that has a high affinity for the dot surface, and a long tail to provide sterical stabilization in solution. Bulky organic ligands with long tails act as highly insulating barriers between dots, hindering charge transport. The complete removal of organic surface ligands has proven to be very difficult, and can lead to dangling bonds on the surface as well as trap states [51]. Therefore, a simple exchange of the original bulky ligands by smaller molecules is a widely used approach for improving charge transport. While these lead to smaller tunnel barriers, they also lead to decreased colloidal stability of the dots, and is typically not performed in solution. The ligands can be exchanged to molecules with the same head group and a shorter tail, or to molecules with different head groups [104]. Cross-linking of dots using bi-functional ligands provides another approach to reduce the inter-particle separation, strengthen electronic coupling between dots, or attach them to electrodes or surfaces. The original long chain organic ligands can also be replaced by inorganic ligands such as soluble molecular metal chalcogenide complexes (MCCs). An attractive feature of MCCs is their facile thermal decomposition to metal chalcogenides, which not only further decreases the inter-dot spacing, but can

also create a layer of conductive 'glue' between the dots [50].

It was recently shown that ligands can also provide an additional level of control over the electronic properties [11]. The band energies of colloidal dots can be modified by ligand exchange, resulting in energy level shifts of up to 0.9 eV, as seen from ultraviolet photoelectron spectroscopy (UPS) measurements on PbS dots with different ligands. The trends in energy level position between different ligands have also been confirmed by atomistic modeling, showing that the observed shifts result from contributions from the dipole moment of the ligand as well as the dipole-surface interaction.

Significant progress has also been achieved in the synthesis of core-shell quantum dots [104], obtained by growing a uniform layer of shell material around the colloidal dot. In the case of epitaxial semiconductor-semiconductor core-shell dots, the choice of materials for the core and the shell allows for controlling the confinement of electron and hole wave functions, which, in turn, determines their optical and electronic properties. The shell can serve to protect the core from oxidation.

1.1.1 Optical properties

For a semiconducting dot, both the electron states in the conduction band and the hole states in the valence band are quantized. Figure 1-2(a) shows a schematic of the density of states for a bulk semiconductor as compared to a semiconductor quantum dot. Starting from a continuum of density of states in the bulk, as the size of the dot decreases, the separation between energy levels increases, and it increases more dramatically near the band edge. The states near the center of the band are still close enough to be considered continuous. Quantization effects can be seen from the optical absorption or emission from colloidal dots, as the absorption/emission intensity becomes concentrated at specific frequencies corresponding to the transitions between discrete states. Figure 1-2(b) shows a schematic of the optical absorption from a bulk semiconductor (black dashed line) and from a semiconducting dot. The absorption spectrum of a bulk semiconductor is continuous, but in a dot it consists of a series of discrete transitions with very high absorption intensity at the transition

frequencies, and this has motivated researchers to create lasers [6].

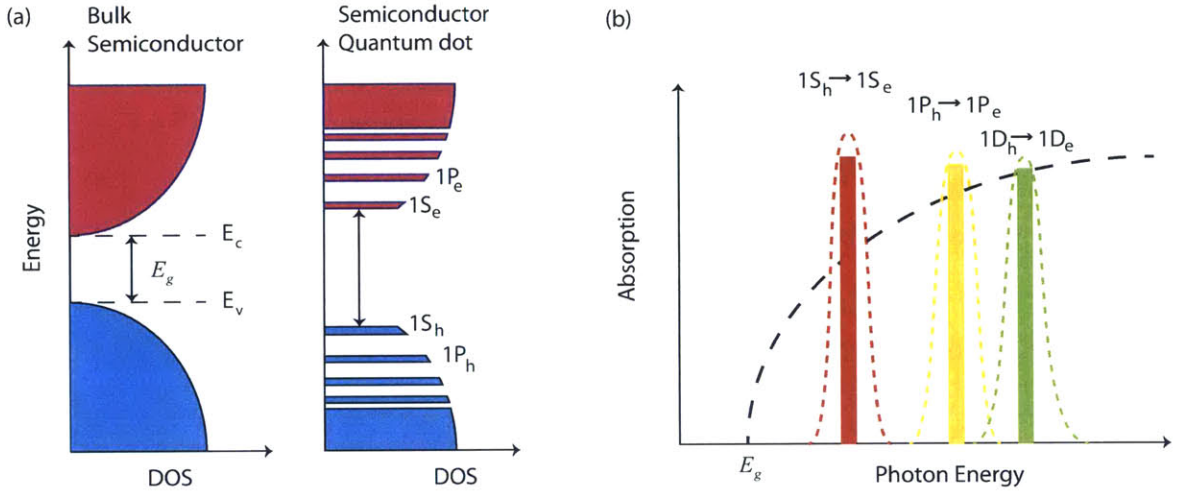

Figure 1-2: Schematic of (a) density of states for a bulk semiconductor as compared to a semiconductor quantum dot. Starting from a continuum of density of states in the bulk, as the size of the dot decreases, the separation between energy levels increases. The increase is more dramatic near the band edge, and the states at the center of the band may still be considered to be continuous. (b) absorption spectrum of a bulk semiconductor (black dashed line) compared to that of a semiconductor quantum dot. The absorption spectrum of a bulk semiconductor is continuous, but in a dot it consists of a series of discrete transitions with very high absorption intensity at the transition frequencies.

From studying optical properties of these dots, one can differentiate between weak and strong confinement regimes [24] by comparing the Bohr exciton radius, a_B, given by $\hbar^2\epsilon/\mu e^2$, where μ is the exciton reduced mass and ϵ is the dielectric constant of the semiconductor, with the dot radius, r. When the dot radius is much larger than the exciton radius, then the binding energy of the exciton is much larger than the quantization energy of both electrons and holes. The optical spectra is then determined by the exciton center of mass. This regime is the weak confinement regime ($r>>a_B$). When the dot radius becomes much smaller than the exciton radius ($r<<a_B$), the optical spectra can be considered as transitions between electron and hole levels as shown in Figure 1-2(b). Given the small exciton radius of $\approx$10 nm in typical semiconductors, it not easy to achieve the strong confinement limit. However, quantum dots of lead salts (PbS, PbSe, and PbTe) are very well suited for the study of this limit, and all the data presented in this thesis are on studies of PbS dots.

1.1.2 PbS quantum dots

Bulk Lead Sulfide (PbS) is a narrow bandgap semiconductor, with a band gap of approximately 0.37 eV at room temperature. It crystallizes in the rock salt structure, and has a very large static dielectric constant of approximately 169 at room temperature [18]. It has equal electron and hole effective masses of 0.25 m_e. The Bohr exciton radius comes out to be approximately 20 nm making it easier to access the strong confinement limit. The similarly small electron and hole masses for PbS also imply large confinement energies, split about equally between carriers. Large level spacings, also imply that the energy level spectra for these dots is simple, as opposed to the spectra of CdS, CdSe or other II-VI semiconductor dots, where the close level spacing and valence band mixing lead to complications [123].

There are multiple ligands and core/shell structures compatible with PbS dots. Oleic acid is used for synthesis, and this can be exchanged to butylamine or thiol based ligands. Cross-linking with short-chain dithiols has been demonstrated to improve the photoconductive properties of PbS arrays [48]. Using thiocyanate based ligands, ambipolar transport has also been observed in PbS nanocubes [47].

The dots used in this work are 4.3 to 4.6 nanometers in diameter. The dot size can be roughly estimated from the optical absorption peaks, and subsequently verified by TEM and X-ray diffraction measurements [117]. The optical absorption shows a peak at a wavelength of 1395 nm, which puts the band gap in the infrared. The full width at half maximum at this wavelength of 110 nm, can be roughly considered to be coming from distribution of site energies of dots in the colloidal solution. The origin of the disorder is the finite size distribution of the dots. The confinement energy, estimated from a particle in spherical box model, is approximately 300 meV.

We can extract the charging energy as $e^2/8\pi\epsilon_o\epsilon r$, where r is the dot radius and ϵ is the dielectric constant of the dot. The dielectric constant of colloidal dots may be roughly estimated by volume weighted average of the ligand and the semiconductor material [21]. Because bulk PbS has a high static dielectric constant, there is a large contrast between component dielectric constants in PbS dots. This high bulk

dielectric constant also suggests that increasing the volume fraction of dot, for example by shortening the spacing between dots by attaching a shorter ligand or using larger dots, could result in a large increase in the effective dielectric constant. From a volume average of a three dimensional close-packed array, we estimate the effective dielectric constant of PbS dots as:

$$\epsilon_{av} = \epsilon_r + (\epsilon_{PbS} - \epsilon_r)\eta \tag{1.3}$$

where, ϵ_r is the dielectric constant of the ligand, ϵ_{PbS} is the dielectric constant of bulk PbS. and η is the packing fraction. For $\epsilon_r \approx 5$, and $\epsilon_{PbS} = 169$, we find $\epsilon_{av} \approx 87$. The charging energy for a dot radius of ≈ 2.2 nm is then estimated to be approximately 4 meV. As the charging energy scales inversely with the dielectric constant, it is very sensitive to errors in the estimation of the dielectric constant. Our collaborators in the chemistry department explicitly measured the dielectric constant of butylamine PbS dots in a capacitor geometry, and find a dielectric constant of 12. They also find that the observed values of dielectric constants for colloidal dots do not agree with those estimated by simple effective medium theories [117]. From this dielectric constant, we estimate a charging energy of 23 meV for butylamine capped dots. For a more detailed discussion on estimating the dielectric constant, we refer the reader to work by D. Wanger from the Bawendi group [117].

1.2 Quantum dot arrays and superlattices

Starting from a quantum dot as an artificial atom, we can think about building artificial two and three dimensional arrays, or artificial solids, using the dots as building blocks. The properties of such a solid are defined in terms of the energy levels of the individual dots, the bonding, or coupling, between dots, and their structural arrangement or packing. In an artificial solid, all of these properties are tunable. As discussed earlier in the chapter, the energy levels of a dot can be tuned by changing the size of the dot. The bonding and structural arrangement is controlled by the ligand, and

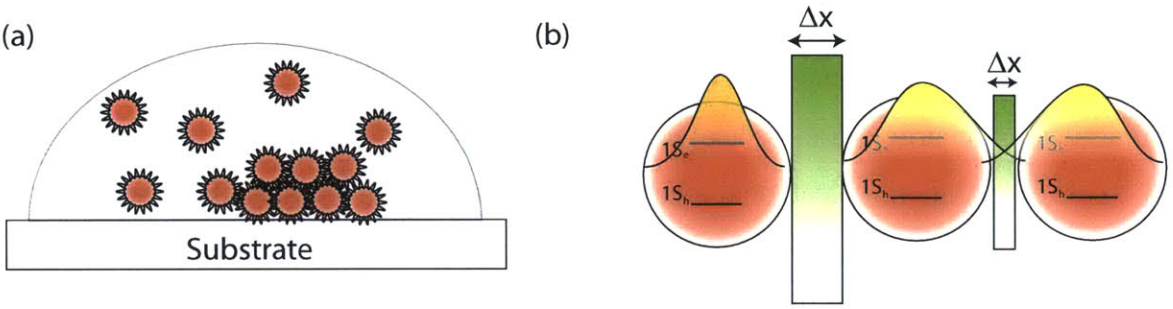

Figure 1-3: (a) From colloidal dots to arrays. A small volume of the colloidal dispersion is dropcast onto a surface, and the solvent is allowed to slowly evaporate. The rate of solvent evaporation coupled with the inter-dot forces determines the ordering length scale in the system, leading to the formation of a two or three dimensional 'artificial solid'. (b) Unlike classical solids, artificial solids are tunable. We can tune the energy levels of each dot by changing the size of the dot. We can tune the inter-dot coupling by modifying the height and width of the tunnel barrier, Δx, by changing the ligand or capping molecule attached to the dot.

the resulting inter-dot interactions. The tunability has created enormous interest in the scientific community to create designer solids. In recent years, significant advances have been made to use these building blocks to create ordered superstructures [15, 98, 91, 112, 113, 20].

The formation of superlattices, with long range order, in general occurs via self assembly guided by entropy and weak interparticle forces. The simplest approach to form arrays and superlattices is to dropcast a small volume of dots onto a substrate and then allow the solvent to slowly evaporate from the dispersion with a narrow size distribution [76]. The rate of solvent evaporation, and the inter-dot interaction then determine the order, with slow evaporation and long ligands favoring long range order.

In contrast to indistinguishable atoms in a solid, no two colloidal dots are truly identical. There may be small experimental variations in size, shape, ligand coverage and so on. This variability introduces disorder energy in a quantum dot array. As the energies of occupied and unoccupied states in semiconductor quantum dots, scale approximately as $1/r^2$, the dispersion in site energies is proportional to $2\Delta r/r$. Another type of disorder, which is very common to quantum dot arrays is packing disorder.

Besides overcoming the charging energy of each dot, to travel between dots, charges must also traverse the tunnel barriers created by the ligands. This gives an additional energy scale associated with the coupling between dots. In the regime of weak coupling, the electronic structure of an array can be described by discrete quantum confined wave functions localized on individual particles. In the strong coupling regime, wave functions from neighboring dots can interact, giving rise to delocalized states over a small portion or entirety of the array. In literature, the associated energy scales is estimated as, $\beta \approx h\Gamma$, where β is the coupling energy, h is the Planck's constant and Γ is the tunneling rate between neighboring dots [104]. The tunneling rate can be approximated by:

$$\Gamma \approx exp(-2\sqrt{(2m^*\Delta E/\hbar^2)}\Delta x) \tag{1.4}$$

where ΔE and Δx are the height and width of the tunnel barrier respectively.

If the barriers between dots are sufficiently small, the quantum dot array is analogous to a covalently bonded solid, even though the coupling ligand itself is much more complex than a single bond. For ionic coupling, we need Coulomb interactions between neighboring dots. This has led to the evolution of binary superlattices of dissimilar quantum dots.

1.2.1 Binary superlattices

Combining two types of dots (semiconducting and/or metallic dots), has lead to the formation of binary nanoparticle superlattices or BNSLs, with a very rich phase diagram and multiple close packed and non-close packed phases [98]. To determine the symmetry or the packing of these superlattices, transmission electron microscopy or small angle x-ray diffraction is used [99]. BNSLs isostructural with known salts or intermetallic compounds have been found. Figure 1-4 shows a superlattice formed with core-shell PbS/CdS and CdSe/ZnS dots 4 nm and 8 nm in diameter.

Self-assembly of dots is a general phenomenon, and to understand its origin, we

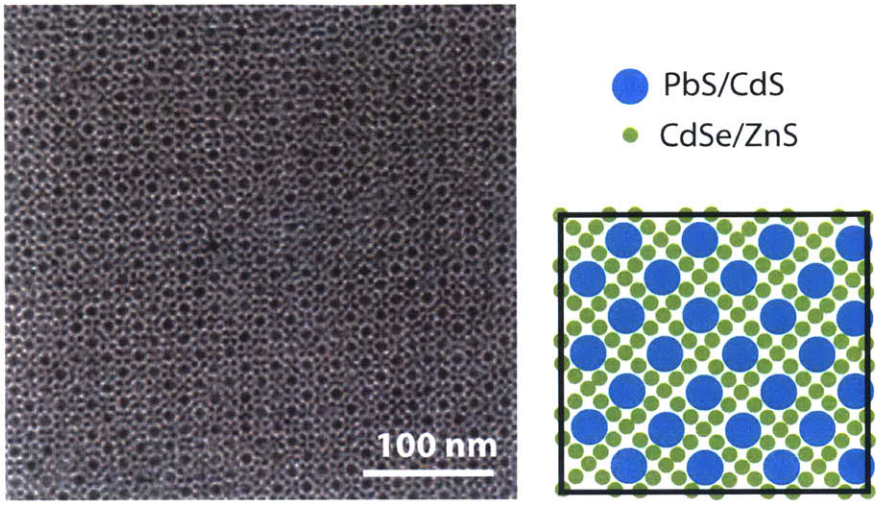

Figure 1-4: Transmission electron micrograph and model of a binary nanoparticle superlattice (BNSL) self-assembled from core-shell 4 nm and 8 nm PbS/CdS and CdSe/ZnS quantum dots. Image taken by Gyuweon Hwang from the Bawendi group.

consider the free energy during formation of a superlattice:

$$\Delta F = \Delta U - T\Delta S \tag{1.5}$$

where, F is the Helmholtz free energy, U is the internal energy and S is the entropy of the system. The change in internal energy is determined by inter-dot interactions, and may be dominated by Van Der Waals, electrostatic or steric forces. The entropic term, ΔS, favors the formation of the densest packing for a given combination of dots. It favors the formation of a binary superlattice if the packing density is comparable or exceeds the density of large and small dots packed separately [104]. Therefore, for certain structures the entropy alone can stabilize these binary structures with long range order. The addition of interparticle forces can further stabilize low-density structures with efficient interactions between dots. The temperature can be used to adjust the relative weights of the internal energy and entropic terms in Equation 1.5, and typically, less dense structures are obtained at low temperatures.

Many key features of ordinary crystals, such as faceting, twinning, polymorphism, and defects, have been observed in these superlattices, suggesting that their assembly follows the same fundamental principles as crystallization of conventional solids.

Recently, it was shown how an ensemble of dots could assemble with quasi-crystalline order and crystallographically forbidden 12-fold symmetry [106]. Studies of the self-assembly of quasi-crystalline superlattices can provide insight into the formation of the quasi-crystal phase in atomic systems [114].

1.3 Electronic coupling and charge transport in quantum dot arrays

In the previous section, we discussed building complex, tunable, two and three dimensional assemblies, using colloidal dots as engineered nanoscale building blocks. If we could control the tunneling rates between dots in an array, we could create an artificial Mott-Hubbard system, and gain a deeper insight into correlated electron physics. The fundamental building blocks for devices are also assemblies or arrays of dots, and so, in order to transform them into competitive functional materials, one has to address the important fundamental problem of transport between individual dots. In this section, we provide a brief overview of the important energy scales in quantum dot arrays, and present a literature survey of the different transport mechanisms reported in colloidal dot arrays.

The properties of a given array of dots, are determined by the interplay of the coupling energy, β, charging energy, E_c, of the individual dots, and the disorder energy of the array, $\Delta\alpha$. For low disorder, if the coupling strength is much smaller than the charging energy of each dot, the array behaves as a Mott insulator. On the other extreme, when the disorder energy dominates, the coupling strength is not large enough to overcome the disorder in site energies throughout the array, and there is a transition from delocalized to localized electronic states, or Anderson localization. Delocalized electronic states can exist at a given temperature only if the inter-dot coupling, β, dominates the thermal energy, k_BT, and the disorder energy, $\Delta\alpha$. Figure 1-5(a), shows the rich phase diagram expected for arrays of dots, adapted from Remacle and Levine [92].

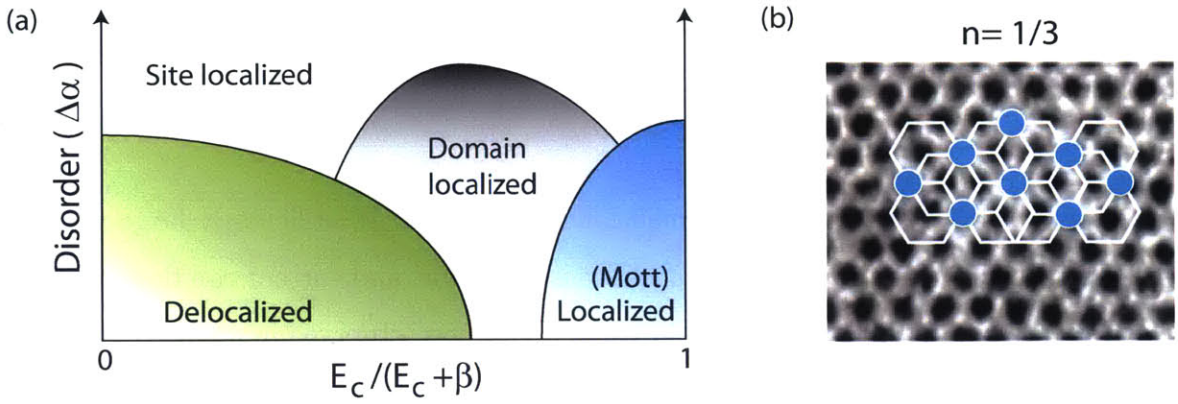

Figure 1-5: (a) A phase diagram showing the different coupling regimes expected for a quantum dot array with size and/or packing disorder. The vertical axis is a measure of the disorder energy, and the x-axis is the dimensionless parameter $E_c/(E_c + \beta)$, where E_c and β are the Coulomb charging energy and the inter-dot coupling energy, respectively. For large disorder, weak electronic coupling can lead to Anderson localization. Reducing the disorder allows for the inter-particle couplings. At very small disorder, Coulomb effects dominate with a Mott-like transition from a delocalized to a site-localized state. Figure adapted from [92]. (b) Colloidal dots can self assemble into ordered 3D closely packed colloidal crystals, with the structure of stacked 2D triangular lattices, as shown in the transmission electron micrograph of PbS dots. Collective or commensurate charge ground states have been predicted to form in these triangular arrays for special densities such as 1 electron for every 3 dots [83], as shown sketched over the TEM image of a PbS quantum dot array. Blue circles depict an electron and white lines highlight the underlying array structure.

Colloidal dots typically self assemble into stacks of two dimensional triangular lattices, as shown in Figure1-5(b). One of the most exciting predictions about electron transport in the frustrated geometry of a triangular lattice is that of Novikov et al. [83]. The authors consider a two dimensional triangular array of quantum dots with a variable electron density in the range 0 to 1/2 electron per dot. The conductivity at the density n = 1/3 decreases more strongly with decreasing temperature than at nearby densities, suggesting the formation of a collective state or a commensurate charge density wave. Figure 1-5(b) shows a sketch of the arrangement of electrons on the triangular array of quantum dots at this density, adapted from reference [83]. Collective charge transport has also been studied theoretically, by Middleton and Wingreen [71] for arrays of small metallic dots. They predict that at temperatures well below the charging energy of a dot, disorder leads to a threshold for conduction,

and the low bias conductance is suppressed by Coulomb blockade. The current is then given by:

$$I \approx (V/V_T - 1)^{\varsigma} \tag{1.6}$$

where $\varsigma = 1,5/3$ for one and two dimension respectively. At sufficiently large applied bias voltage, $V > V_t$, the Coulomb blockade is overcome, and current can flow through the array. The existence of a threshold voltage, has been observed in arrays of metallic [9, 2], and semiconducting dots [94].

For a vast majority of colloidal dot systems, disorder is the the dominant energy scale, and so, the observed transport mechanisms are similar to those observed in disordered and doped semiconductor systems. The different mechanisms can, in principle, be experimentally distinguished by studying the temperature dependence of the conductance. For phonon assisted hopping to nearest neighbor sites, the conductance has an Arrhenius form, $G \propto \exp(-\Delta E/T)$. At lower temperatures, hopping to a dot that is not the nearest neighbor may be energetically more favorable even though the hopping distance is larger. This is the variable range hopping regime and is characterized, if the density of localized states is constant, by a temperature dependence of $G \propto \exp(-T^*/T)^{1/\nu}$, where $\nu = 2,4$. The $\nu = 4$ exponent characterizes Mott's variable range hopping. If Coulomb correlations play an important role, then an exponent of $\nu = 2$ is observed, corresponding to Efros-Shklovskii (ES) variable range hopping, in a Coulomb gap. Typically Coulomb interactions become more important at lower temperatures, and so a crossover from Motts variable range hopping to ES hopping is expected as the temperature is lowered. Literature shows a relatively large variation of transport properties for semiconducting quantum dots. Thermally activated (Arrhenius) behavior [70], and a crossover from thermally activated to ES variable range hopping [42] has been reported for annealed and thiol capped PbSe dots respectively. A transition from nearest neighbor to ES hopping, and from Mott's variable range hopping to ES variable range hopping has also been reported for CdSe dots [126, 57]. Trapping of mobile carriers in poorly passivated surface states is an important consideration in the charge transport through quantum dot arrays, and this was shown by

Ginger and Greenham for CdSe dots [29]. Power law decays of the current and highly non-ohmic conduction, similar to dispersive transport in amorphous semiconductors has also been observed in arrays of CdSe dots [21, 73]. A novel model of transport based on Levy statistics has been proposed to explain the power law current transients [82].

There has been interest in trying to achieve bulk type carrier transport through minibands formed due to strong interparticle coupling, also known as the Bloch regime. Accessing this regime has been complicated by the experimental challenges associated with achieving sufficient inter-dot coupling, low density of electronic traps and low energetic disorder. In contrast to thermally activated hopping, band-like transport through delocalized states is characterized by a decreasing mobility with increasing temperature. Band-like transport has been recently reported for all inorganic CdSe arrays [55]. The authors report an effective inter-dot resistance of 55kΩ, which is comparable to the conductance quantum.

1.4 From fundamentals to device applications

A large motivation for studying the fundamental properties of colloidal quantum dot arrays has been to bring these materials into the arena of practical applications and enable them to successfully compete with existing technologies. Applications of colloidal dots include, but are not limited to, solar cells, light emitting diodes, photodetectors, field effect transistors, thermoelectric devices, and biomarkers. We refer the reader to the recent review by Talapin et. al. for an extensive overview of the applications for colloidal dot systems [104], and in this section we focus our attention on the applications of PbS dots.

Near-infrared PbS quantum dots have emerged as promising candidates for photovoltaic applications because of a tunable energy bandgap that covers the optimal bandgap range for single and multi-junction solar cells. Advances in surface passivation, particularly through the use of halide ions as inorganic ligands, has led to rapid improvements in solar cell power conversion efficiencies. By engineering the

band alignment using different surface ligands and photovoltaic device architectures, certified efficiencies of 8.5 % have been achieved [14, 53]. The impressive solar-cell performance comes, in part, from mastering the surface chemistry of the dots and understanding the relationship between surface functionalization and electronic properties.

Another area where PbS dots have a lot of potential is for use as infrared photodetectors. While there are a large variety of sensitive photon detection systems operating in the visible spectral range, available infrared detectors are either too expensive or insensitive. Infrared photodetector sensitivity is quantified by the normalized detectivity measured in units of Jones (cm $Hz^{1/2}W^{-1}$). Using butylamine capped PbS dots, ultra-sensitive photodetectors have been made with a detectivity of 1.8×10^{13} Jones at 1.3 micron at room temperature, almost an order higher than the detectivity of today's highest performance photodetectors [49, 65]. The ultimate limit to the sensitivity of photodetectors is noise, and a careful examination of noise sources in these dots would enable further improvements in this direction.

Initially used as a research tool to study transport in closely packed quantum dot thin films, field effect transistors with quantum dots as the active layer, have recently experienced a breakthrough in performance (achievement of mobilities higher than 30 $cm^2V^{-1}s^{-1}$) as a result of a proper choice of surface ligands and/or improved chemical treatment of the arrays during device processing. For an overview of these developments, we refer the reader to a recent review on quantum dot field effect transistors [31].

1.5 Thesis overview

In this thesis, we attempt to study transport in nanopatterned colloidal quantum dot arrays. All transport measurements in literature have been on macroscopic arrays, where typically annealing or ligand exchange procedures are employed to improve the conductance. These post deposition treatments typically lead to clustering and cracking in the films, which have the potential to decrease the efficiency of charge

transport in quantum dot films. It also makes it impossible to study the charge dynamics intrinsic to the dots and is thus a barrier to realizing colloidal dot-based designer solids.

In Chapter 2, we present our creation of the first colloidal quantum dot films of nanoscale dimensions that are electrically conductive and crack-free. These films make it possible to study the electrical properties intrinsic to the dots unimpeded by defects such as cracking and clustering that typically exist in larger-scale films. Our technique for forming the nanoscale films is based on electron beam lithography and a lift-off process. The patterns have dimensions as small as 30 nm, and can be lithographically positioned with nanoscale precision. We achieve unprecedented versatility in integrating these nanopatterned structures into device structures both for studying the intrinsic electrical properties of the dots and for nanoscale optoelectronic applications. We find that the electrical conductivity of the nanoscale films is 180 times higher than that of drop-cast, microscopic films made of the same type dot.

By removing this macroscopic component of the structural disorder in a quantum dot arrays, in samples that are 80 nm wide, we are able to reveal the electrical properties intrinsic to the arrays. We report electrical measurements of nanopatterned arrays free of large-scale structural defects and discover that charge is transmitted in discrete time intervals, which is described by Levy statistics. This insight into the mechanism of charge transmission in an array of dots is an essential step toward accessing the predicted complex electron and spin behavior in these systems. In Chapter 3, we present a characterization of the noise in nanopatterned quantum dot arrays in the context of a model in which a quasi-one-dimensional percolation path is turned on and off, by charging of a dot along the path.

In Chapter 4, we use an integrated charge sensor to study transport in the array. Integrated charge sensors have been extensively used to study slow electron dynamics in systems where the current is immeasurably small, such as in the tunneling of single electrons on and off quantum dots. Recently, the ability to measure slow electron dynamics has been exploited to probe transport in highly resistive materials, for which traditional transport techniques fail [62]. The measurement of high resistances,

achieved by a time resolved measurement of charge diffusing through the material, has also been shown to be insensitive to contact effects such as blocking contacts [68]. The integration of quantum dot arrays with the charge sensor is facilitated by our novel nanopatterning technique. The integrated charge sensors can also be used to detect conductance fluctuations in the nearby nanopatterned arrays.

We extend the measurement technique to characterize the electronic properties of PbS quantum dots with different inter-dot couplings. We are able to measure resistances as high as 10^{18} Ω using only moderate voltages. To our knowledge, these constitute the highest resistances measured on these artificial colloidal solids. While transport measurements have been performed on semiconducting colloidal dots with a variety of ligands, the transport characteristics of the dots with the native ligands have never been measured without annealing or sintering the arrays, due to extremely weak coupling between the dots. We present the first transport measurements on nanopatterned PbS arrays with the native oleate ligand. We then study the effect of increasing the effective electronic coupling between the dots in a similar manner. Our technique allows us to probe a variety of transport phenomena including the temperature and field dependence of the current in the arrays.

We find that holes are the majority carriers for these arrays and for weak inter-dot coupling, the conductance follows an Arrhenius behavior with an activation energy that can be modulated by an electric field established by a source drain bias. Our results in this regime are understood by a simple model of release of a carrier from a trap state and nearest neighbor hopping. As the coupling strength between dots is increased by reducing the size of the ligand, we find that the data no longer fits to simply activated transport, and we observe the onset of variable range hopping at lower temperatures.

In Chapter 5, we discuss the broader implications of the work and present ideas for future experiments.

Chapter 2

Synthesis, nanopatterning and characterization of PbS colloidal quantum dots

In this chapter, we discuss the technique we have developed for nanopatterning colloidal quantum dots. We describe the general method for synthesis of colloidal dots, and the specific steps for synthesis of PbS dots in section 2.1. In Section 2.2, we motivate the need for nanopatterning colloidal dots. In Section 2.3, we briefly overview the existing techniques for patterning colloidal dots. In Section 2.4, we describe our patterning technique in detail. In Section 2.5, we discuss the compatibility of our technique with different capping agents or ligands associated with colloidal dots. In section 2.6, we characterize our patterned films and discuss steps to improve the quality of the film, such as surface treatment for the substrate. Finally, in section 2.7, we discuss the improvement in the conductivity of the patterned films as compared to unpatterned films. Parts of this work also appear in T. S. Mentzel *et al.* [69].

2.1 Chemical Synthesis of Colloidal quantum dots

The preparation of nearly monodisperse organically passivated dots is essential for studying properties inherent to nanoscale structures as opposed to those associated

with structural heterogeneity or polydispersity. The term monodisperse in colloidal chemistry is used for dots with a standard deviation $\sigma \leq 5\%$ in diameter.

The synthesis of monodisperse dots, requires a short nucleation event followed by a slower controlled growth of the nuclei. The short nucleation burst is created by a rapid addition of reagents to a heated reaction vessel. The rapid addition of reagents, lowers the temperature to below threshold for nucleation, and no new nuclei form after a short amount of time. As the growth of any one dot is similar to all the others, the initial size distribution is determined by the timescale of growth and nucleation. Figure 2.1(a), shows a sketch of the nucleation and growth process as a function of time. At time, t = 0, the precursors are injected rapidly into the solution to create the short nucleation burst.

Colloidal dots are stable with respect to aggregation only if there exists a repulsive force of sufficient strength and range, to counteract the van der Waals attraction between the dots. Ligands, or capping molecules are present in solution as stabilizing agents during growth to prevent aggregation and precipitation of dots. During growth, the ligands come on and off the surface of the dots at a rapid rate set by the temperature. Ligands can affect the shape of the dots, as they may bond more readily with certain crystal planes, resulting in faster growth on crystal planes poorly passivated with the ligand. If the growth phase continues for longer periods of time, one observes a second growth phase called Ostwald ripening. In this process the high surface energy of the smaller dots promotes their dissolution, and the larger dots grow in size. The average dot size can then increase over time accompanied by a decrease in the total number of dots, and controlled ripening can lead to the preparation of a size series of dots.

Once the desired size is reached, the reaction vessel is cooled to room temperature, to terminate any further growth. The next step is a size selective precipitation, which involves the addition of a non-solvent into the dispersion, to narrow the size distribution. The introduction of a non-solvent, miscible with the original dispersing solvent, destabilizes the dispersion, causing the dots to aggregate and precipitate out of solution, leaving many of the synthetic by-products in solution. As the largest

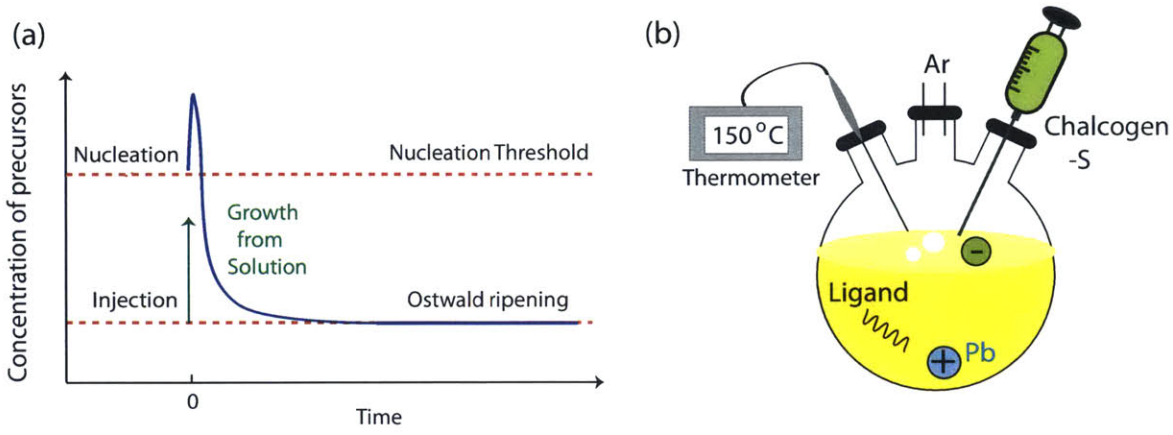

Figure 2-1: (a) Sketch depicting the nucleation and growth phases in the synthesis of monodisperse colloidal quantum dots. (b) Cartoon of the apparatus used for the synthesis of Oleic acid capped PbS colloidal quantum dots.

dots exhibit the largest attractive forces, they aggregate before the smaller ones, and partial flocculation and subsequent filtering and centrifuging can isolate a precipitate enriched in the larger size. The precipitate is re-dispersed in a solvent and subjected recursively to this procedure to further narrow the size distribution, and also get rid of other impurities.

Synthetic organic techniques can be used to tailor the ligands attached to dots after growth. The procedure known as ligand exchange involves a repeated exposure of the dots to an excess of a competing ligand or capping group, followed by precipitation to isolate the partially exchanged dots. This recursive approach can be used to cap dots with a wide range of chemical functionalities, even if the binding of the new cap is less favorable than the original [76].

2.1.1 Synthesis of PbS dots

For synthesis of PbS dots, we start with a Pb precursor in a flask, and a Sulfur compound in solution in a syringe, as shown in Figure 2.1(b). The Pb precursor is prepared by dissolving and degassing 11.38 gm of Lead Acetate in a mixture of 270 ml Oleic acid (which also serves as the ligand) and 30 ml of 1-Octadecene (ODE) at

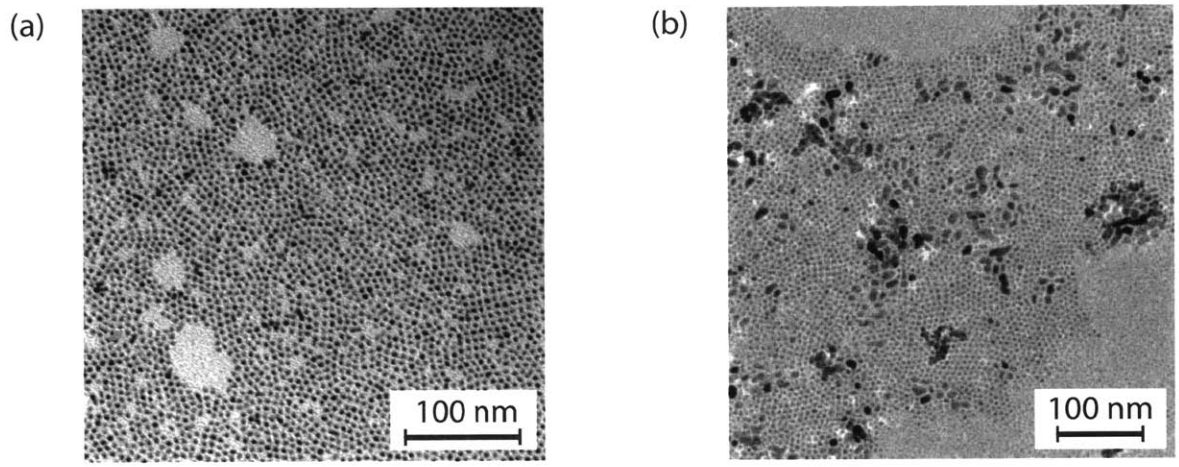

Figure 2-2: Transmission electron micrographs of PbS dots. (a) Freshly prepared butylamine capped PbS dots. (b) If we expose the dots to elevated temperatures (even 5-10 degrees above room temperature) after the growth step is complete, Ostwald ripening takes place. Briefly, Ostwald ripening is when atoms from the surface of smaller dots (with high surface energy) leave to join the surface of larger (lower surface energy) dots, giving a broad distribution of dot sizes.

100°C. After the lead precursor is made, the solution is heated to 150°C under argon, to form Pb oleate. This is followed by the swift injection of the sulfur precursor, which is made with 3.15 ml of hexamethyldisilathiane (TMS2-S) and 150 ml of ODE [127].

As the sulfur solution is injected, particles nucleate and the temperature drops from 150° C to approximately 130° C. At this slightly lower temperature, the nucleated particles grow by adding atoms from the surrounding solution to the surface. The solution is cooled after approximately 5 minutes, and the resulting dots have a diameter of 4.4 ± 0.2 nm, as seen from TEM measurements. Figure 2-2(a) shows TEM images of freshly prepared butylamine capped PbS dots. If the solution is heated for a time after the growth takes place, Ostwald ripening occurs. While controlled Ostwald ripening can help the preparation of a size series of dots, uncontrolled Ostwald ripening, can cause a large amount of disorder in the system. Figure 2-2(b) shows TEM images of butylamine capped PbS dots having undergone Ostwald ripening due to heating. Ostwald ripening in this case introduces a large size disorder in the system and must be avoided.

Size selective precipitation and filtration is performed by adding a mixture of methanol and butanol to precipitate the dots. The solution is centrifuged to collect the dots and the supernatant is discarded. At this stage for measurements on oleic acid capped dots, the dots are redissolved in hexane, and the same procedure is repeated twice. For measurements with butylamine capped dots, the dots are dispersed in butylamine, and left stirring on a stir plate inside the glovebox for a period of three days. The dots are then precipitated with isopropyl alcohol. The solution is centrifuged, the supernatant is discarded, and the dots are redissolved in hexane. Before using the dots, they are passed through a 0.1 μm filter. The size selective precipitation for either ligand is thus carried out thrice, in order to minimize the size disorder in the system.

2.2 Need for nanopatterning

Colloidal dots can be made to assemble into an ordered array or close-packed film by dropcasting or spincasting on a substrate. As the solvent evaporates, the dots assemble into a three dimensional solid. The ordering length scale is then determined by the rate of solvent evaporation, the interaction between the dots, as well as the interaction with the substrate. Typically when the colloidal solution is dropcast onto a surface, the dots tend to form clusters as shown in Figure 2-3(b). Methods to improve the conductance of the dots, such as annealing, causes cracking as show in Figure 2-3(c). Besides diminishing the charge transport efficiency for device applications, the presence of cracks and clusters, makes it impossible to study the charge dynamics intrinsic to the dots, and is thus a barrier to realizing colloidal dot based designer solids. Applications of colloidal dots in nanoelectronic and nanophotonic circuits [85], LED nanodisplays [44, 4], and diffraction gratings [97] are only possible with nanoscale control over the assembly and placement of dots on a surface. Finally, eliminating structural defects in the films, such as cracks and clustering, and their effect on charge transport is an essential step toward studying nanoscale charge dynamics and realizing the predicted charge correlations in colloidal quantum dot arrays [83].

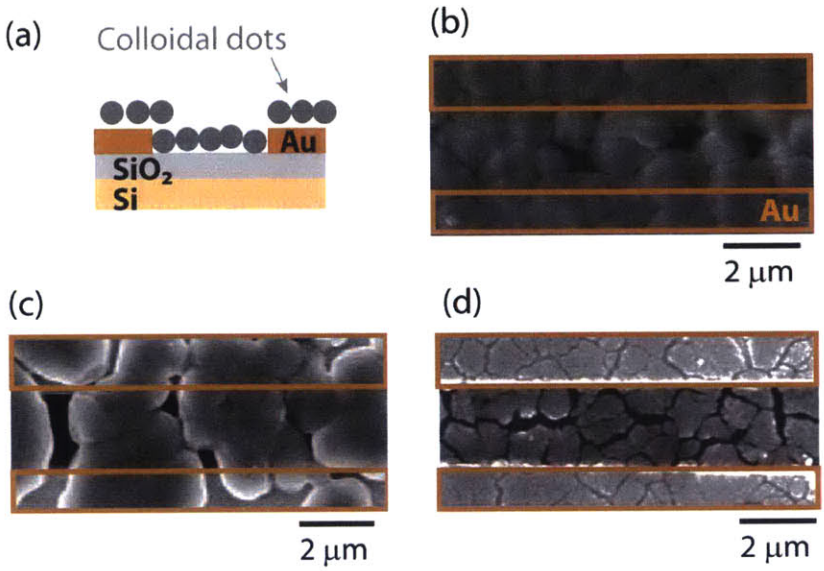

Figure 2-3: (a) Schematic of colloidal dots drop cast on an inverted FET device (side view). (b) Scanning electron micrograph of a PbSe film drop cast on an inverted FET device (top view; the gold electrodes, which are beneath the film and thus obscured from view, are outlined in orange), and (c) after annealing the film for one hour at 400 K. (d) When the thickness of the film exceeds approximately 1 μm, cracks emerge as the film dries. Image also appears in [69].

2.3 Overview of existing patterning techniques

Prior methods for assembling colloidal quantum dots into patterned structures on a substrate fall into three main categories. The first method uses a patterned template that guides the assembly of the dots (Template-Assisted Self Assembly). A second method of patterning is printing: microcontact printing [44, 30], inkjet printing [110], and nanoimprint lithography of a colloidal quantum dot-polymer composite [107]. The third entails functionalizing the dots with a ligand and forming patterns on a substrate by effectively controlling the ligand-substrate interaction.

Template-assisted self-assembly [95] is a process in which strong interactions between a template and nanoparticles lead to the arrangement of nanoparticles in structures that are predefined by the shape of the template. The templates may be hard, such as lithographically patterned photoresist, or anisotropically etched trenches in Silicon, or soft like DNA molecules [3]. At the current stage of development, it is not clear whether this assembly process can be eventually extended to nanoscale particles

($\approx 100nm$) [124]. A newer approach [78], is to use the interface between two phases, such as liquid-liquid or air-liquid, as the template. The Langmuir-Blodgett technique has been used to form monolayers at the waterair interface and to transfer them onto a solid substrate [109]. While the floating sheets are stabilized with long range order, nanoscale device integration of these sheets seems non-trivial.

Microcontact printing is a form of soft lithography that uses patterns on a master stamp to form patterns of ink on the surface of a substrate through conformal contact. Polydimethylsiloxane (PDMS) is often used as the stamp, as it can be easily molded. In order to use these PDMS stamps for printing solutions of quantum dots, the mold is typically treated with an organic compound, such as Parylene-C, to make the surface compatible with the dots. The coated stamp is then inked with quantum dots, and the dots are transferred to a substrate by contact printing. Microcontact printing can achieve nanoscale patterns, but is highly sensitive to the chemical compatibility of the dot solution, the stamp, and the substrate. The dots must preferentially adhere to the substrate over the polymer stamp, which puts a serious constraint on compatible substrates [44, 30].

Another approach has been to functionalize the ligand in the quantum dots. Park *et al.* [87] functionalized CdSe quantum dots with a photosensitive monolayer. Upon exposure to ultraviolet (UV) radiation , films composed of this material were found to polymerize, forming interconnected arrays of dots, rendering them photopatternable. Jun *et al.* [40] found that exposing lead chalcogenide films with their native oleate ligands to strong UV light, allowed the native ligands to form an insoluble cross-linked network, while the unexposed areas were still soluble to toluene solvent. By UV light exposure through a shadow mask followed by solvent rinsing, they have been able to produce a feature size on the order of 2 μm.

While the techniques reviewed here are able to attain control over the shape and placement of the dots on a specialized surface, the challenge still remains to form nanoscale arrays of colloidal quantum dots that can be integrated into a device structure with nanoscale precision.

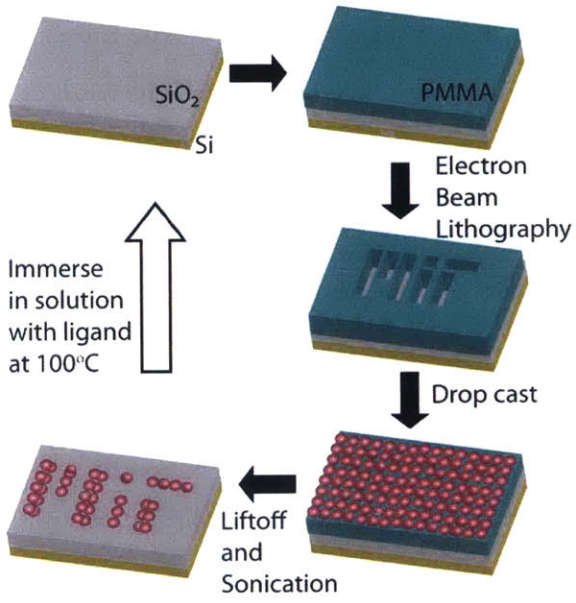

Figure 2-4: An overview of the process for patterning nanoscale films of colloidal dots.

2.4 Nanopatterning colloidal quantum dots

We use a combination of electron beam lithography followed by a lift off process to form crack-free films of nanoscale dimensions. Our technique uniquely combines the following characteristics:

- Colloidal quantum dot films with features as small as 30 nm
- Controlled placement of quantum dot films onto a surface or into a device structure with nanoscale precision (30 nm), and
- Flexibility in choice of core material and ligand

We start with a Silicon wafer with 100-300 nm of high quality thermally grown SiO_2. The wafers are cleaned with organic solvents (acetone, methanol and isopropyl alcohol), and then baked on a hotplate set at 180° C, to drive off moisture from the surface. The wafers were then coated with PMMA (polymethyl methaacrylate), which is an electron beam resist. Depending on the size of the features needed, the thickness of the PMMA stack can be adjusted. Smaller feature sizes work best with thin layers of resist. We then create the desired pattern in the form of trenches in the resist, using an electron beam. A drop of the colloidal solution is put on the

substrate using a 10 μL syringe, and allowed to spread over the entire surface. The concentration of the solution used for dropcasting, as well as the solvent, controls the thickness and packing of the resulting film. The solvent used for the work in this thesis is 9:1 Hexane:Octane, as it has been shown to give uniform films over large length scales. As a rule of thumb, for a lift off processes, say with a metal, the thickness of the resist must be atleast three times the desired thickness of the metal. Since we are dealing with a colloidal solution, instead of a metal, the thickness can be controlled only somewhat by adjusting the solution concentration.

Once the film has been allowed to dry, the substrate is immersed in acetone. The amount of time for the film to dry is determined by the concentration of the starting solution, with more concentrated solutions requiring longer wait times. During lift-off an ultrasonic bath, may or may not be needed depending on the feature size required. Sonication during lift-off ensures that the films tear cleanly at the edges of the patterns. However, sonication must be avoided if smaller feature size ($\leq$ 100 nm) is desired, as even minimal sonication can tear the patterned film. Squirting the film with acetone is a gentler alternative to sonication. For multiple large features in close proximity to each other, such as in a grating, sonication is required to remove the dots from the areas between the lines. Sometimes, we observe a residue on the surface after lift off. This may be just the residue from acetone, or the dots themselves. The substrate can be soaked in a vial of isopropanol to clean off the residue and then left to dry in the nitrogen environment of the glovebox. Allowing the isopropanol to evaporate while the substrate sits flat on a surface can also leave a residue. Instead, we hold the substrate with tweezers so that the isopropanol runs to the edge of the substrate before evaporating. A kimwipe can be used to wick the solvent from the edge of the substrate. We have found that the problem of surface residue is more severe, when the resist thickness is less than 50 nm. This is probably due to van der Waal's forces between the dots and the substrate. In this case, squirting the substrate with acetone and isopropanol after lift-off and blowing the surface dry with nitrogen can eliminate the residue. Once again, for sub 100 nm patterns, we avoid using a nitrogen gun as the force may tear the edges of the patterns.

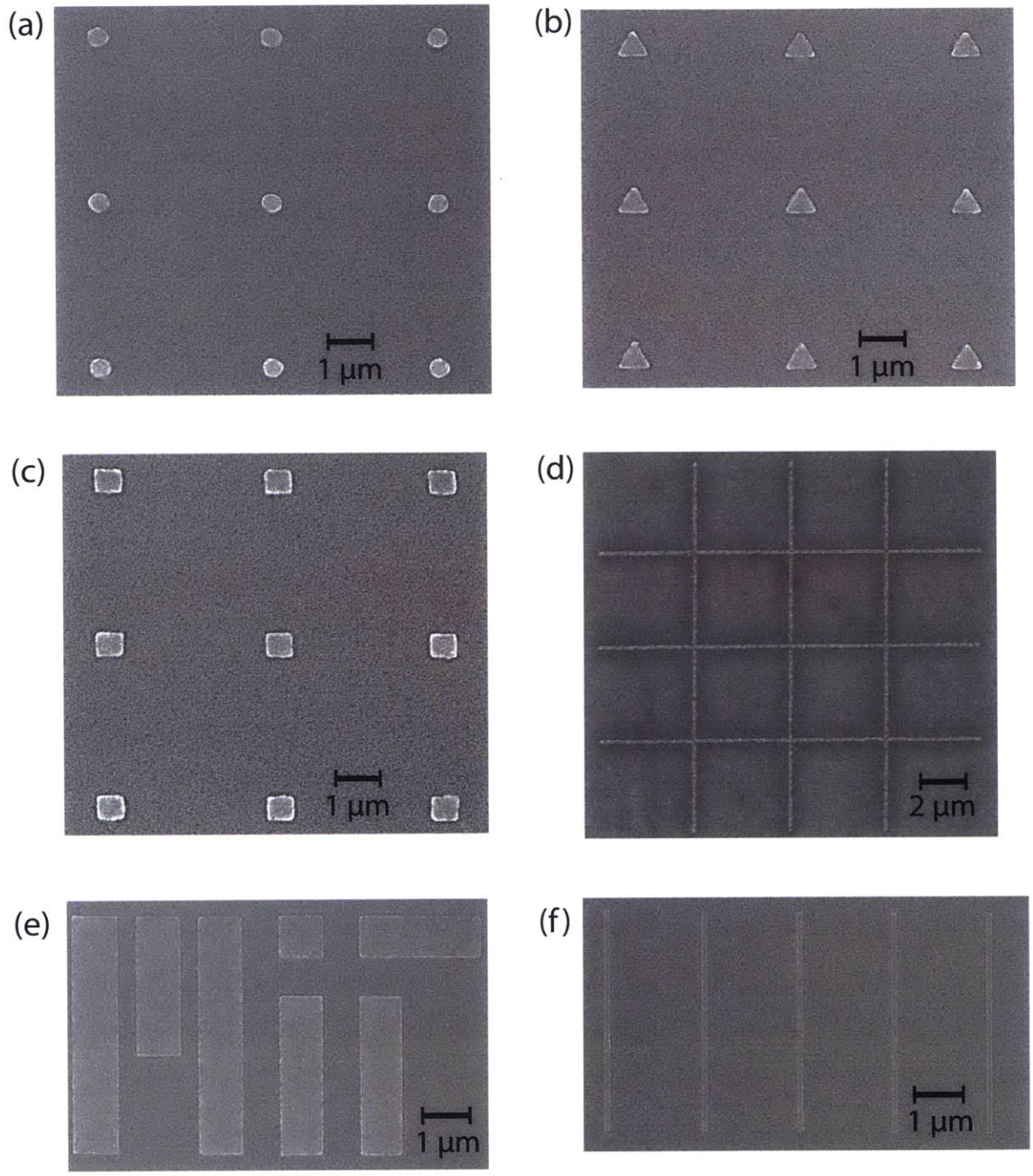

Figure 2-5: Scanning electron micrographs (a)-(f) of nanopatterned films of oleic acid capped PbS quantum dots.

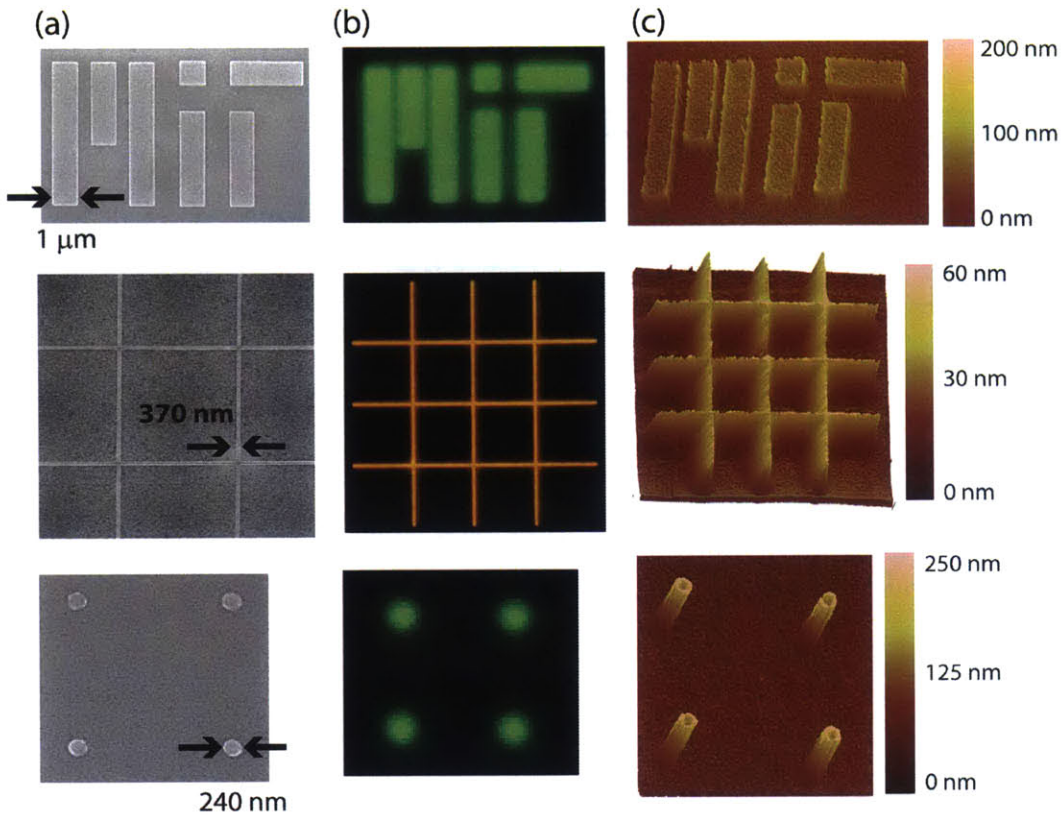

Figure 2-6: Nanopatterned films of CdSe quantum dots (first and third rows) and $Zn_{0.5}Cd_{0.5}SeZn_{0.5}Cd_{0.5}S$ coreshell dots (second row). (a) Scanning electron micrograph, (b) fluorescence (actual color), and (c) AFM images. Image also appears in [69].

In Figures 2-5(a)-(f) and 2-6, we demonstrate the flexibility in choice of dots by patterning films with PbS, CdSe and $Zn_{0.5}Cd_{0.5}SeZn_{0.5}Cd_{0.5}S$ coreshell dots. CdSe dots show fluorescence in the visible part of the spectrum that can be easily measured with a confocal optical microscope. As the patterned films fluoresce (as shown in Figure 2-6(b)), we can conclude that the dots remain unharmed in the patterning process. In Figure 2-7(a) we show 30 nm small patterns of $Zn_{0.5}Cd_{0.5}SeZn_{0.5}Cd_{0.5}S$ coreshell dots with a phosphonic acid ligand. In Figure 2-7(b), the nanoscale pattern of dots is placed with nanoscale precision relative to a nearby transistor gate. The alignment for this placement is done on the Raith 150, and the details are discussed in Appendix B.

Our nanopatterns are robust and remain bound to the surface even when immersed in non-polar solvents like hexane or octane, in which the dots are normally soluble.

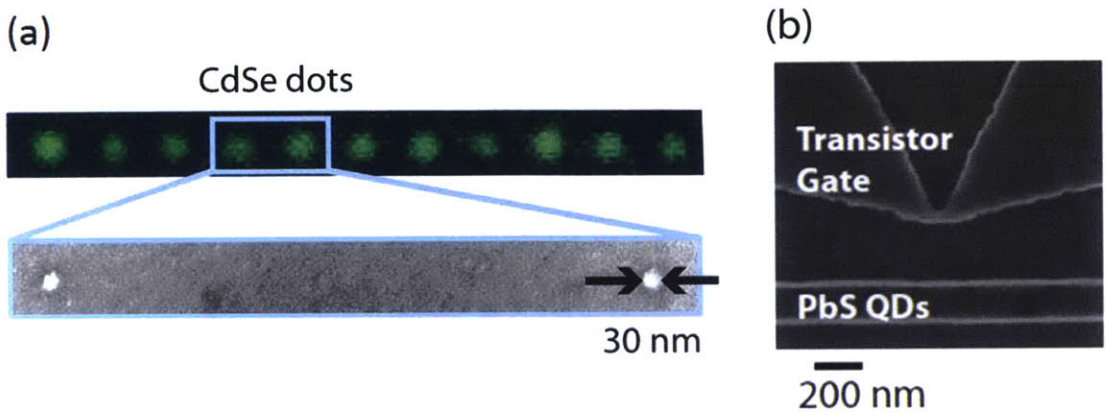

Figure 2-7: (a) Fluorescence and Scanning electron microscope (SEM) image of 30 nm small patterns of $Zn_{0.5}Cd_{0.5}SeZn_{0.5}Cd_{0.5}S$ coreshell dots with a phosphonic acid ligand (b) 200 nm wide pattern of PbS dots with butylamine ligand, placed 200 nm away from a transistor gate.

We hypothesize that during the lift-off process, acetone removes the ligands from the surface of the dots on the outermost layer of the film rendering the film insoluble. We speculate that the ligand is being removed from only the top layer because the nanopatterned films fluoresce, which would not be the case if the ligands were absent.

It is also possible to remove the patterned films from the substrate and recycle the substrate, if necessary. As the patterning process is expected to remove the ligand from the top layer of dots, the first step is to drive the ligand back on to the surface of the dots. The dots should then be soluble in hexane or octane. Because the dots are bound to the surface, additional thermal energy must be provided to overcome the attractive forces. The use of octane as a solvent is preferred because its boiling point (125 °C) is higher than that of other commonly used solvents like hexane (68 °C), and the solution does not evaporate when we raise the temperature for a prolonged period. Octane and Hexane are extremely volatile solvents, and care must be taken while heating them. We successfully removed butylamine capped PbS dots from an oxide substrate, by submerging the substrate with the pattern in a solution of 19:1 octane/n-butylamine and heating it to 100 °C overnight.

2.5 Ligand exchange

While ligands play an important role in the synthesis of colloidal dots, they also play a pivotal role in the passivation of surface electronic states, and the assembly of dots into an array. Changes in the inter-dot separation, induced by changing the ligands, can significantly influence the ordering, and thereby the electrical properties of the quantum dot arrays. Highly insulating superlattices with long range order are formed with long ligands that provide a large tunnel barrier between dots. Shorter ligands, and subsequently smaller tunnel barriers, lead to more conducting arrays. However the packing of dots in arrays stabilized with short ligands, tends to be glassy and chaotic, because of strong interparticle interactions. The importance of surface ligands can hardly be overemphasized.

As mentioned briefly in section 1.1, ligand exchange can be performed while the dots are in solution (solution exchange), or after deposition of the quantum dot film (solid state exchange). Our patterning technique can be easily extended to a solution ligand exchange, by simply adjusting the concentration of the solution for dropcasting. However, we recommend special precautions when working with dots that have undergone a solution ligand exchange. Shorter ligands tend to be less stable in solution, and there is a high probability that they fall off the dots causing them to agglomerate. While agglomerated dots are undesirable for any transport study or device application, they can cause the patterning process to fail. When dropcasting agglomerated dots, either clumps appear in the in the resulting film or the patterns wash off entirely from the substrate during the lift-off process. In PbS dots, the native oleic acid ligand, can be replaced with n-butylamine in solution. If the n-butylamine-capped dots are stored in solution for an extended period, the ligand will fall off from the dots causing them to agglomerate. The solution exchanged dots, must therefore be used as soon as possible after the final precipitation step is completed. On the other hand, more flexibility with timing exists in the step prior to the final precipitation, and the dots can be left stirring in n-butylamine in a glovebox environment for as long as needed. We recommend suspending the dot solution above the stir plate,

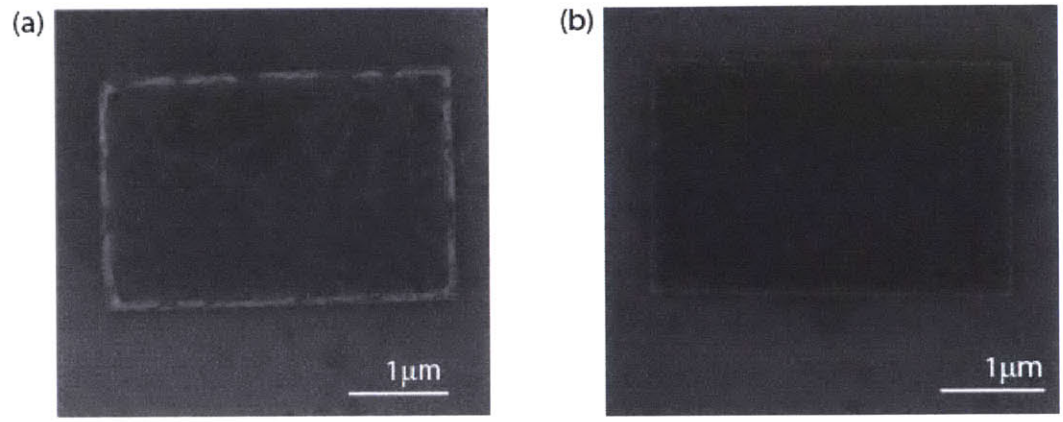

Figure 2-8: Scanning electron microscope (SEM) images of PbS films with post deposition ligand exchange from butylamine (BA) to the shorter ethanedithiol (EDT) ligand. (a) Ligand exchange performed before lift off, and (b) ligand exchange performed after lift-off.

rather than have it be in direct contact, in order to avoid Ostwald ripening of the dots due to heating. Figure 2-7(b) shows a 250 nm wide and 600 nm long nanopattern made from butylamine capped PbS dots.

Shorter ligands, such as thiols (-SH) and halides(-Cl,-Br), cannot easily be stabilized in solution, and the exchange needs to be performed after the deposition of the film. In order to the carry out a post deposition ligand exchange, the array after deposition, is chemically treated with a solution containing the new ligand. This process naturally strains the already deposited film, leading to the formation of cracks. For unpatterned films, these cracks are filled by dropcasting another layer of dots, followed by a ligand exchange for this layer, and the process is repeated till all the cracks are filled. Our patterning technique can be extended to a solid state ligand exchange only in a limited capacity. As the native ligand is fairly long, we first perform a solution ligand exchange to a shorter ligand in order to reduce subsequent shock to the film. We dropcast the solution exchanged dots onto the lithographic pattern, and then proceed to a post deposition ligand exchange. Although not mandatory, a surface treatment is sometimes performed before dropcasting to improve adhesion of the dots to the surface. The details of the treatment, and the constraints this treatment may impose on the patterning process are discussed in the next section. The chemical treatment for ligand exchange may be performed either before or after

lift off of the patterns is complete.

For PbS dots, we exchange the native ligand to butylamine in solution. We create 3 μm $\times$ 3μm wide trenches in 200 nm of PMMA and then dropcast with the butylamine dots. In order to exchange the butylamine ligand to EDT, we chemically treat the film by dipping the substrate in 0.05M EDT solution in acetonitrile for 3 seconds. Figure 2-8(a) and (b) show scanning electron microscope (SEM) images of the patterns formed when the ligand exchange is performed before and after lift-off. As seen from the images, a ligand exchange performed after lift-off gives more uniform films. However, minor cracks develop along the edges of the pattern irrespective of which way the exchange is carried out. This makes it very difficult to make patterns smaller than $\approx 1\mu m$ with a post deposition exchange, as they will be completely obscured with cracks. Given the need for a fixed film to resist thickness ratio for a successful lift-off process, it seems unlikely that nanoscale patterns can be obtained with shorter ligands with our technique. One could imagine working with very thick resists, and extremely dilute dot solutions. Then, by performing a ligand exchange before lift-off, one could in principle fill the cracks in the film. However, it is very difficult to pattern small features with thick resists, and also it is very difficult to estimate before hand how many layers of dots would be needed to completely fill all the cracks present in the film.

For the work presented in this thesis, we work with the native ligand (oleic acid), and butylamine which is compatible with a solution ligand exchange. Although longer ligands give more resistive films, they help stabilize long range order and the ease in nanopatterning dots with these ligands enables us to investigate transport in nanoscopic patterns.

2.6 Film morphology and characterization

We use a combination of atomic force microscopy (AFM), Transmission electron microscopy (TEM), and Helium ion microscope imaging to study the surface profile and packing of dots in the nanopatterned films. As seen in Figure 2-6 and Figure 2-9,

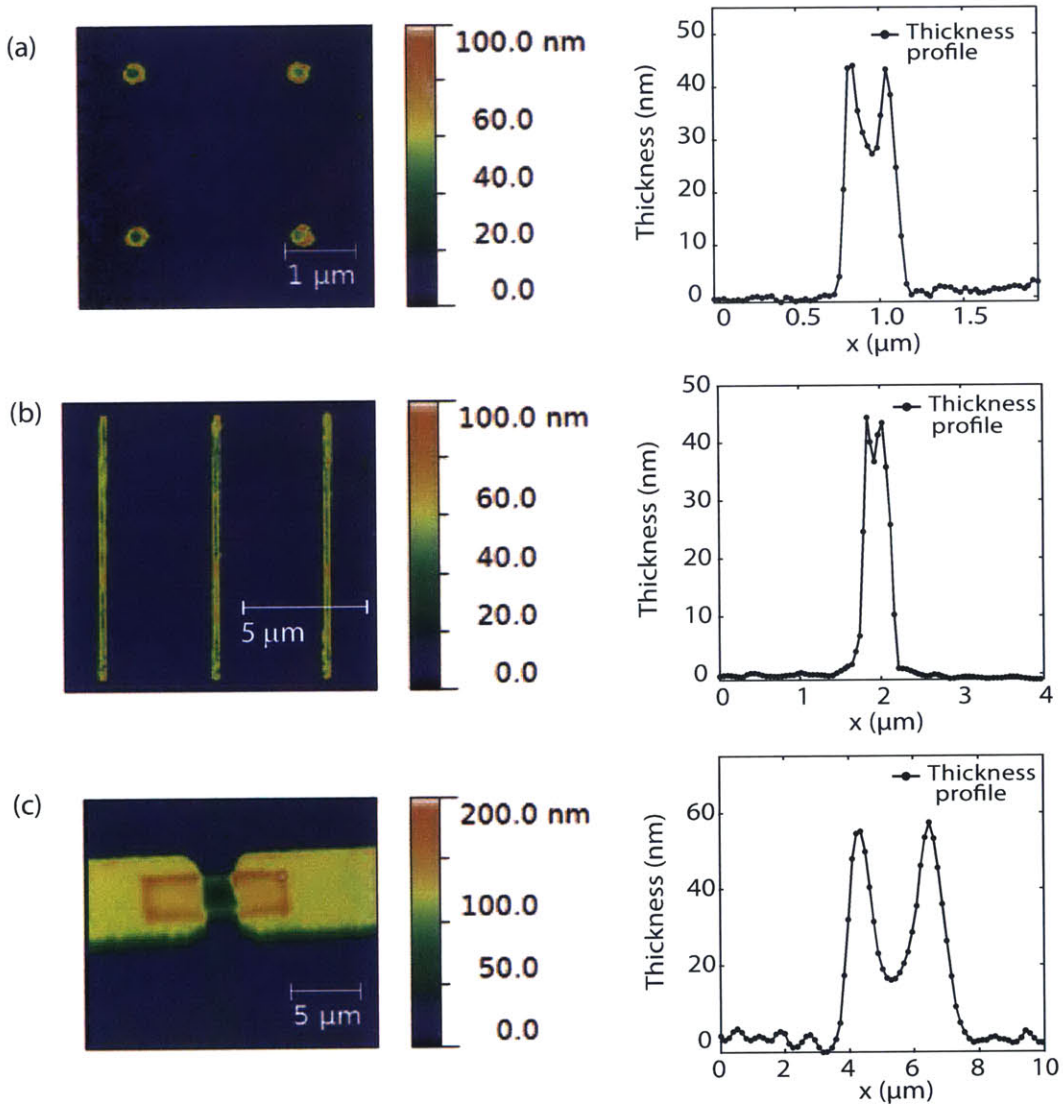

Figure 2-9: Atomic Force Microscope (AFM) images and line scans of patterns with butylamine capped PbS dots. (a) 400 nm wide circles created with 200 nm resist, (b) 200 nm wide lines created in 200 nm resist, and (c) 600 nm wide rectangular pattern on 60 nm thick Ti/Au electrodes created on 200 nm thick resist.

the patterns do not show any macroscopic cracks or clusters. Line scans across the patterns, however, show that the edges of the pattern are higher than the center. It has been suggested [76] that the solvent used for dropcasting can influence the surface profile, and using hexane and octane as solvents can lead to a concave film surface. We tried a variety of different solvents including pentane, Tetrachloroethylene (TCE), and 9:1 Octane:Octanol, but the surface profile did not change. We find that a square cross-section of the trench helps reduce the height difference between the center and the edges. An example of a square cross-section is to pattern a x nm wide trench in x nm thick resist. Figure 2-9(a) and (b) show the AFM images and corresponding line scans for circles with a 400 nm diameter and 200 nm wide lines on 200 nm thick PMMA. For similar film thickness, the height variations are more severe in the 400 nm circles. We make a pattern on gold electrodes, as shown in Figure 2-9(c), and see that the film is continuous over the gold electrodes. With the same resist thickness we see that the height difference is more severe for the wider pattern. We also find that using dilute solutions for dropcasting, in order to obtain thinner films, makes the problem worse. This means that to some extent, the thickness of the film, and hence the concentration of the solution used for dropcasting, needs to be adjusted according to the desired width and length of the pattern.

We use Transmission electron microscopy (TEM) primarily to study the packing of individual dots in the film. Since dilute solutions are used for dropcasting on TEM grids, this also gives us some insight into the formation of the pattern itself. We use 40nm PELCO silicon dioxide support films for TEM with 24 50 $\times$ 50 μm apertures. We stick the grid onto an empty silicon chip using PMMA as glue. After the PMMA dries, we then spin on PMMA on the TEM grid for electron beam lithography. The patterns can now easily be created on these TEM grids. This procedure works just as easily for regular carbon TEM grids but we use the $Si0_2$ grids to keep the substrate for patterning the same. Figure 2-10 shows the TEM images of the patterns formed. For wide patterns, and dilute concentrations, we find that film formation begins at the edges of the resist, and then moves inwards. As we move from a dilute (Figure 2-10(a)) to a more concentrated solution (Figure 2-10(b)), we observe complete coverage of the

pattern. As we zoom in to study the center of the film, for patterns with complete coverage, we find that while butylamine capped dots give close packed films, films with oleic acid capped dots tend to be polycrystalline. Given the hydrophobic nature of the ligands, it is natural to expect them to preferentially stick to PMMA, which is also hydrophobic, rather than the hydrophilic oxide. This explains the surface profile observed for all of the patterns but also highlights a constraint on the final thickness of the film especially for wider patterns, making it seemingly impossible to obtain thin films($\leq$ 50 nm) over large ($\geq$ 400 nm) length scales. Surface treatments, discussed below, can make the dots like the oxide just as much as PMMA, however we were unable to find a treatment which made the dots like the oxide and dislike the resist.

Surface treatment

Surface treatments for the substrate are designed to improve adhesion of dots to the substrate and typically involve growing a self-assembled monolayer on the substrate. When performed on oxide substrates, these treatments can also help passivate surface traps. The most commonly used surface treatment involves a coating of MPTMS (3-mercaptopropyl-trimethoxysilane). Our patterning process is compatible with a surface treatment, when the treatment is performed after the lithography step. Pre-treating the substrate, and then spinning on the resist, makes the resist adhere better to the substrate, and can make lift-off difficult. In order to form patterns with a surface treatment, the substrate is first cleaned for 5 minutes in oxygen plasma. We then carry out the electron beam lithography. The patterns are developed, creating trenches in the resist. The substrate is then immersed in 0.2 M (3-mercaptopropyl)trimethoxysilane (MPTMS, in toluene) solution for 12 hours to grow a self-assembled monolayer of MPTMS. We then dropcast on the substrate, followed by a lift-off process. Because of the strong adhesion of the dots to the surface, a sonication step is essential to getting the patterns to work. However, this makes it impossible to form very small patterns with a surface treatment, as they are unable to withstand sonication. As shown in Figure 2-11, surface treatment gives a better surface morphology, but the edges are still taller than the bulk of the film.

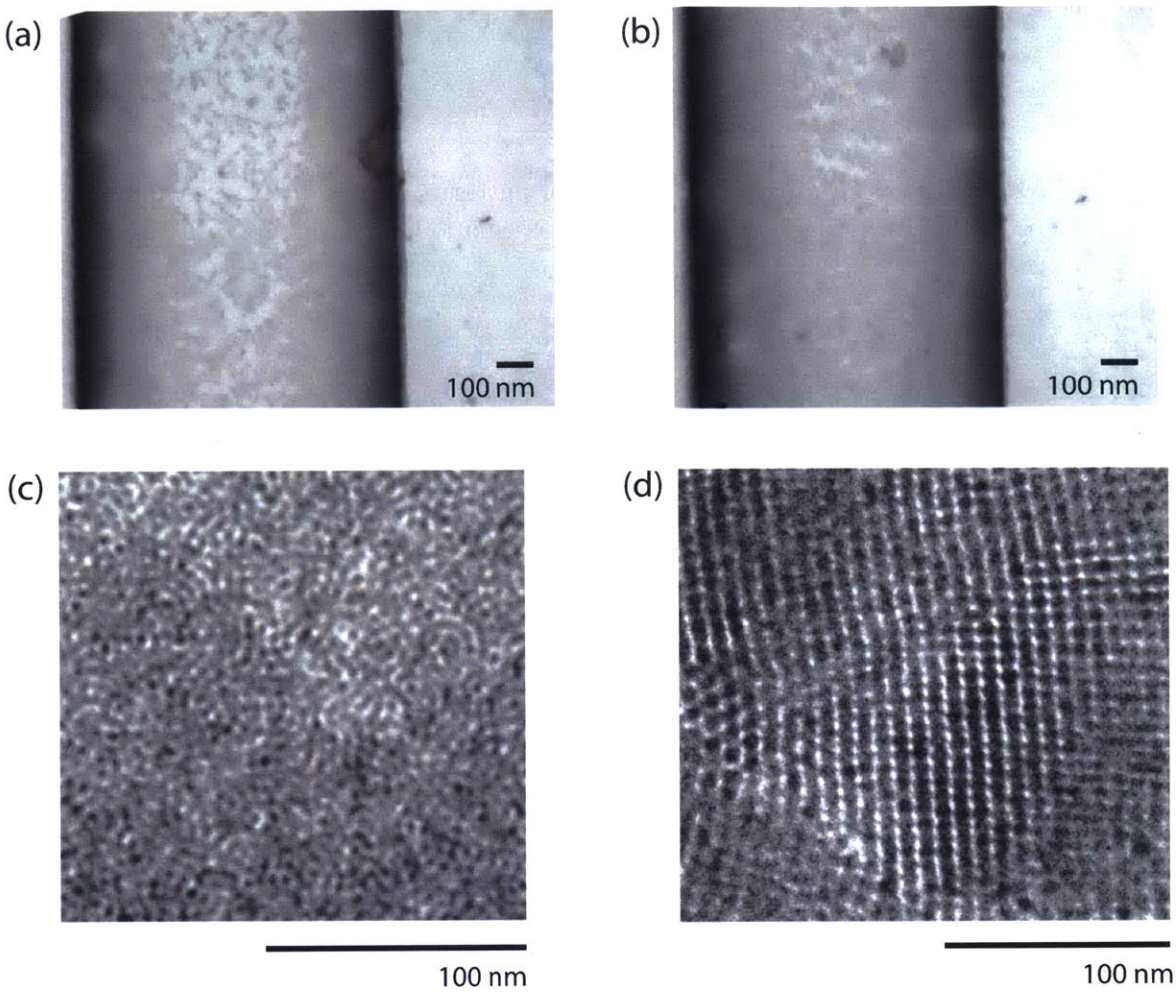

Figure 2-10: Transmission electron micrographs showing the formation of patterned films. (a) Patterns made on SiO_2 TEM grids showing formation of film starting at the edge of the resist. (b) As the dropcasting solution is made more concentrated, complete coverage of the pattern is achieved. (c) Packing of butylamine capped PbS dots in the middle of the pattern showing a close packed film. (d) Packing of oleic acid capped PbS dots from the middle of the pattern showing polycrystalline structure.

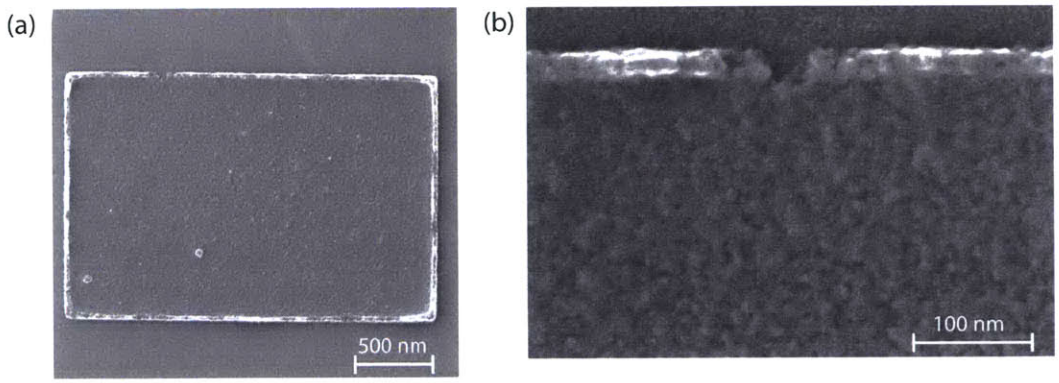

Figure 2-11: Helium ion microscope images of patterns formed after treatment of the oxide with 0.2 M (3-mercaptopropyl)trimethoxysilane (MPTMS, in toluene).

2.7 Electrical properties

The electrical current in dropcast quantum dot films is typically small because the electronic coupling between dots, as determined by the size of the native capping ligand, is weak [89, 34]. To increase electrical current, either the film is annealed [125, 21, 67] or the native capping ligand on the dot is exchanged for a smaller molecule by immersing the film in a solution containing the smaller molecule [105]. In both of these approaches, there is a strong driving force that creates cracks in the film, adding to the structural defects, as seen in Figure 2-3. Despite the clusters and cracks, it has been possible to study charge-transport in these films because current may flow through a continuous pathway that connects the clusters, or, a second layer of dots can be deposited to fill in the voids between clusters [105]. However, it is likely that structural defects influence the transport properties in the film.

We begin with microscopic unpatterned films, and dropcast on 2 μm or 5 μm long electrodes which are 800 μm wide. The film thickness is measured by scratching the patterns and measuring with a profilometer. The thickness for the films is observed to be 300 nm and 40 nm, from two sets of devices. We then immerse the substrates in acetone in order to compare them with the patterned films as the lift-off process is done in acetone. There have also been reports of increased conductance due to necking of the dots from methanol exposure [49], and acetone is expected to have a similar effect. The current is immeasurably small for oleic acid capped dots. For butylamine

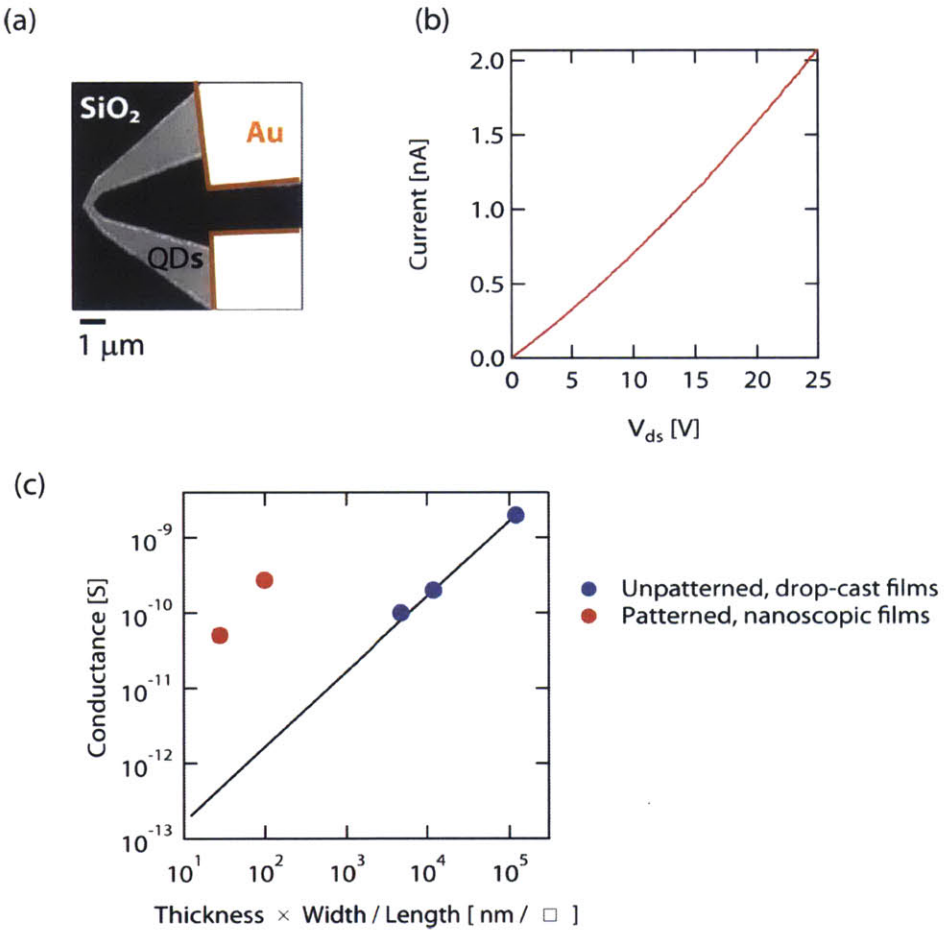

Figure 2-12: (a) An AFM image of a film of butylamine capped PbS dots, which is 350 nm wide at its narrowest point. The film is continuous, in contrast to those shown in Figure 2-3 (b)-(d). (b) Current-voltage characteristic of the nanopatterned film shown in (a). (c) Conductance of butylamine capped PbS dots versus the dimensions of the film with $V_{ds} = 0.1$ V. The red circles represent the conductance of the nanopatterned film shown in (a) and a comparable rectangular film with nanometer dimensions. The blue circles represent the conductance of unpatterned films in a device structure shown in Figure 2-3. The conductivity of the nanoscopic films is 180 times higher than what is found in the microscopic films. Image also appears in [69].

capped dots, the current-voltage characteristics are ohmic at low voltages, and the zero bias conductance is extracted from these measurements. The conductivity σ is calculated from the relationship G = $\sigma(wt/l)$ where G is the conductance, l is the length, t is the thickness, and w is the width of the film. The conductivity of the unpatterned, microscopic films is approximately 0.09 μS/cm.

We measure the current-voltage characteristics of two nanopatterns. The first pattern is rectangular with dimensions 50 nm thick, 2 μm wide and 1 μm long. The second pattern, shown in Figure 2-12(a) is 130nm thick between two gold electrodes, and tapers down to a width of 350 nm at its narrowest point. From the current-voltage characteristics, which is ohmic at low voltages 2-12(b), we find the zero-bias conductivity to be 17 μS/cm. We plot the conductance versus the dimensions of the films in Figure 2-12(c). The plot illustrates that the conductivity of the crack-free, nanopatterned films is 180 times higher than the conductivity of the unpatterned, dropcast films, which exhibit structural disorder.

To conclude, we have demonstrated the ability to form nanoscale patterns of colloidal quantum dot arrays that are structurally continuous. Our patterning technique, based on a simple lift-off process, allows for flexibility in the choice of dot material, ligand, and solvent. Electrical measurements on nanopatterned arrays reveals electrical conductivity two orders of magnitude higher than in macroscopic or unpatterned arrays, in which the dots form clumps and clusters. We speculate that the increased conductivity stems from the elimination of defects in the array. This technique for pattering quantum dot arrays, opens the possibility of studying the nanoscopic charge dynamics in the localized states of the dots, and we explore this aspect in the remainder of this thesis. Eliminating structural defects is also an essential step toward realizing the charge correlations predicted in ordered quantum dot arrays, and the use of colloidal dots in nanoelectronics, nanophotonics, LED nanodisplays, and nanoscale detection of biomolecules.

Chapter 3

Noise in nanopatterned colloidal quantum dot arrays

In this chapter, we discuss the noise characteristics of PbS quantum dot arrays. In Section 3.1, we give an introduction to the common sources of noise in solid state systems. In section 3.2, we focus on noise in disordered and inhomogeneous materials, and present a literature survey of noise studies in colloidal quantum dot systems. In sections 3.3 and 3.4, we describe our device structure and the experimental set up for noise measurements. Finally, in sections 3.5 and 3.6, we present our results and discuss a model based on Levy statistics to explain our observations.

3.1 Noise and fluctuations in solids

We can think about noise as a spontaneous random variation of a physical quantity as a function of time, or a random deviation of the physical quantity from some mean value. Noise is typically a manifestation of thermal motion of matter, and the discreteness of its structure. The ultimate accuracy of measurement of any physical quantity is noise limited, and so noise is usually viewed as the bane of measurements. However, a careful study of noise in a material can provide additional insights into the properties of the system, and can even be used to characterize exotic states in materials such as charge density waves and quasi-particles in a fractional quantum hall

state [8]. During the past decade new phenomena and new features of old phenomena have been studied such as noise in ballistic conductors, noise in strongly disordered conductors, noise in high-T_c superconductors and, magnetic 1/f noise in spin glasses and so on. In this section, we discuss the underlying physics of some of the common sources of noise in solids [46].

When we measure a signal as a function of time, *x(t)*, the noise in the signal is best characterized by the spectral density. The power spectral density of a signal tells us which frequencies carry the signal's power. Roughly, we can estimate the spectral density from the magnitude squared of the Fourier Transform (FT) of a finite stretch of the signal. However, the FT computation assumes that the finite signal repeats over and over. If the initial and final value of the finite signal are not the same, this can lead to aberrations in the FT because of the abrupt changes at the start and end of the signal. For a better estimation of the spectral density, 'windowing' is used where the finite signal is premultiplied with a value that smoothly decreases to zero at each end. This helps to more accurately assign power to the frequencies and reduces aberrations from the finite size of the signal.

Johnson noise

Johnson noise in conductors arises from the thermal fluctuations of the electron density within them. In a letter to Nature in 1927, J. B. Johnson wrote about voltage fluctuations that appear *to be the result of thermal agitation of the electric charges in the material of the conductor* [38], and Harry Nyquist provided a theoretical explanation [84]. Johnson's name became associated with this noise, after he experimentally verified the dependence of the noise voltage on the resistance [39]. According to Nyquist, an idealized resistor is assumed to contain a voltage generator causing a fluctuating emf at the terminals. The mean squared voltage, V^2_{rms}, and the associated spectral density, S_v, (proportional to the FT of the signal) are given by:

$$\left\langle V^2_{rms} \right\rangle = 4Rk_BT\Delta f \tag{3.1a}$$

$$S_v = 4Rk_BT \tag{3.1b}$$

where, R is the resistance of the conductor, k_B is the Boltzmann's constant, T is the absolute temperature, and Δf is the bandwidth of the measuring instrument. The noise spectral density for Johnson noise is independent of frequency, and for this reason Johnson noise is said to be white. As the magnitude of the noise only depends on the resistance and the temperature, this has attracted interest for using thermal noise as a means of measuring temperature [122]. For Johnson noise thermometry (JNT), the theory is exact unlike usual thermodynamic methods, which are imperfect because there is no such thing as an ideal gas or an ideal blackbody.

Shot noise

Walter Schottky discovered shot noise in 1918, while studying vacuum tubes[96]. Shot noise in an electrical conductor is a consequence of the quantization of the charge. Shot noise only occurs when there is a current flow. Schottky assumed the uncorrelated arrival of particles with a poissonian distribution of arrival times, and arrived at an expression for rms fluctuations, I^2_{rms}, and spectral density, S_I, of shot noise:

$$I^2_{rms} = 2q\overline{I}\Delta f \tag{3.2a}$$

$$S_I = 2q\left\langle \overline{I} \right\rangle \tag{3.2b}$$

where, q, is the charge of the particle, and $\overline{I}$ is the average current flowing through the conductor. Like Johnson noise, the spectral density of shot noise is also white.

In contrast to conductance measurements, which measure an averaged charge over time, shot noise measurement are sensitive to the magnitude of the charge itself. An understanding of the shot noise in a system can then be used to determine the charge and statistics of the particles relevant for transport. Theoretical investigations [41] into the quantum corrections for shot noise due to quasi-particles, have found that the classical expression for shot noise is still valid if the charge, q, is replaced by the quasi-particle charge. After the observation of fractional quantum hall effect (FQH) in systems, Laughlin [54] argued that the conduction properties could be explained

in terms of quasi-particles with a fractional charge. R. de-Picciotto *et al.* utilized quantum shot noise measurements to unambiguously show that the current in the FQH regime, at filling factor 1/3, was carried by quasi-particles with charge e/3 [19]. For a complete overview of shot noise in mesoscopic systems, we refer the reader to a review article by Blanter and Büttiker [10].

1/f noise

Low-frequency noise with the spectral density, S(f), proportional to $1/f^{\gamma}$ (where f is the frequency and $\gamma \sim$ 1-2) was initially discovered in vacuum tubes [37]. It has since been observed in a wide variety of systems including current fluctuations in resistors, intensity fluctuations in music and even signals in human cognition. Despite almost a century of research, 1/f noise remains a controversial phenomenon and numerous debates continue about its origin and mechanisms. The common name for this noise does not imply the existence of a single physical mechanism that gives rise to all of its manifestations. In fact, it is now accepted that different fluctuation processes can be responsible for the 1/f noise in different materials and devices. In a review article on low frequency fluctuations, Dutta and Horn review the sources of 1/f noise in materials [22].

The rms current, I_{rms}, and the spectral density, $S_V(f)$ of 1/f noise can be illustrated with the phenomenological equations by Hooge [33]:

$$I_{rms}^2 = \alpha_H \frac{i_{1/f}^{2+\beta}}{N_c f^{\gamma}} \tag{3.3a}$$

$$S_V(f) = \alpha_H \frac{V_{DC}^{2+\beta}}{N_c f^{\gamma}} \tag{3.3b}$$

where, $i_{1/f} = I(t) - \overline{I}$, N_c is the number of carriers in the system, and f is the frequency. α_H, β and γ are constants. α_H is also known as Hooge's constant, and is dimensionless if $\gamma = 1$ and $\beta = 0$. It is important to note here that these equations are empirical and no theoretical reason exists for this dependence. Over the years a lot of data have been tabulated for metals and semiconductors showing room tem-

perature noise in approximate agreement with this equation for a universal value of $\alpha_H \sim 2\times10^{-3}$. Notable deviations from Hooge's equation have been found from noise measurements in Manganin, semi-metal Bismuth [116], and most recently graphene sheets [5]. Even simple metals such as Cu, Au and Ag show strong deviations as a function of temperature in ways that are characteristic of each metal [23]. At the same time, Hooge's relationship cannot be undervalued. It is the only relationship that allows one to estimate, however crudely, the magnitude of the spectral density of noise in uniform conductors. For strongly disordered and inhomogeneous conductors, the measured values of α_H can be many orders higher than the expected value of 2×10^{-3}.

Telegraph noise

In small electronic devices. the resistance and the electric current often switches at random between two (or several) discrete values, giving random telegraph noise (RTN). The time interval between switching events is random, but the values of the fluctuating quantity are time independent. In the early 1980's, resistive switchings were found to be caused by the switching of a single electron or single defect in nanometer-size semiconductor structures [90].

In its most elementary form, a random telegraph signal consists of the current through a device switching between an on and an off state. Figure 3-1(a) shows the telegraph noise seen in a narrow channel MOSFET made for the research in this thesis. The RTN is characterized by three parameters: t_{on}, t_{off} and the amplitude of the switch. While the on and off times are randomly distributed, the amplitude is usually fixed as can be directly seen from the time trace. When analyzing the RTN for a sufficiently long period of time, one can establish the probability distribution function of the switching times, which are Poisson distributed in this case (Figure 3-1(b) and (c)):

$$P(t) = \frac{1}{\tau} e^{-t/\tau} \tag{3.4}$$

The origin of telegraph noise in MOSFETs is the capture and release of single electrons

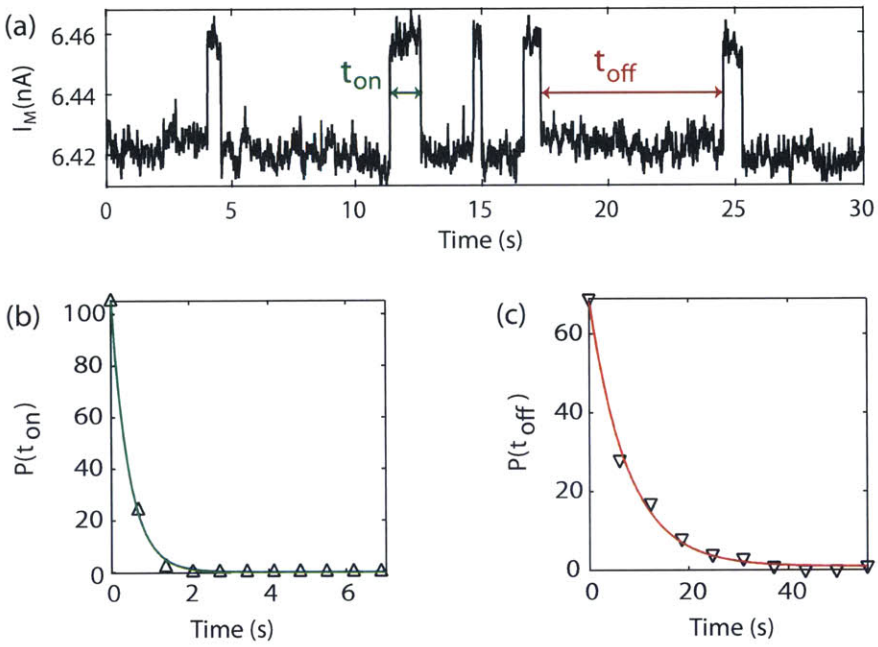

Figure 3-1: (a) Random telegraph noise (RTN) observed in a silicon MOSFET. The current from the device jumps between an on and an off state. The origin of telegraph noise in a MOSFET is the capture and release of single electrons from a trap state, probably in the oxide. (b) The probability distribution of the on time, $P(t_{on})$ and (c) off time $P(t_{off})$ obtained from telegraph noise measurements. The green and red lines are fits to the functional form given by equation 3.4.

from a trap state. By studying the evolution of the characteristic times as a function of temperature or gate voltage, one can use the noise as a tool to characterize the traps.

3.2 Noise in disordered and inhomogeneous systems

A large variety of systems can be classified as disordered or inhomogeneous. They exhibit higher noise than homogenous conductors with the same dimensions and resistance, primarily because of a non-uniform distribution of electric fields and current densities, if the current is confined to narrow paths within the material. The spectrum of resistance fluctuations in these systems is usually 1/f. A strong motivation for noise studies in these materials has been the possibility of using noise measurements as a

probe for further understanding of the underlying complex conduction mechanism. Examples of 1/f noise studies in disordered or inhomogeneous systems found in the literature include but are not limited to: metal insulator mixtures [111], conducting polymers [12], doped semiconductors [102] and sliding charge density wave systems [7, 17].

The physics of fluctuations in disordered materials, is in general very complicated and material specific. However, there are some common features that can be understood by a bond percolation model or a random resistor network. The simplest model for a strongly disordered material is a two dimensional square lattice of sites connected with bonds, as shown in Figure 3-2(a). Each bond connecting adjacent sites i and j has a fluctuating resistance r_{ij}, which in the simplest case may be either 0 or 1, corresponding to a broken and an unbroken bond respectively. For a more realistic picture of disorder, one may assume a Gaussian, exponential or even a power law distribution for the fluctuations. An unbroken bond can be considered as a channel through which current can pass. If p denotes the fraction of unbroken bonds, at some critical value p_c an infinite cluster (IC) will appear which threads the entire lattice. At $p = p_c$, current starts to flow between the electrodes, and the conductivity of the lattice is determined by the IC. Gefen *et al.* [27] introduced a non-linear random resistor network (NLRRN), where a broken bond can become conducting or unbroken if the voltage applied across it is larger than a critical voltage. For sufficiently low voltages, the current then flows only through the IC, and the conduction is linear. As the voltage bias is increased, and exceeds the threshold for some broken bonds, they become conducting leading to a non-linear macroscopic conduction. Figure 3-2(b) shows a new conduction channel opening up as a function of field in a 3×3 network.

In disordered systems within a percolation model, the correlation length or mean free path of the carriers is typically much smaller than the sample dimensions, so that the fluctuations of different bonds in the network can be assumed to be uncorrelated. For $p > p_c$, the number of current paths in the system is large, and if the resistance along different paths is uncorrelated, the contribution of fluctuations to the total resistance tend to cancel one another. As the system approaches the percolation

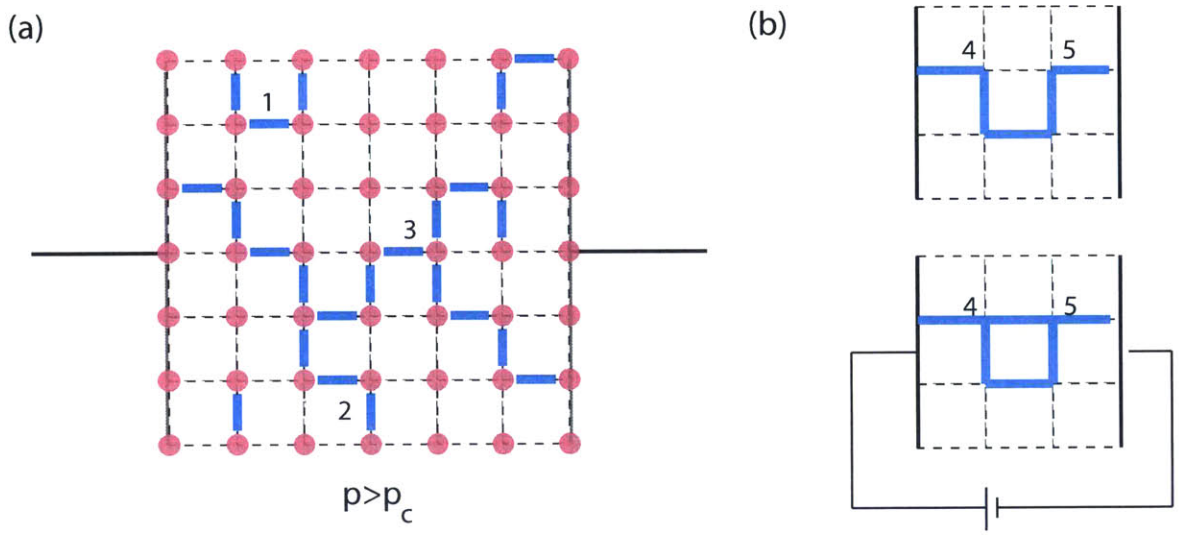

Figure 3-2: The random resistor network (bond percolation) (a) Thick blue lines and black dashed lines correspond to unbroken and broken bonds respectively. 1 shows an isolated cluster, 2 shows a dead end, and 3 shows a segment of the infinite cluster backbone. (b) A 3 × 3 network with a conducting path between the electrodes. As an external bias is applied, $V \geq V_{th}$, a new conduction channel opens up between points 4 and 5.

threshold, there are very few conduction channels, and the cancellation effect becomes smaller. In the model discussed here, only the resistance of individual bonds fluctuate, but in some systems even the fraction, p, of unbroken bonds fluctuate. Fluctuations in number of superconducting junctions in Josephson junction arrays are equivalent to fluctuating $\delta p(t)$.

A special example of transport in strongly disordered systems is hopping conduction. The hopping can be to nearest neighbors or variable range. Because the tunneling probability depends exponentially on the distance between two sites, some current paths are effectively cut because of their exponentially large resistance, just as in the disordered lattice model. The current flows mainly along paths which form a network similar to an IC in the percolation model. Now that we have developed an understanding of the sources of noise and fluctuations in homogeneous and inhomogeneous materials, we briefly overview noise studies on colloidal quantum dot systems.

3.2.1 Overview of noise in colloidal quantum dots

Noise studies in colloidal quantum dot systems have been primarily focused in two directions. As there has been much interest to integrate metallic and semiconducting dots into devices, the first direction is to understand 1/f noise in the granular materials which may impact device performance. 1/f noise has been shown to limit the sensitivity of chemoresistive sensors based on metallic dots [52] and detectivity of colloidal quantum dot infrared photodetectors [56, 43].

The second and more interesting direction is the study of fluorescence intermittency or blinking in colloidal dots. Blinking was first observed during optical microscope studies on single CdSe dots [79]. CdSe dots have a bandgap which lies in the visible part of the spectrum, and can exhibit fluorescence, with an emission wavelength that can be tuned by changing the size of the dot. Optical microscopy of single immobilized dots showed blinking behavior, where the dots alternate between on (fluorescing) and off (non-fluorescing) states. Electron jumps between discrete energy levels is expected to give emission at a frequency governed by the separation between the energy levels. However jumps where the fluorescence or emission literally stops under continuous excitation, are unexpected. The experimentally observed off-times of several seconds or minutes are also vastly longer than μs or ms timescales expected from the level separation and other quantum mechanical considerations. The on- and off- time distributions follow power law dynamics with exponential cutoffs under fairly general experimental conditions and are the most striking feature of colloidal quantum dot blinking, suggesting a universal underlying mechanism. More recently, blinking behavior was also observed from individual core/shell PbS/CdS and InAs/CdSe dots [16], furthering the theory that processes governing stochastic blinking in colloidal dots are universal, and insensitive to microscopic material properties and possibly better characterized by physical properties like shape, surface passivation and the local chemical environment. It is also hypothesized that the blinking events are linked to dot charging, but no experiment to date has directly shown this. A full understanding of the blinking mechanism remains the longest outstanding question

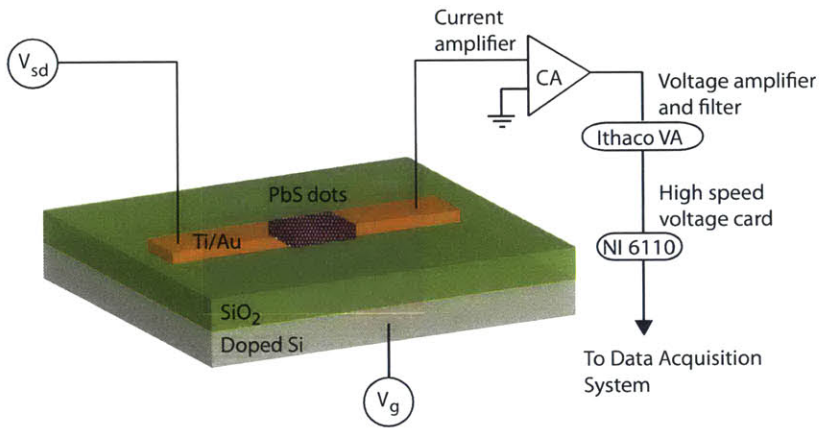

Figure 3-3: Schematic of a typical device structure for two probe transport and noise measurements on nanopatterned colloidal quantum dots. For measurements on nanopatterned arrays of dots, gold electrodes are patterned with electron beam lithography. The dots are placed only in the area between the electrodes.

in colloidal quantum dot photophysics.

3.3 Device Fabrication

A schematic of the typical substrate structure is shown in Figure 3-3. The nanopatterns are measured in an inverted FET geometry with the pattern serving as the channel. We use a degenerately doped n-type or p-type silicon substrate as a back gate and thermally grown SiO_2 serves as the gate dielectric. As the majority carriers in most quantum dot arrays are holes, conventional transport measurements use an n-type silicon substrate. Our charge sensing measurements discussed in the next chapter make use of a n-channel silicon MOSFET as a sensor, which consists of a p-type silicon substrate and 100 nm of SiO_2, so a large number of patterns discussed in this chapter use the same configuration. While the type of doping in the substrate does not impact transport measurements on the dots, the oxide thickness and the corresponding leakage does. For gate voltage measurements, patterns are made on 300 nm of SiO_2 in order to minimize gate leakage. Two Ti/Au electrodes are patterned using electron beam lithography, and serve as the source and drain. The thickness of the Ti and Au layers is 7 nm and 50 nm respectively. Gold is chosen as the primary electrode because it is inert and is expected to form ohmic contacts with PbS dots.

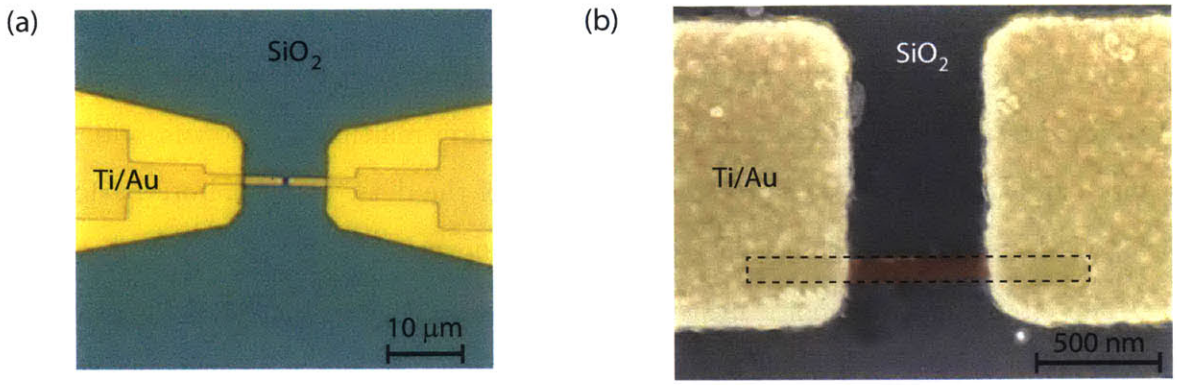

Figure 3-4: (a) Optical microscope image and (b) false color scanning electron micrograph of patterned gold electrodes and 80 nm wide butylamine capped PbS dots on 300nm of SiO_2.

Figures 3-4(a) and (b) show an optical microscope image and a scanning electron micrograph of the device structure on 300nm of SiO_2. The separation between the gold electrodes is 600 nm, and they are 500 nm wide. We create the nanopatterns using the procedure outlined in chapter 2, using a 100 nm thick resist layer.

3.4 Instrumentation

Following the fabrication sequence described in the previous section, we glue the device to a chip carrier in the nitrogen environment of the glovebox, using silver epoxy EE-129J from EpoTek. This silver epoxy requires 24 hours to cure, and is the only type which cures at room temperature. To contact the substrate, which serves as the back gate, we wire bond to the back of the chip carrier. The dots are briefly exposed to air during wirebonding, and care is taken to minimize this exposure. We perform low temperature measurements in a Janis SuperTran VP He^4 flow through cryostat. After loading the sample in the cryostat, we pump and purge the sample space multiple times with ultra high purity Helium. The sample sits in Helium gas, and liquid helium cools the walls of the sample space which then cools the sample through the exchange gas. We monitor the sample temperature with a d670 Silicon diode which sits in the sample space. We control the temperature with a resistive heater located in the area which receives liquid Helium, and a Lakeshore 331 Temperature controller. The

cryostat is retrofitted with 12 coaxial cables from Lakeshore. As we need to measure highly resistive samples, we ensure that the resistance path to ground is $\geq 10^{12}$ Ω. We found that our cryostat developed small leaks after multiple cooldowns, which can cause oxidation and water vapor contamination of the dots. We therefore perform a leak check using a leak detector before every cooldown.

The circuit used for noise measurements is as shown in Figure 3-3. We supply a DC voltage to one terminal using a Yokogawa 7651 (0-30 V), and use a Keithley 2400 voltage source (0-100 V) to supply the back gate voltage. We measure the current using a low noise Femto 400 kHz bandwidth amplifier with a fixed gain of 10^7 V/A. The amplifier is mounted fairly close to the coaxial connectors at the top of the cryostat, in order to minimize the size of the measurement circuit loop and circuit noise. The output of the current amplifier, after being further filtered and amplified by an Ithaco 1201 voltage amplifier with a variable gain (10-10^4) is fed into a NI-6110 high speed card. We use digital sampling techniques, such as box car averaging, to eliminate digital noise originating from the high speed cards.

3.5 Results

3.5.1 Bias and gate voltage dependence

Preliminary I-V measurements on 80 nm wide nanopatterns of butylamine capped PbS dots, at room temperature, show large fluctuations in the current. The current is almost immeasurable ($<$ 200 fA) for source-drain bias voltages less than 10 V for most devices, but increases non-linearly with applied field. Figure 3-5(a) shows a scanning electron micrograph of the 80 nm wide nanopatterns along with the current-voltage characteristics at room temperature. Given the size of each dot to be between 4.3 and 4.6 nm and the inter-dot separation to be approximately 1 nm, the pattern is approximately 120 dots long, 16 dots wide, and the thickness of the film is about 4 monolayers.

We measure the current as a function of time for fixed source-drain bias, and find

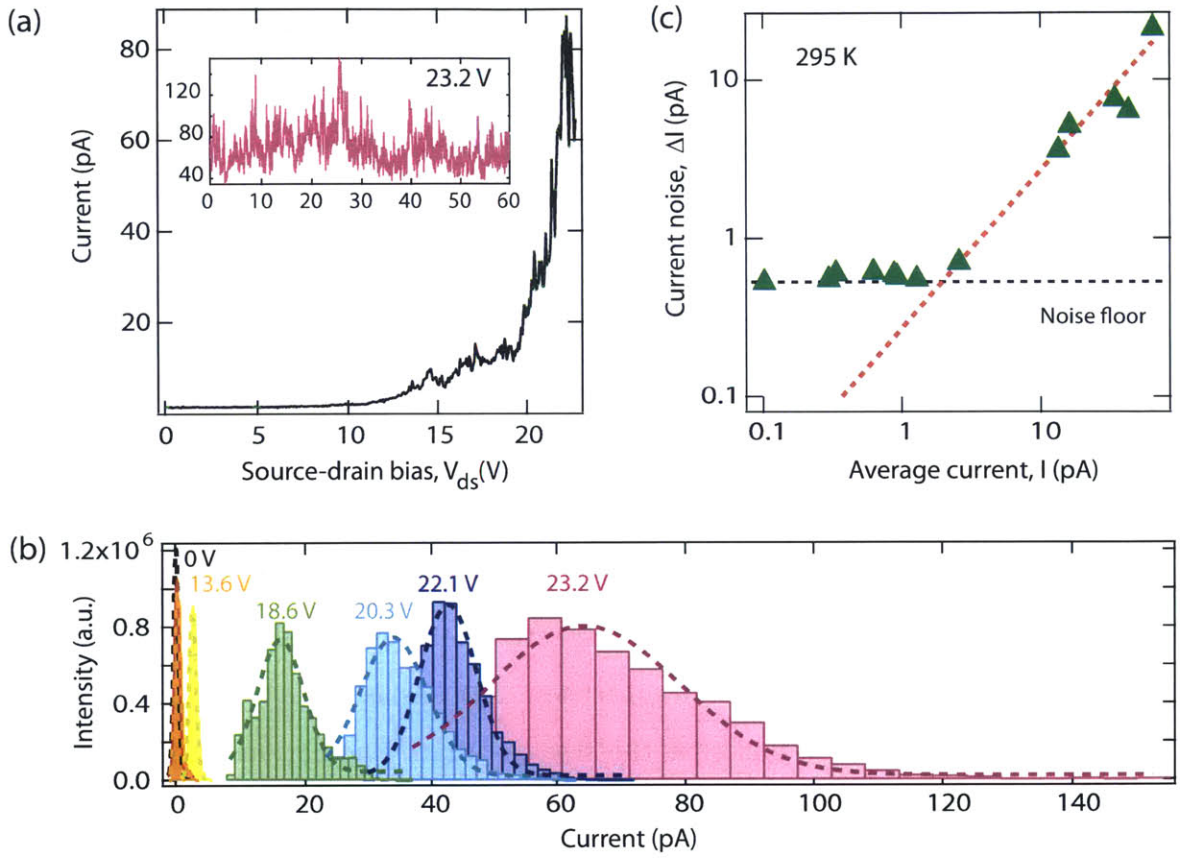

Figure 3-5: Current-Voltage (I-V) characteristics of nanopatterned PbS dots. (a) I-V curves for 80 nm wide pattern showing excess noise in the current. Inset shows noise in the current in the time domain at a source drain bias of 23.2 V. (b) Histogram of the current measured as a function of time for different values of the source drain bias, as indicated in the figure. The dashed lines in the histograms are Gaussian fits. The current noise, ΔI, is given by the full width at half maximum from the fits. (c) Log-log plot of the current noise, ΔI, extracted from the histograms, as function of the average current, I. We see the the excess noise is proportional to the average current. The black dashed line denotes the noise floor of our circuit, and the red dashed line is a linear fit to the data above the noise floor.

that the fluctuations can sometimes to be as large as the current itself. A time trace for $V_{ds} = 23.2$ V is shown in the inset of Figure 3-5(a). We histogram the time traces for different source-drain biases. In a histogram, while there is no 'best' number of bins, different bin sizes can reveal different features of the data and typically one starts with equal bin widths. Since all our time traces have equal numbers of points, we use a bin size, k, that is implicitly based on the range of data. If N is the number of points in the time trace, then the most commonly used method is to set the number of bins, n, to be equal to $\sqrt{N}$. For normal distributions, a better approach is to set the number to be equal to $log_2 N + 1$. The bin size is then calculated by

$$k = \frac{max(x) - min(x)}{n} \tag{3.5}$$

where, x(t) is the signal, n is the number of bins for the histogram and k, is the bin size. We then fit the histograms to a Gaussian distribution and extract an average current (I) and fluctuations in the current (ΔI) from the mean and full width at half maximum (FWHM) of the distribution, respectively. Figure 3-5(b) shows histograms of the current for different source-drain biases. The dashed lines represent gaussian fits to the histograms. We find that the size of current fluctuations, (ΔI) given by the FWHM, increases with increasing source-drain bias. When we plot the current noise ΔI as a function of the average current, I, we find that the amplitude of the fluctuations scale almost linearly with the average current from which we infer that it is the differential conductance that is fluctuating. Figure 3-5(c) shows this dependence on a log-log scale. The black dashed line represents our instrument noise floor, and the red dashed line is a linear fit (ΔI/I ~ 0.3) to the data points above the noise floor extrapolated to zero bias.

We find the power spectral density of the noise at very low frequency to be of the form $1/f^{\gamma}$, with $\gamma \approx 1.4$. This is easily seen when we plot the magnitude squared of the Fourier transform as a function of frequency on a log-log scale. Figure 3-6(a) shows this dependence and also how the amplitude of the $1/f^{\gamma}$ noise grows with increasing source-drain bias, while the exponent γ remains almost unchanged. Other

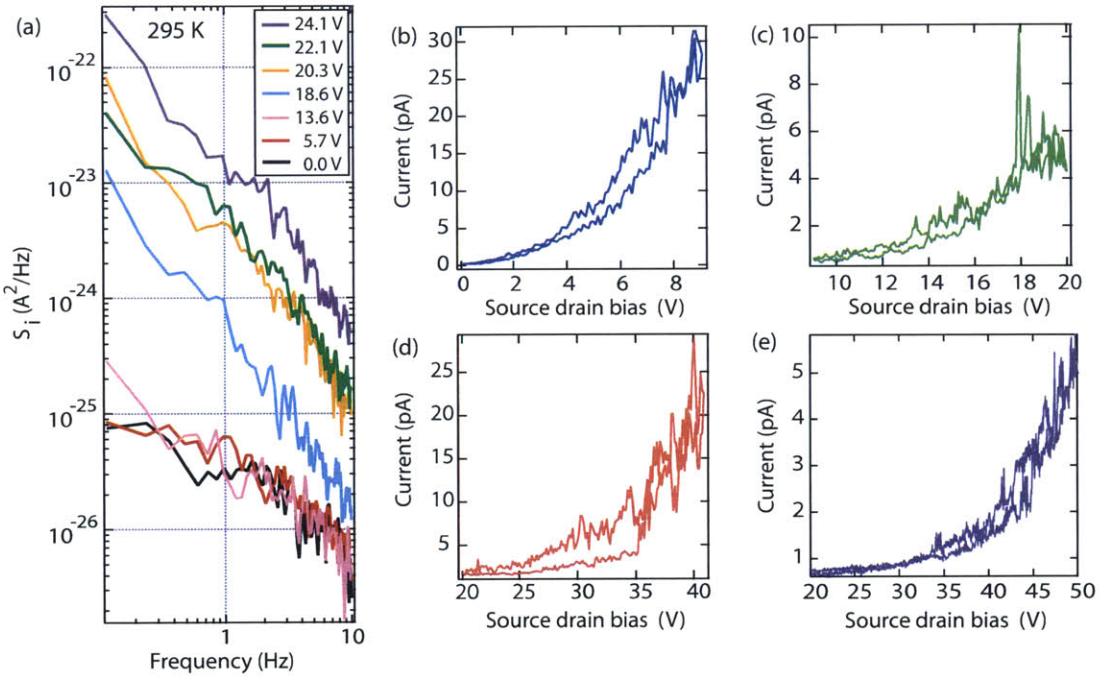

Figure 3-6: (a) Power spectral density of current noise, S_i, in units of A^2/Hz as a function of increasing source-drain bias, showing 1/f noise below 10 Hz. The magnitude of 1/f noise increases with increasing source-drain bias. (b)-(e) show I-V measurements on nominally identical 80 nm wide butylamine capped PbS nanopatterns. While the dimensions of the nanopatterns are the same, (b) and (c) are made on 100 nm thick SiO_2, whereas (d) and (e) are made on 300 nm of SiO_2. The differential conductance ranges from $10^{-12}\Omega^{-1}$ for (b), to immeasurably small ($>10^{-14}\Omega^{-1}$) for a significant number of devices.

groups that observe 1/f noise in HgTe and PbSe dots, attempt to quantify the noise mainly by estimating Hooge's parameter α_H from equation 3.3. They find that the calculated values are one to two orders of magnitude higher than the expected value and claim higher noise in colloidal dots. From our data, $i^2_{1/f} = 1.7\times10^{-23}$ A^2/Hz for $f = 1Hz$, which gives us $\alpha_H/N_c \approx 8.4\times10^{-3}$, where N_c is the number of carriers in the film. If we assume one carrier per dot, this gives us $N_c \approx 10^3$ for our nanopattern. This would imply $\alpha_H \approx 8$, which is three orders of magnitude higher than the Hooge's expected value. However, it is important to note here that Hooge's equation is found to be applicable mainly to ohmic conductors, and in general is not expected to be true for disordered and non-linear conductors, as discussed in sections 3.1 and 3.2. The only piece of information then gained from this comparison is that the dots are significantly noisier than an ohmic resistor of comparable magnitude.

We propose that the large noise reflects the small number of current paths in our nanopattern. We expect that because of their small number, changes in the conductance through any of these paths will affect the transport substantially. This may be supported by the observation that there is a large sample to sample variation in the conductance of these narrow patterns, while the noise characteristics remain unchanged. Figure 3-6(b)-(e) shows current-voltage characteristics for a few nanopatterns. While the dimensions of the nanopatterns are the same, (b) and (c) are made on 100 nm thick SiO_2, whereas (d) and (e) are made on 300 nm of SiO_2. We measured 65 nanopatterns, and find the highest differential conductance to be $10^{-12}\Omega^{-1}$ from figure 3-6(b). For twelve of the nanopatterns, we were unable to measure any current even with 50 V across the device which puts the differential conductance at $< 10^{-14}\Omega^{-1}$. Because of these small values, we apply a relatively high source-drain bias in order to measure current. In the FET geometry with Si substrate as the back gate, applying a relatively high bias also has the effect of non-uniformly gating the sample, where the effective gate voltage at one end is equal to $-V_{ds}$. Non-uniform gating of the sample can also explain the lower differential conductance for samples fabricated on thicker SiO_2.

In order to distinguish the gate voltage dependence from the bias dependence

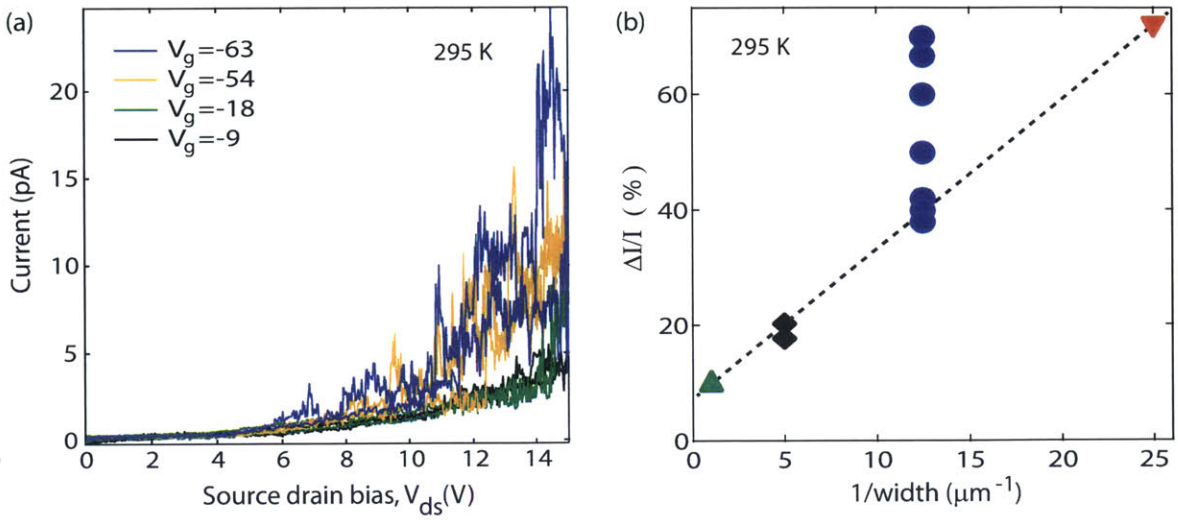

Figure 3-7: (a) Noise as a function of gate voltage at room temperature. As seen from the current-voltage characteristics, the noise increases with increasing gate voltage (V_g), but this can be seen clearly only when the applied gate voltage is larger than the source-drain bias. (b) Percentage fluctuation in the current, for different pattern widths, with constant electrode spacing. Multiple data points for a single width represent the sample to sample variation. The line serves as a guide to the eye to show that the noise scales inversely with the width of the pattern.

we have to apply a gate voltage, $V_g >> V_{ds}$. This is non-trivial because of leakage through the oxide which is comparable to the device resistance. As a result, we are able to see a gate voltage dependence of the noise for very few devices where we are able to measure current at relatively low source-drain biases. Figure 3-7(a) shows the I-V curves at different gate voltages. We see that as we apply a more negative gate voltage the dots become more conducting, consistent with holes as the majority carriers. We find that the noise increases almost linearly with increasing current, just as we saw for the source-drain bias dependence.

Wider patterns with the same separation between electrodes also show excess noise, but the magnitude of the fluctuations appear to be much smaller. Figure 3-7(b) shows the percentage fluctuation in the current ($\Delta I/I$) for different pattern widths at room temperature. Multiple data points for a single width represent data collected from different devices. The wider patterns are made identically and have a thickness variation of $\pm$ 20 nm from sample to sample. Despite the large sample-to-sample variation, illustrated for samples of width 80 nm, the general trend, that the

noise is smaller for wider samples, is clear.

From this section, we conclude that the noise is caused by conductance fluctuations in individual current paths in the system. The noise increases almost linearly with increasing current. The fluctuations in the current appear to be too large for all rows of dots to be participating equally. It is then possible that the magnitude of the noise can grow to a significant fraction of the average current because of the small number of current paths in the system. As the number of conduction channels is increased, by increasing the width and thickness of the patterns, the amplitude of fluctuations decreases. Any description about the mechanism causing the noise is difficult without studying the temperature dependence of the noise.

3.5.2 Temperature dependence of noise

The temperature dependence of the noise in 80 nm patterns can only be measured at very high fields because the average current freezes out at low temperatures, making it impossible to cover the whole temperature range at low source-drain bias. Figure 3-8 shows histograms of the current at fixed source-drain bias, V_{ds} = 25 V, for different temperatures. At this high field, we observe that the average current is weakly temperature dependent, and the strongest temperature dependence of the average current is seen above 180 K, where the histogram widths start to increase rapidly as well.

In order to measure the current at relatively lower fields for the temperature dependence, we study patterns that are 200 nm wide and have the same separation between electrodes. Figure 3-9(a) shows I-V curves for a 200 nm wide patterns. For this device, the fluctuations in the current become immeasurably small below 180 K. Figure 3-9(b) shows the average current. I_{av} and current noise, ΔI, for V_{ds} = 15 V extracted from gaussian fits to time traces, as a function of 1000/T. As the temperature is controlled by adjusting the heat input into the system, the heater power supply acts as a variable noise source at all temperatures giving a randomly fluctuating noise floor. The current noise from the nanopattern is expected to be uncorrelated with the heater noise and other circuit noise, and since two uncorrelated

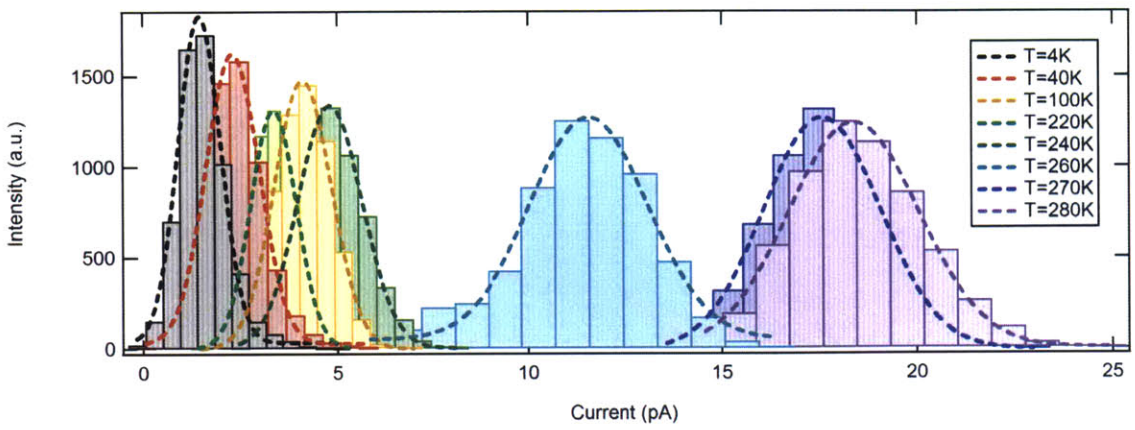

Figure 3-8: Histograms of the current at fixed source-drain bias, V_{ds} = 25 V, as function of temperature for 80 nm wide butylamine capped PbS nanopatterns.

noise sources add in quadrature, we can subtract the heater noise from our data at every temperature. We measure the noise at zero bias for each temperature, and this gives us the noise background to be subtracted. The source-drain bias data are collected at room temperature with the heater disconnected, and all other instrument sources of noise do not change with bias as can be seen in Figure 3-5(c), so this correction is not applied for the room temperature data.

If we now look at the average current as a function of inverse temperature, we find that it does not fit to a straight line for the whole temperature range. The interesting observation is that the noise current follows the average current, consistent with what is expected for a conductance fluctuation. Because of the high resistance in these devices, we are only able to measure transport in a regime where it would be dominated by the high field. In the next chapter we present results of transport measurements in the zero bias regime for these highly resistive dots, using a nanoscale charge sensor, and explore the temperature dependence of the current in detail.

3.5.3 Effect of changing the ligand

The next question we ask is if the noise depends on the passivating ligand on the surface. Any dependence of the noise on surface passivation would imply that the noise or conductance fluctuations happen at the surface of the dot. Given the patterning

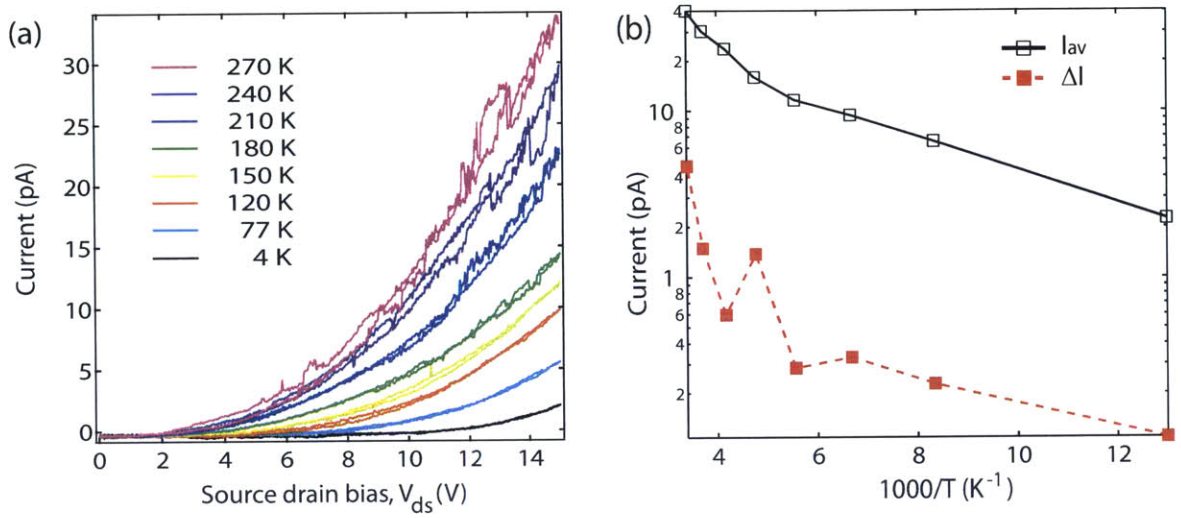

Figure 3-9: (a) Current-voltage characteristics of 200 nm wide butylamine-capped PbS nanopatterns for different temperatures. (b) Average current, I_{av} (black squares), and current noise, ΔI (filled red squares), at V_{ds} = 15 V as a function of 1000/T, where T is the temperature. The current noise, ΔI, follows the average current just as one would expect for conductance fluctuations. The lines serve as guide to the eye.

constraints discussed in section 2.5, we are unable to move to shorter ligands, and so we move to the longer native oleic acid ligands. Changing to these long ligands increases the tunneling distance by almost a factor of 2, and the resistance goes up exponentially with the distance and a possible increase in barrier height which is difficult to estimate. Because of the expected high resistance, there have been no reports of transport measurements on unannealed oleic acid capped PbS dots. As discussed in section 2.7, our patterning technique is expected to improve the conductance by almost two orders of magnitude, enabling us to make the first transport measurements on nanopatterned oleic acid capped PbS dots, which are on average two to three orders of magnitude more resistive than butylamine capped PbS dots.

We measure 200 nm wide patterns for these ligands, which, because of the increased inter-dot spacing, gives us approximately the same number of dots in each row as the 80 nm patterns with the short ligand. Figure 3-10 shows the current-voltage characteristics for a range of temperatures. At room temperature, we see current fluctuations which grow with increasing source-drain bias. As we cool down to lower temperatures, the noise becomes smaller. These observations seem consis-

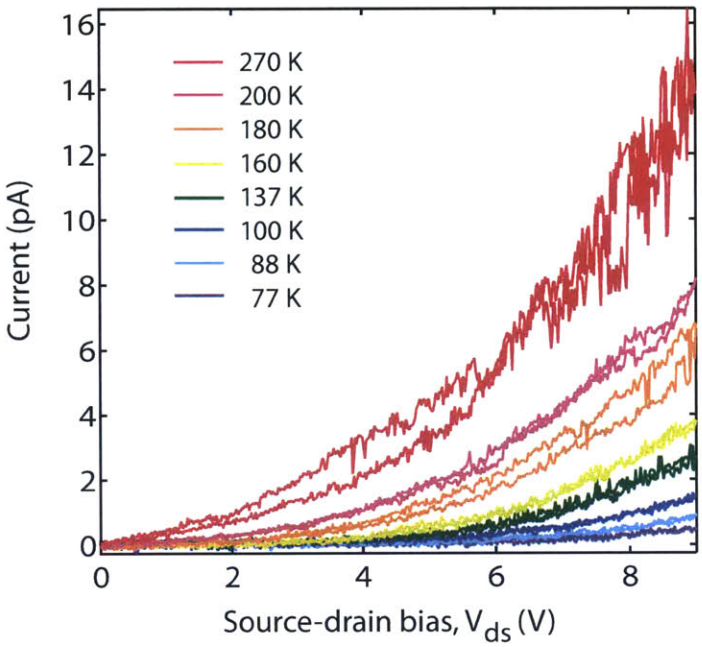

Figure 3-10: Current-voltage characteristics for 200 nm wide nanopatterns of oleic acid capped PbS dots. Note the telegraph nature of the noise.

tent with what we expect from measurements on shorter ligands, and at first sight it appears that only the average current is smaller because of the height and width of the tunnel barrier. However, the time traces at fixed source-drain bias as a function of temperature, provide a surprise.

Measuring the noise in the frequency domain, we find 1/f noise at room temperature, but as we cool down, we see a crossover to telegraph noise. From the telegraph noise we can then extract statistics for the on and off times. Figure 3-11(a) shows small snippets of the time traces at 295 K, 230 K, 200 K and 180 K. We subtract the average current, I_{av}, in order to quantify the size of the fluctuations. We see that not only do the telegraph switches grow in amplitude with increasing temperature, but also they become faster. It is important to point out that we see telegraph events over a period of multiple days and multiple cooldowns. Interestingly, we find that at a given temperature and source-drain bias, the switching rate becomes slower over extended periods of time. Figure 3-11(b) shows snippets of the time traces at 200 K taken on the first and third day of measurements.

Another surprising finding is that the probability distribution for the on and off

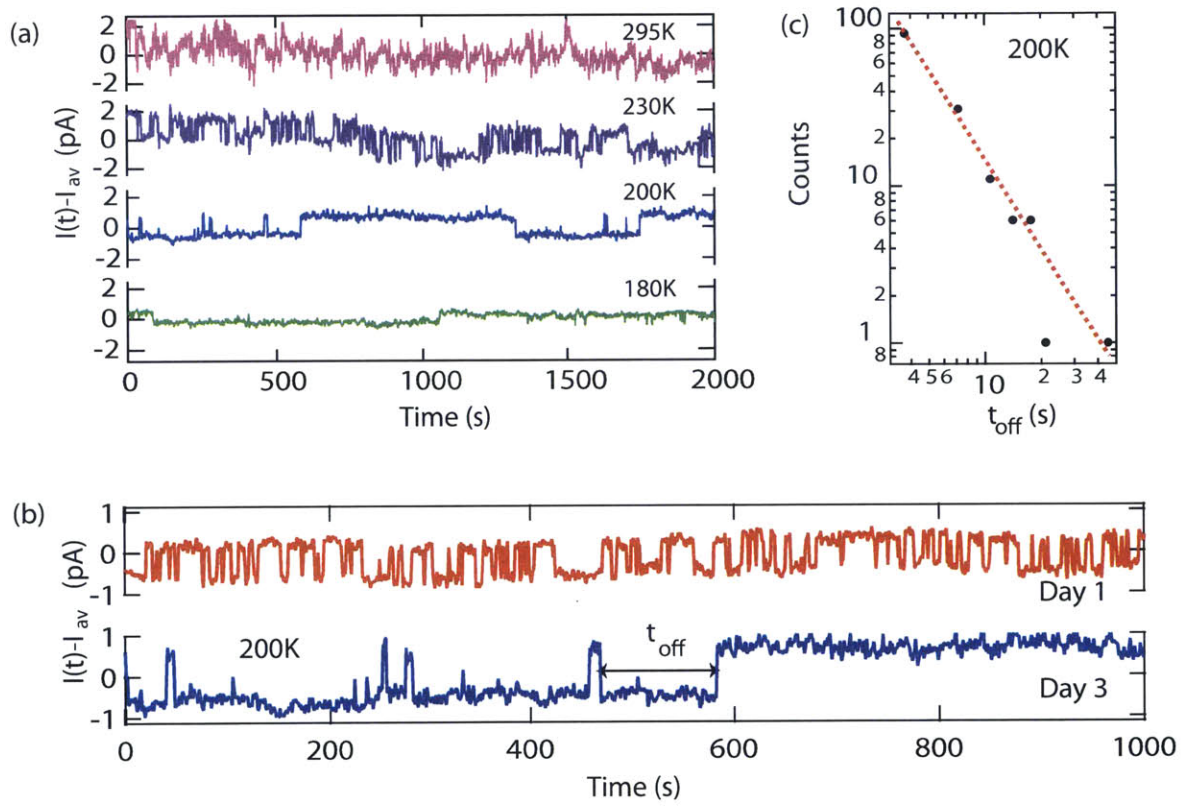

Figure 3-11: (a) Current measured as function of time at different temperatures, for 200 nm wide nanopatterns of oleic acid capped PbS dots. (b) Telegraph events are most clearly observed at temperatures below room temperature, and the switching rate decreases with extended measuring time. Top and bottom traces show switching events on the first and third day of measurement. The average current is subtracted from all of the time traces for ease of comparison. (c) Histograms of the off times on a log-log plot fit well to a power law, $\mathrm{p}(\mathrm{t}_{off}) = \mathrm{A}/t_{off}^{1+\mu}$, with $\mu = 0.6$.

times is better fit to a power law than an exponential. Figure 3-11(c) shows a power-law fit for the off times to $p(t_{off}) = A/t_{off}^{1+\mu}$, with $\mu = 0.6$. It is then likely, that the 1/f noise at room temperature originates from a superposition of many telegraph like processes each with a power law distribution. The temperature dependence of the telegraph events reveals that the system shows longer on and off times as we go to lower temperatures, and this effect is not clearly understood. The large error bars resulting from observing a small number of switching events at lower temperatures, makes it difficult to make a conclusive statement about the temperature dependence of the power law exponent. As mentioned in section 3.2.1, power law distributions are commonly seen in blinking from CdSe dots. To our knowledge, transport signatures of blinking have never been observed.

3.5.4 Hysteresis and memory effects

The increase in off times observed above suggest that the sample has a memory of the application of a voltage. It is therefore not surprising that, as we measure the oleic acid capped PbS arrays we observe hysteresis and memory effects. In order to study these effects, we sweep the source-drain bias to a fixed voltage, V_f. We then monitor the current for a fixed amount of time, and sweep the voltage back to zero. Figure 3-12(a) shows current-voltage characteristics acquired in this manner for a range of temperatures. The solid red lines for each temperature show data recorded during the sweep up to $V_f = 16$ V. The dashed black lines show the data as we sweep the voltage down, after holding at V_f for one hour at each temperature. Figure 3-12(b) shows the time traces for a fraction of the wait time. At low temperatures, 100-130 K, we see that there is almost negligible hysteresis between the sweep up and sweep down. At 140 K, the sweep up and down curves start showing hysteresis, and this grows greatly with temperature. At a temperature of 270 K, the current drops by almost 50 percent as a function of time.

As seen in Figure 3-12(b), the decay of the current at fixed high voltage as a function of time is not exponential. The largest drop seems to occur within the first few seconds, and then the amplitude and rate of the decay process slows down with

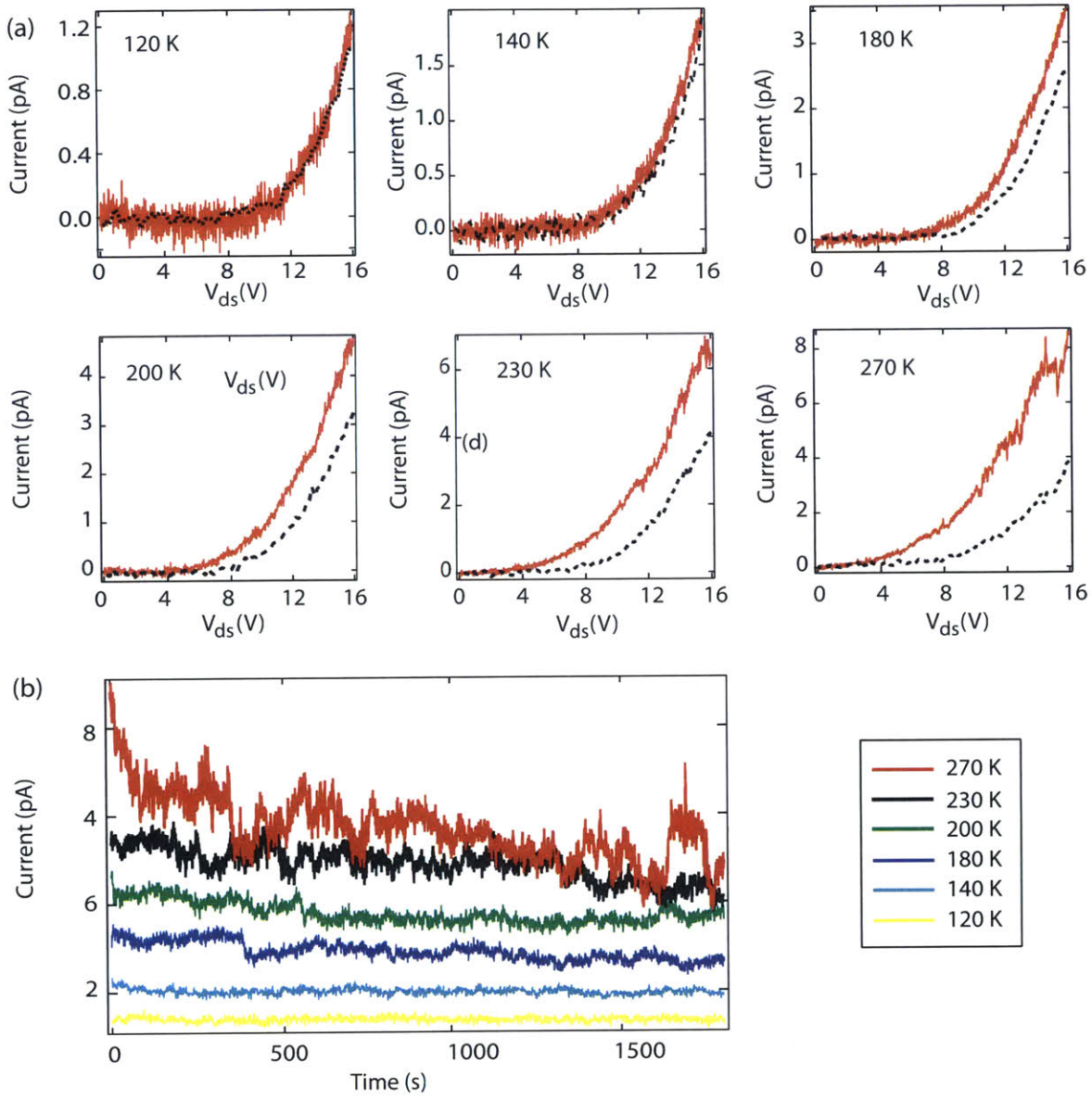

Figure 3-12: (a) Hysteresis in current-voltage characteristics of oleic acid capped dots. Red solid lines depict the current as the source-drain bias is raised from 0 to 16 V. We hold the voltage at 16 V for 1 hour and turn the source-drain bias down to 0 V again. Black dashed lines denote the current measured during the sweep down. (b) Current as a function of time for different temperatures, immediately after sweeping the source-drain bias up to 16 V.

time, and eventually we reach a state where the current does not change appreciable on experimentally measurable timescales. While this effect was first seen for oleic acid capped dots, it has been since verified that it exists for all measured patterns.

Consistent with this large hysteresis are memory effects. If at a fixed high temperature, say 270 K, we sweep the source-drain bias to voltage V_1, allow the current to stabilize such that it does not change appreciably on the timescale of several minutes, say I_1, and then sweep the voltage down, we observe hysteresis as the current drops from I_1 to 0. If we then repeat the same experiment again and sweep up to voltage V_1, we measure current I_1 which then decays to a lower current I_2, as shown in Figure 3-13. Power law decays for the current have been previously reported in CdSe dots [73, 74], where the decay exponent depends on temperature, dot size, capping layer, and gate oxide thickness.

We find that the current can be restored by annealing at an elevated temperature. To quantify this effect, we measure the current-voltage characteristics of a 200 nm wide butylamine-capped PbS nanopattern at room temperature, and heat the sample under vacuum to 303 K, while continuously monitoring the current. We find that the current increases with temperature, but the increase is much larger than simply expected from the temperature dependence. Once the temperature stabilizes and the current starts to decay, we remove the source-drain bias, and let the sample relax overnight to room temperature. We find that the current stays at the elevated value at room temperature as well. Figure 3-14(a) shows the current-voltage characteristics before (black dashed line) and after (red line) heating the sample to 303 K. Figure 3-14(b) shows the current measured as a function of time while heating. The shaded region shows the current as the temperature increases from 295 K to 303 K. From the temperature dependence of the current at lower temperatures, we expect the current to increase from 3.5 pA to 3.6 pA as the temperature is raised to 303 K, instead of the observed 7.5 pA.

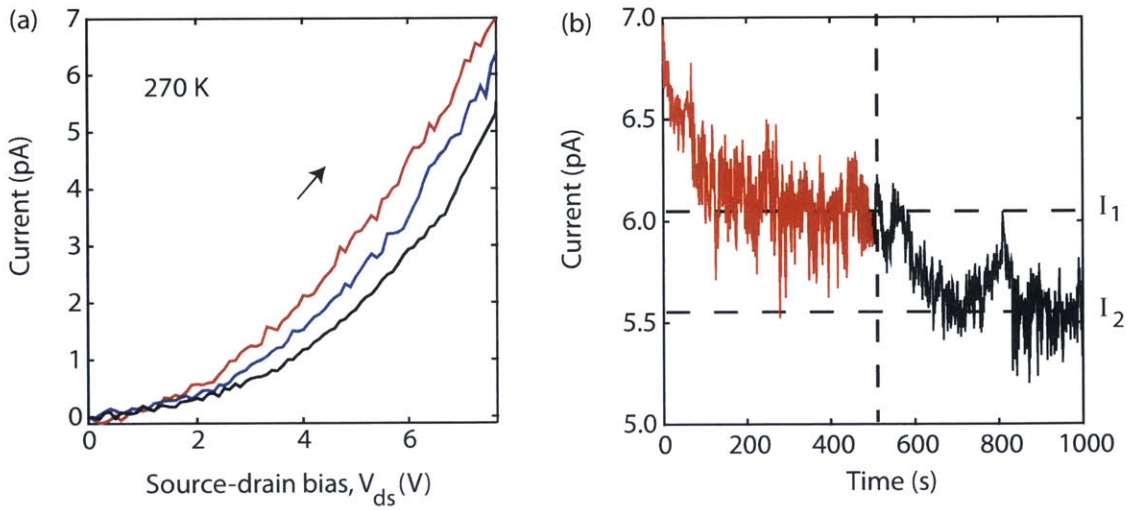

Figure 3-13: Memory effects: (a) Current as the voltage is swept from 0 to 8 V for a 200 nm wide pattern of butylamine capped dots. The red trace is the first sweep up to 8 V. We then measure the current as a function of time for 10 minutes (plotted red in (b), and then sweep the voltage down. The sweep down, not shown in the figure, coincides exactly with the blue trace. The blue curve is the second sweep up to 8 V. Once again we measure the current as function of time (plotted black in (b), and then sweep the source-drain bias back to 0 V. The sweep down and subsequent sweep up are represented by the black trace. (b) Current as a function of time. The red time trace shows the current as a function of time after the first voltage sweep. The current decays from 7 pA to $I_1 \sim 6$ pA in 500 seconds. During the next voltage sweep, the system remembers that the current had dropped to I_1, and we observe a decay to a lower value $I_2 \sim 5.5$ pA in 500 seconds.

3.6 Discussion

In this chapter, we studied the current-voltage characteristics of nanopatterned PbS quantum dot arrays. We observe a large noise in the time domain, which is directly proportional to the average current, showing that it results from conductance rather than charge fluctuations. The conductance noise scales inversely with width, growing to almost 75% of the average current for 40 nm wide patterns. In some cases, mainly with the long ligand, the noise is telegraph-like, switching on and off. The off-times have a power law distribution, and so they increase with time leading to an overall decay of the current, which can be partially restored by heating the sample to elevated temperatures. We attempt to explain our results with a model in which the current is

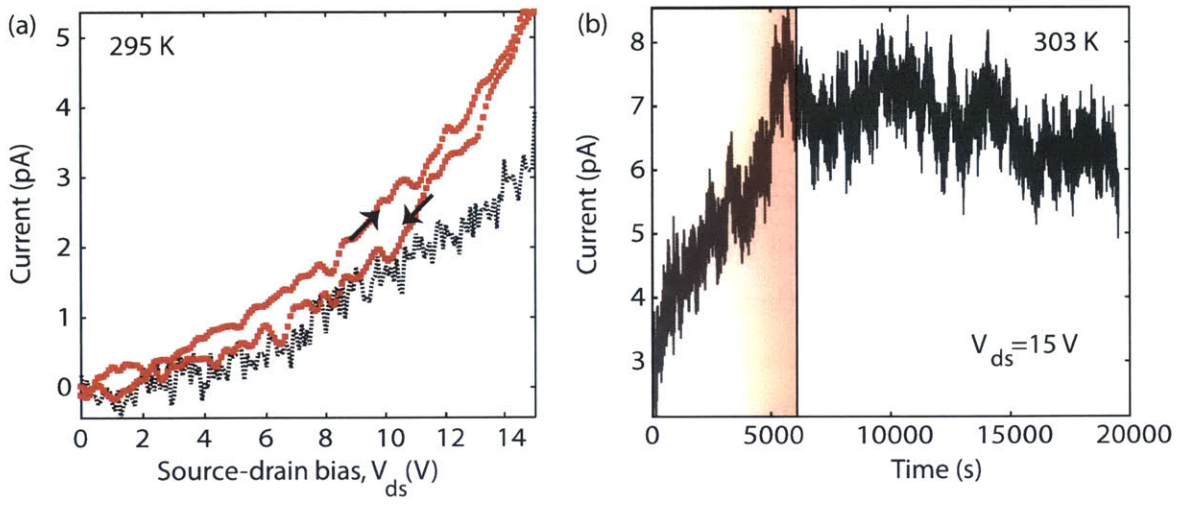

Figure 3-14: (a) Current-voltage characteristics at room temperature, before (black dashed line), and after (red line), heating the sample to 303 K. (b) Current as a function of time for V_{ds} = 15 V. The red shaded region indicates changing temperature.

carried by quasi-one-dimensional paths that can be interrupted by trapping of charge.

The power-law dependence of the off times in the telegraph noise is sometimes called Levy statistics, and has been extensively studied by photoluminescence measurements primarily for CdSe dots [79]. Transport measurements on CdSe dots showed power law decays of the current as a function of time [73]. Novikov *et al.* [82], developed a model for the time decay of the average current first observed in CdSe nanocrystals capped with trioctylphosphine oxide. The authors considered the array to be made of a finite number of conducting channels, and showed that both a decay of the average current and noise can result from a power law tail for the distribution of off-times (τ), given by:

$$p(\tau) = \frac{A}{\tau^{1+\mu}}, 0 < \mu < 1. \tag{3.6}$$

The current is then given by:

$$I(t) = I_0 t^{-\nu}, 0 < \nu < 1, \tag{3.7}$$

where, the exponent ν is given by 1-μ. The expected noise spectrum for Levy statis-

tics is given by a power law in frequency, or $1/f^{\alpha}$ noise in contrast to white noise expected for a Poissonian channel [81]. It was, however, suspected that the behavior was not generalizable, because CdSe films were found [74] to have blocking contacts to Ti/Au, and it was thought that the decay of the current might be a contact effect. From our observation of telegraph events in oleic acid capped PbS dots, we find power law distributions for the wait times, with $\mu \sim 0.6$ as given by equation 3.6. The power law decay of the current observed at higher temperatures is described well by equation 3.7 with $\nu \sim 0.4$. We are then able to verify the proposed relation between the exponents. The observed $1/f^{\alpha}$ noise spectra, with an exponent α similar to the exponent for the current decay highlights the good agreement with the theoretical model discussed above. Our observations then suggest that the limitation of current by quasi-one-dimensional channels and its noise and decay may be general features of colloidal quantum dot arrays. This broader conclusion is also supported by recent reports of blinking in single PbS dots measured with time-resolved intermittent contact conductive atomic force microscopy [64] and infrared spectroscopy [16].

Following the arguments of Ambegaokar, Halperin and Langer (AHL) [1], for variable range hopping in disordered semiconductors, the high resistance of the barriers between dots results in exponentially small tunneling rates between dots. Small variations of the tunnel barrier heights and widths will therefore result in exponentially large variations in tunneling resistances. The AHL recipe for calculating the overall resistance with such an exponentially broad distribution of microscopic resistances is to begin with the smallest resistors and put in successively larger ones until a percolation path is created across the sample. Such a path is necessarily quasi-one-dimensional. If a resistor in the critical path switches between two values of resistance and if there are only a small number of parallel paths in the sample, telegraph noise will be seen.

To gain an insight into the physical mechanism behind Levy statistics, we briefly review the proposed mechanisms for blinking in CdSe dots. Blinking in individual quantum dots has been associated with the charging of dots [79]. Presumably, an electron (or hole in the case of our p-type dots), gets trapped in a localized state,

and the resulting charged quantum dot does not respond to the photoexcitation as it did when neutral. We assume that trapping of charge also strongly modifies the resistance along the percolation path. That trapping is the cause of the overall decay of the current is substantiated by raising the temperature after the average current is allowed to decay. We find that such annealing restores part of the lost current.

If we assume the existence of multiple traps near a quantum dot, which can localize a carrier, in the vicinity of a trapped electron, the coulomb field can cause misalignment of energy levels of the dots, causing the conduction channel to close. The conduction channel can open up once the trapped electron escapes. For an exponential distribution of trap states, only thermally activated electrons or holes can escape the trap site. Electrons trapped in deep trap states will then be released on exponentially longer time scales than those in shallow trap states, resulting in an overall power law distribution. However, this picture requires a large trap density in the vicinity of each dot. A second picture is tunneling to the trap sites. Tunneling has been discussed a lot in the context of blinking in CdSe dots, as the power law for blinking was found to be almost independent of temperature. From a simple WKB picture, the tunneling rate can be estimated as:

$$r_{tunnel} = Ae^{-2.\sqrt{2m^*\Delta E/\hbar^2}L} \tag{3.8}$$

where, r_{tunnel} is the tunneling rate, A is the attempt frequency, m^* is the effective electron mass, ΔE is height of the barrier and L is the barrier width. Fluctuations in the barrier height and width, coupled with the assumption that as a charge tunnels on to the trap, the barrier may change during the tunneling off process, can give a distribution of tunneling rates.

To conclude, large fluctuations are seen in the current measured in nanopatterned PbS arrays, with a finite number of conductance channels. The statistics of these fluctuations are similar to those observed from fluorescence blinking in colloidal dots, which suggests a more general origin of these fluctuations. The results are understood in the context of a model in which a quasi-one-dimensional percolation paths is turned

on and off, by charging of a dot along the path.

Chapter 4

Charge sensing in PbS colloidal quantum dots

In this chapter we discuss the integration of a narrow channel MOSFET as a charge sensor with nanopatterned PbS quantum dot arrays. The sensor can be used to measure the conductance of the nanopatterned array, by a time resolved measurement of charge, and to study the noise or fluctuations discussed in the previous chapter. In the first section, we give a brief overview of the existing techniques to study transport in colloidal quantum dot arrays, and motivate the need for a new technique to probe transport. In section 4.2, we describe how we can use our sensor to measure high resistances in a nearby nanopattern. We also briefly discuss the range of resistances that can be probed with this technique. In Section 4.3, we present conductance measurements on butylamine capped PbS dots measured with this technique, as a function of temperature and field. In section 4.4, we present the first conductance measurements on unannealed nanopatterned arrays of PbS dots capped with the native oleate ligand. The resistances measured in both these sections are the highest measured for colloidal quantum dot arrays. We discuss our results for PbS dots, in terms of having a tunable artificial solid, in section 4.5. Finally, in section 4.6, we discuss future prospects of the use of our charge sensors, including how they can be used to study noise and fluctuations in colloidal dots and other nanoscale systems.

4.1 Measuring transport in colloidal quantum dot arrays

Electronic transport in colloidal quantum dots has been studied both theoretically and experimentally for almost a decade. As discussed in Chapter 1, the important pieces of theoretical framework have been developed, for other disordered semiconductors by Mott, Efros and Shklovskii, and others. Experimentally, many different configurations have been used to investigate the system properties and also realize the theoretical models. The simplest configuration is a three terminal device, a field effect transistor (FET). In the geometry analogous to conventional FETs, the dots are dropcast onto patterned source and drain electrodes on a substrate. The electrode configurations may be interdigitated (consisting of several electrode finger pairs) to provide higher current and improved reproducibility, or have nanometer spacings for studying single dot characteristics. Electrodes with gap spacing less than 10 nm are typically created by electromigration. The dots typically cover the entire surface, the dots between the source drain electrodes serve as the channel, and a third electrode separated by an insulating layer is used to modulate the electron density.

The FET geometry has been extensively used to study PbSe [70], CdSe [73, 21] and CdTe [28] colloidal quantum dot arrays. A known challenge with two-probe measurements is that the measured resistance includes contributions from both the sample as well as the contacts. For systems with blocking contacts, such as CdSe dots [73, 21], we can no longer measure transport in this geometry. In order to eliminate contact effects, four probe measurements are used. However, given the high resistances of colloidal quantum dot arrays originating from the large organic tunnel barriers, it becomes increasingly difficult to measure the voltage drop across the dots because of instrument limitations and the need to make the distance between current leads very small.

As discussed in the previous chapters, efforts to form more conducting arrays typically include replacing the long ligands with shorter ones. However, chemical or electrochemical gating methods can also be used to insert charge carriers or increase

the charge density in these arrays [115]. For chemical doping, strong reducing agents such as potassium [125] or sodium [100] are introduced into the array, which donate their electrons to form n-type conducting arrays. However, this process of chemical doping is very difficult to control. Electrochemical gating is performed in a cell which consists of a working electrode, which is the material of interest, in contact with an ionic solution or an electrolyte. As the device is used to measure the electronic conductance of the array, it has two electrical contacts.The electrochemical potential is controlled by applying a voltage with respect to a reference electrode. Charge is injected into the system by electrochemically driving ions into the nano-voids in the array. ZnO [93], CdSe [125] and PbSe [120] quantum dot arrays have been investigated with this technique. A recent trend [115] is to charge the quantum dot array to a certain degree, and then freeze it, in order to study the conductance below the freezing point of the liquid permeating the voids. avoiding parallel conductance in the electrolyte.

Scanning tunneling spectroscopy, in which one measures the current between the STM tip and the dot bound to a conducting substrate, has been primarily used for the study of isolated dots [35, 72]. It has recently been used to controllably contact individual CdSe dots in a multilayer array to study electrical contacts to the array [36]. However, it is not clear that these measurements are possible on arrays thicker than one or two monolayers, as the usual model used in interpreting electron tunneling results starts to break down.

It is important to note that for all the methods described above, vacuum annealing or post deposition ligand exchange techniques have been used to increase the conductivity of the films in order to study transport. The insulating nature of organic ligands typically used in colloidal synthesis results in poor inter-particle coupling, and highly resistive films. While recent improvements in ligand properties, such as the use of molecular metal chalcogenide complexes to generate inorganic quantum dot arrays, have led to highly conducting arrays [50], increased inter-particle interactions between closely packed dots, has led to an increased packing disorder in the films. In order to probe charge ordering or collective effects in an array, we look to mini-

mize the packing disorder, and end up working with very high resistance arrays, that cannot be probed with the methods discussed above. A new direction with colloidal quantum dots are multicomponent superlattices that not only provide the opportunity to probe the unique physics of self-assembling in the nanometer scale but also can potentially be utilized as a 'bottom-up' design tool to build 'meta-materials' of novel physical properties distinct from their individual components [98, 104]. These superlattices are primarily stabilized by ligand-ligand vanderwaal's interactions and therefore are expected to have very high resistances, owing to a large tunnel barrier between dots.

We use a novel technique to study transport in highly resistive colloidal quantum dot arrays, based on a time resolved measurement of charge using a nanoscale charge sensor. This method has been previously used to study transport in highly resistive nanopatterned films of amorphous silicon and germanium [62, 68]. It was recently also shown that this technique is insensitive to contact effects (or blocking contacts) [68]. Our nanopatterning technique described in Chapter 2, makes it very easy to integrate the charge sensor with colloidal dot arrays. To summarize, the charge sensing technique, designed to measure high resistances and insensitive to the nature of contacts, appears to be ideally suited to study transport in colloidal quantum dot systems.

4.2 Conductance measurements using charge sensing

In the study of single electron devices, charge measurement using integrated sensors have been utilized to measure electron dynamics in materials where the electrical current may be immeasurably small [59]. Recently, integrated sensors have been successfully used to study transport in highly resistive amorphous semiconductors [62, 68]. In this novel resistance measurement technique, we effectively measure the charging of the resistive material, and measurement of very high resistances is made

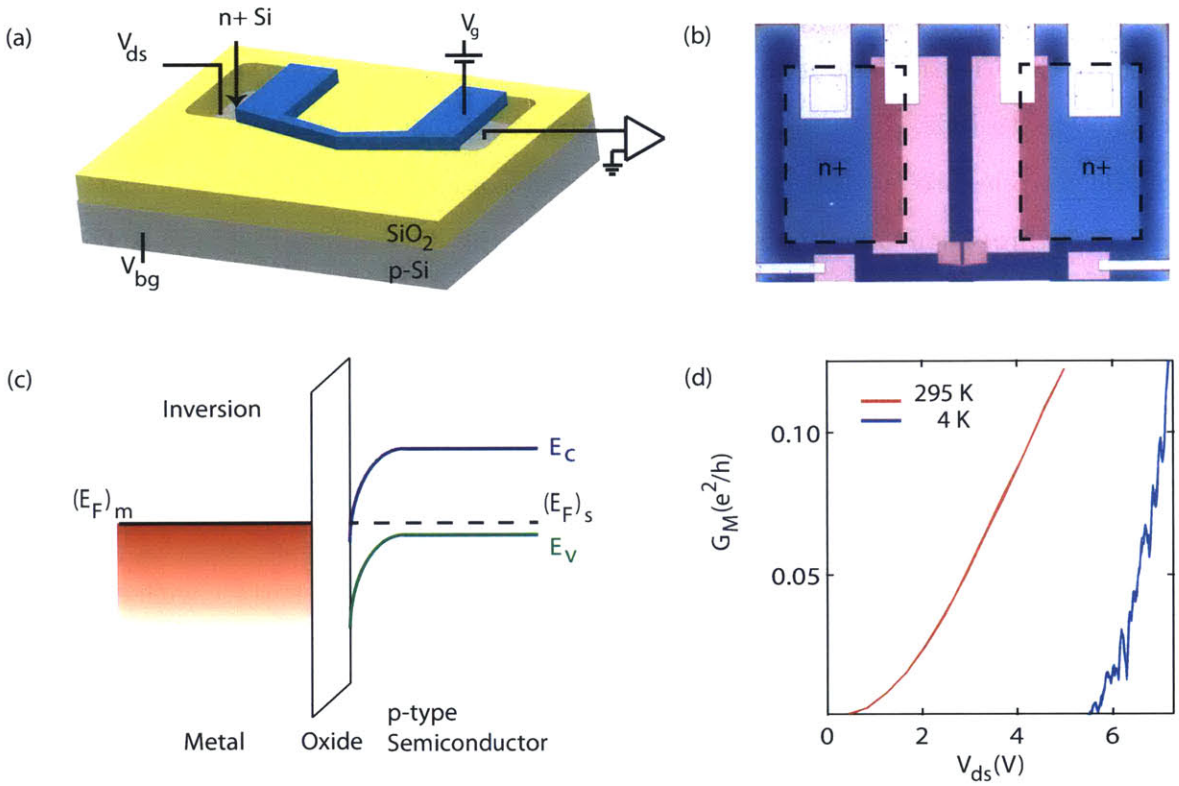

Figure 4-1: (a) Schematic , and (b) optical micrograph of a narrow channel silicon MOSFET. The device consists of an n-channel silicon MOSFET positioned approximately 100 nm away from a nanopatterned array of dots. The gate of the MOSFET tapers to a width of $\approx$ 80 nm wide at its narrowest point and a positive voltage on the top gate induces an inversion channel of a comparable width at the Si-SiO_2 interface.(c) Schematic illustrating the band bending in a n-channel MOSFET for the formation of an inversion region. (d) Conductance of the inversion region, G_M measured with 32 μV ac excitation as a function of voltage applied to the top gate, at 295 K (red) and 4 K (blue).

possible by the extremely small input capacitances achievable with integrated charge sensors. We attempt to extend the applicability of this technique to nanopatterned quantum dot arrays.

We use a narrow channel MOSFET as a charge sensor. The fabrication procedure is discussed in detail in Appendix A; here we quickly review aspects that are vital to an understanding of the charge detection technique. The metal oxide semiconductor (MOS) structure is obtained by growing 100 nm of silicon dioxide (SiO_2) on top of a p-type silicon substrate, and depositing a layer of metal (Aluminum) or n-type polycrystalline silicon. The gate of the MOSFET tapers down to a narrow width

of almost 80 nm so that the MOSFET in sensitive to its electrostatic environment. The MOSFET structure includes two additional terminals (drain and source), each connected to individual highly doped n-type regions on the p-type substrate. Two gold electrodes are fabricated adjacent to the sensor for contacts to the nanopatterned dots. Figure 4-1(a) and (b) show a cartoon of the device structure and an optical micrograph of the fabricated MOSFET.

The initial occupancy of the energy bands in the semiconductor is set by the work function of the gate metal and the properties of the semiconductor. As we apply a positive voltage on the gate, we drive the valence band edge further away from the Fermi level, and holes further away from the gate. At larger gate voltages, we move the conduction band edge closer to the Fermi level, and populate the surface with electrons forming an inversion region at the semiconductor oxide interface, underneath the gate. Figure 4-1(c) shows the band diagram of a MOSFET in inversion. The inversion region extends between the source and the drain of the MOSFET. The threshold for inversion is determined by the work function of the gate metal. As Aluminum and n+ poly-silicon have comparable work functions we use them interchangeably for measurements in this thesis.

In order to characterize our MOSFET, we apply a positive gate voltage V_g to the MOSFET gate contacts, forming an inversion layer underneath. We measure the resistance of the inversion region with a small AC excitation from a Stanford Research 830 lock-in amplifier applied to one of the n+ contacts (source). A 400 kHz Femto current amplifier fed into the lock in, measures the current flowing out of the other n+ contact (drain). Figure 4-1 (d) shows the conductance of the inversion region in units of e^2/h, as a function of the gate voltage V_g for room temperature and 4 K, measured with an AC excitation of 32 μV. From the slope of the curves, we find a field effect mobility of 400 $cm^2V^{-1}s^{-1}$ at room temperature, which increases as we go to lower temperatures. As the MOSFET gate tapers down to a very narrow width, we observe reproducible conductance fluctuations at 4K.

By patterning a strip of quantum dots adjacent to the MOSFET, we can determine the conductance of the dots. Our measurement consists of applying a voltage

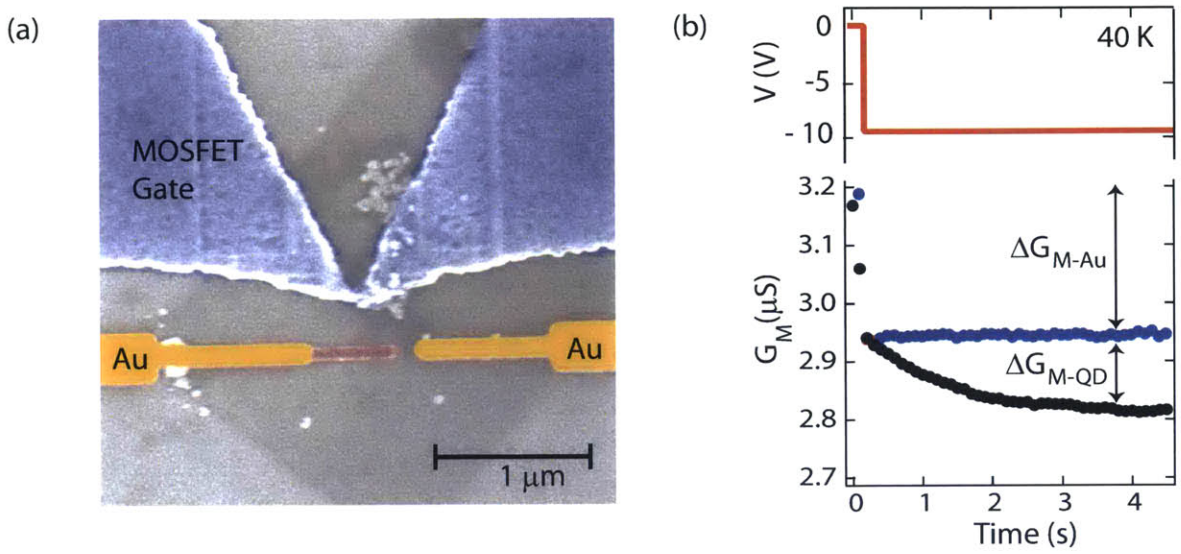

Figure 4-2: (a) False colored scanning electron micrograph of butylamine capped PbS nanopattern (red), adjacent to a narrow channel MOSFET gate (blue). The nanopattern is connected to one of the gold electrodes, but is 100 nm away from the other one. This geometry helps us to distinguish the response of the MOSFET to charge being added to the nanopattern and the gold electrodes. (b) Measurement technique (T = 40 K). The upper panel shows the voltage pulse applied to the gold electrodes as a function of time. The lower panel shows the response of the MOSFET, G_M, on pulsing the electrode connected to the nanopattern (black) and the the response on pulsing the electrode disconnected from the nanopattern (blue), at T = 40 K. The observation confirms a transient response caused by slow charging of the resistive nanopattern.

pulse to one of the gold electrodes connected to the nanopattern, and simultaneously monitoring the conductance of the MOSFET. For pulsing measurements, we use a high speed NI 6110 voltage card. We connect two Yokogawa voltage sources in series, and combine this with the output of the high speed card voltage card in order to apply a small pulse to a large DC offset. The other end of the nanopattern, is held at the same potential as the back gate for charge sensing measurements, and connected to an Ithaco Current amplifier, for current measurements.

When the MOSFET is in inversion, the nanopattern as well as the gold electrodes are capacitively coupled to the inversion region. As the voltage on the gold electrodes adjacent to the nanopattern is stepped from 0 to a negative voltage, we expect to see a response from charge being added to the gold electrodes and to the nanopattern. In order to distinguish the responses, we fabricated a device where the nanopattern is

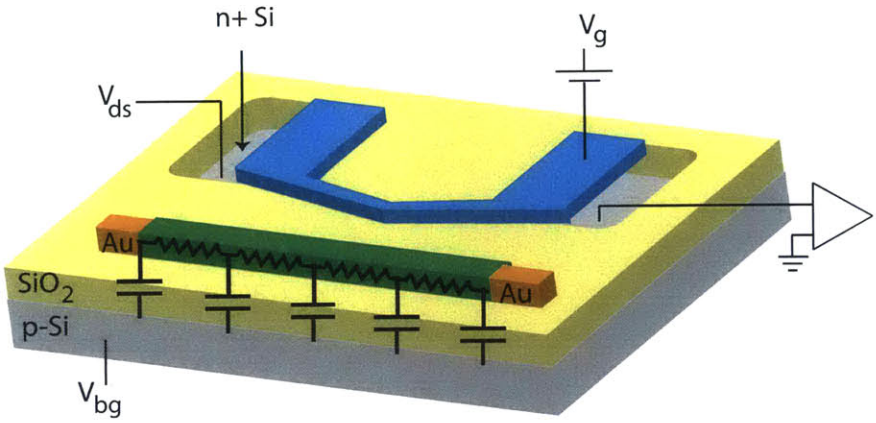

Figure 4-3: Device and circuit used for charge sensing measurements. The resistive material, is modeled as a distributed RC network. A key assumption for the formalism, is a uniformly distributed resistance over the length scale.

connected to only one of the gold electrodes. This was accomplished by terminating the pattern 100 nm away from one of the gold electrodes, lithographically. Figure 4-2 (a) shows a false color SEM image of the MOSFET adjacent to this nanopattern.

The pulse and the response of the MOSFET are shown in Figure 4-2(b). As we apply a negative voltage step to the gold electrode connected to the nanopattern, we observe an instantaneous jump in the MOSFET conductance followed by a further decrease slowly with time. We call this slow decay a charge transient. When we pulse the disconnected gold electrode, we observe only the instantaneous response. The MOSFET responds to charge being added to both the nanopattern and the gold electrodes. The response from the gold is instantaneous on our measurement time scale, because of the very low resistance of the metal, but the response from the highly resistive nanopattern is slower. We are essentially charging the capacitance between the gold electrodes and the nanopattern and the underlying substrate. The time dependence of the charging transient from the nanopattern has been shown to be accurately exponential [62], and the resistance of the nanopattern can be extracted from this transient, as discussed in the next section.

4.2.1 Diffusion Model

A quantitative model for extracting the resistance from charge transients was provided by K. MacLean [62], and we reproduce parts of it here. We model the resistive material as a distributed RC network as shown in Figure 4-3, where C is the capacitance per unit area of the strip. In doing so, we assume the material to be uniform such that the resistance per unit length $dR = R_s dx/w$ where w is the width of the strip, and R_s is the resistance per square.

If $\sigma(x,t)$ is the charge per unit area as a function of position along the strip x and time t, we obtain a diffusion equation:

$$\frac{\partial \sigma(x,t)}{\partial t} = D\frac{\partial^2 \sigma(x,t)}{\partial x^2} \tag{4.1}$$

where the diffusion constant is given by $D^{-1}=R_sC$. The diffusion equation can be solved by a separation of variables, and for a strip of length L, the solution can be approximated as:

$$\Delta\sigma(t) \propto e^{-D\pi^2 t/L^2} \tag{4.2}$$

To lowest order, the conductance of the MOSFET (G_M) varies linearly with $\Delta\sigma$, and we can write:

$$G_M(t) \approx G_\infty + G_o e^{-\Gamma t}, \Gamma = D\Pi^2/L^2 \tag{4.3}$$

We see that the expected functional form for the transient is exponential. From exponential fits to our transients, we can extract Γ and calculate the conductance of the nanopattern G_{PbS} as follows:

$$G_{PbS} = wLC\Gamma/\pi^2 \tag{4.4}$$

It is important to note here that the technique measures the differential conductance dI/dV, rather than just the conductance G of the material. For ohmic regimes they are identical, however they may be significantly different for non-ohmic regimes. The above derivation still holds true if G is replaced by dI/dV as long as the material

is uniform.

4.2.2 Limits of measurement technique

Just like all the other measurement techniques discussed in section 4.1, the charge sensing technique also has limitations in terms of the range of resistances that can be measured at a given temperature. With charge sensing, we effectively measure an RC time constant. For the feature sizes we are interested in, the effective capacitance is roughly of the order of 10^{-18} F. With this small capacitance, we can easily probe resistances as high as 10^{18} Ω, but for lower resistances, say R< 10^{13} Ω, we need to measure time scales faster than a μs, which becomes increasingly difficult due to instrument limitations. However for resistances less than $10^{13}\Omega$, we can measure the current using a current amplifier. The charge sensing technique is complementary to conventional current measurements in terms of the range of resistances that can be probed. While we may be unable to measure transients for the low resistance regime, we can use our charge sensor to study fluctuations in the nearby nanopattern, and we discuss more about this in section 4.6.

As we cool down to 4 K, and apply a voltage pulse to the gold electrodes, instead of seeing a transient from the nanopattern, we see a large jump in the MOSFET conductance which gradually dies away as time progresses, or a recovery, as shown in Figure 4-4 (a). This recovery is seen from pulsing the gold electrodes connected to the nanopattern as well as the disconnected electrode, and is therefore, not related to the nanopattern. This response has been understood in terms of screening from the p-type substrate [61]. As we apply a voltage to the gold contact, an opposing charge is induced in the p-type substrate, and at low temperatures where the resistance of the substrate is high, this charge is induced at a measurably slow rate r. To obtain a value for r, we fit the recovery to an exponential, and at 4 K we get a rate of 2 Hz. This rate is expected to be proportional to the resistance of the p-type substrate, and so as we increase the temperature this rate gets faster. Figure 4-4(b) shows the the screening rate as function of inverse temperature, and we see that the rate saturates to a minimum value at 4 K. In Figure 4-4(c), we plot Δr = r - r_{4K} as function of

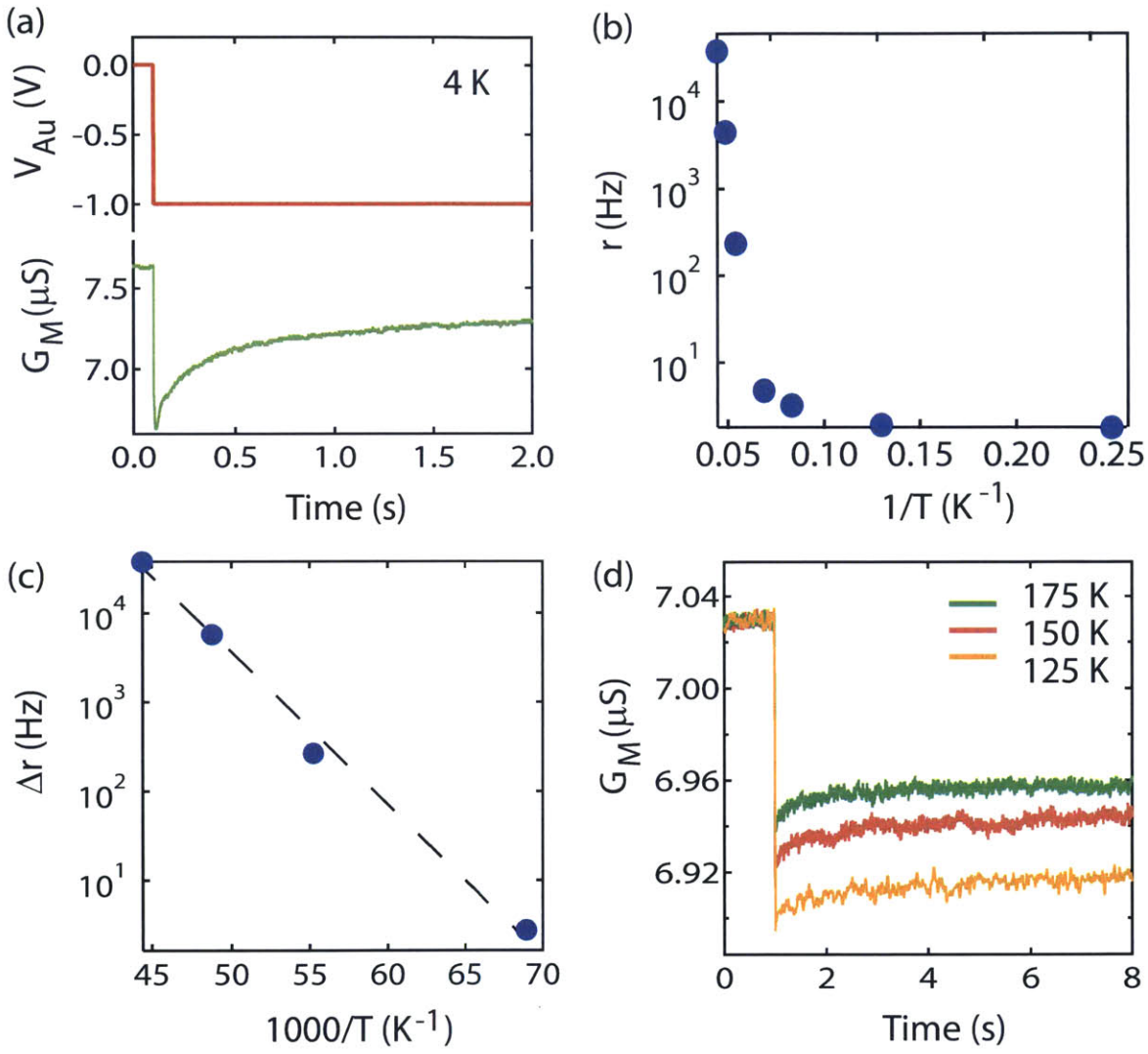

Figure 4-4: Screening and limits of measurement (a) The top trace (red line) shows the voltage step applied to the gold contact at T = 4 K. The lower trace shows the slow recovery of the MOSFET conductance, as discussed in the main text. (b) Screening rate, r, extracted from exponential fit to the recovery, as a function of inverse temperature for low temperatures. (c) Change in screening rate $\Delta r = r - r_{min}$ as a function of inverse temperature. The solid line is a theoretical fit described in the main text. (d) Screening from other sources at higher temperatures give slower recovery at high temperatures.

inverse temperature, and extract an activation energy of 45 meV, which is exactly the Boron acceptor binding energy, demonstrating that screening from the substrate limits the charge sensing measurements at low enough temperatures. Presumably the saturation results from some conduction mechanism other than activation of holes in the p-type substrate, such as the tunneling of electrons between acceptor states in the p-type substrate. K. MacLean et. al.[61] performed similar measurements and extracted the same activation energy, however the minimum saturation rate was four times higher than ours. This is reasonable given that the doping level of our p-type substrate is lower.

As the temperature is increased above 20 K, the recovery becomes too fast to measure, and we are able to see the transient response from the nanopattern again. The screening effects from the substrate restrict our transient measurements to temperatures above 20 K. At temperatures above 100 K, we again see a very slow recovery which may distort our transients. We believe that this may be caused by screening from charges in the oxide or the surface. The amount of distortion caused by this response, which may have a large sample to sample variation, poses another limit on the highest resistance that can be measured at these temperatures.

Finally, from the model discussed in the previous section, the oxide is assumed to be a perfect capacitor with no leakage. The resistance of the oxide then sets another limit on our measurement technique. In his Ph. D. thesis, K. MacLean [60] showed that in order for the leakage through the oxide to be negligible, the dielectric relaxation time of the oxide, defined as $\tau_{ox} = 1/\rho_{ox}\kappa_{ox}\epsilon_0$, must be larger than the charging time.

4.3 Transport in butylamine capped PbS quantum dot array

We present results for transport in nanopatterned arrays of butylamine-capped PbS quantum dots. The dot diameter estimated from optical absorption measurements

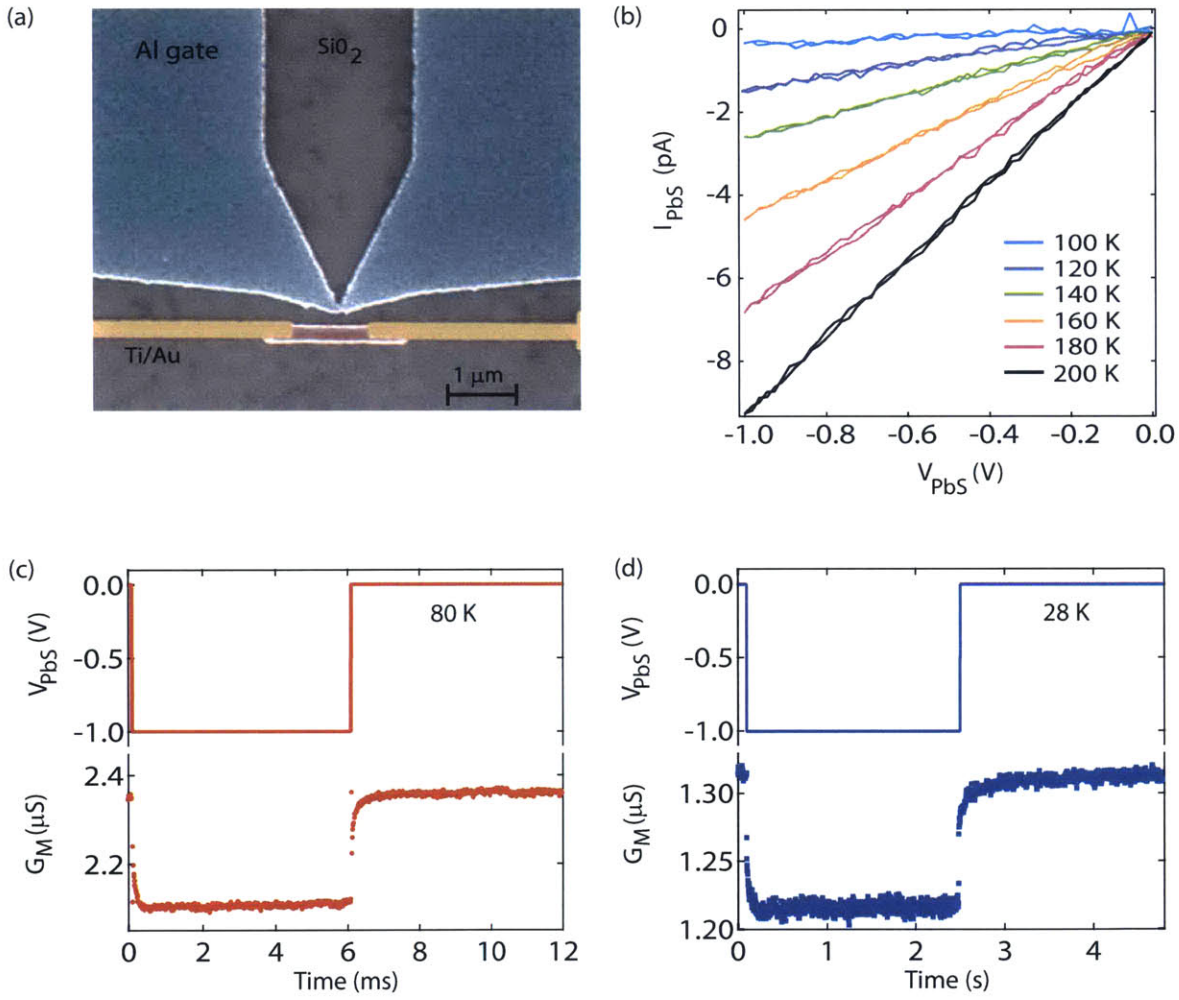

Figure 4-5: (a) False color scanning electron micrograph of a 200 nm wide nanopattern of butylamine capped PbS dots (red), connected to gold electrodes placed a micron apart. The nanopattern and the gold electrodes are defined with electron beam lithography and placed 100 nm away from the narrowest part of the Al gate of the MOSFET. (b) Current-voltage characteristics of the nanopattern from room temperature to 100 K. (c) Conductance of the MOSFET, G_M, as a function of time as the voltage on one of the gold electrodes is stepped from 0 to -1 and back to 0 at 80 K, and (d) 28 K.

ranges from 4.3 to 4.6 nm. The butylamine ligand attached to the dot surface using a solution ligand exchange discussed in Chapter 2, provides a 0.5 nm wide tunnel barrier. From noise measurements, we have learned that 80 nm wide nanopatterns have very few conduction channels and can therefore exhibit a large variation in the conductance. We, therefore, use 200 nm wide patterns to obtain measurements of average transport properties. Figure 4-5(a) shows a false color scanning electron micrograph of the measured device. A 200 nm wide nanopattern of butylamine capped dots, false colored in red, is placed between two gold electrodes spaced a micron apart, and approximately 100 nanometers away from the MOSFET gate (blue), using electron beam lithography. We create the nanopattern of dots using the procedure outlined in Chapter 2, with a 100 nm thick resist layer. The alignment procedure is discussed in detail in Appendix B.

As mentioned earlier, our device structure allows us to measure current in addition to transients resulting from the spreading of charge. At high temperatures, we are able to measure the current and extract the conductance of the array, G_{PbS}, directly. Figure 4-5(b) shows the current-voltage characteristics from room temperature to 100 K. As we move to lower temperatures, specifically below 100 K for this device, our current measurements are limited by instrument noise from the amplifiers. At these temperatures, we extract the conductance from exponential fits to charge transients as discussed below.

For transient measurements, we measure the conductance of the inversion region, G_M, with a 4 mV DC bias applied to one of the n-type contacts, and apply a fixed positive gate voltage, V_g, on the MOSFET gate. Because the conductance of the inversion region depends on the temperature, we adjust the MOSFET gate voltage as we vary the temperature so that G_M remains approximately constant. We then step the voltage on one of the gold electrodes from 0 to -1V, while the other electrode is held at the same potential as the p-type substrate. As charge diffuses in the distributed RC network of the array, the conductance of the MOSFET varies exponentially with time. We fit the transient response to $G_M = G_0 \exp(-\Gamma t)$ where $\Gamma = \pi^2 g_{PbS}/wLC$, and extract the conductance of the array, G_{PbS} at a bias of 0.5 V.

The upper panels in Figure 4-5(c) and (d), show the time dependence of the applied voltage pulses. The lower panels show the transient responses of the MOSFET conductance, G_M, at 80 K and 28 K, respectively. In order to improve the signal to noise, we average multiple traces together. The traces shown here are the average of 25 transients at 28 K and 100 transients at 80 K. We see that the transient at 80 K, which happens on the millisecond time scale, is much faster than the transient at 28 K, which occurs at a timescale of few seconds, corresponding to a higher conductance at 80 K. The lowest temperature at which we could observe transients for this device was 22 K. At lower temperatures, even though the timescales would be within the measurement capabilities of our technique, we were limited by screening effects from the substrate, as discussed in the previous section.

Figure 4-6(a) and (b) show the measured conductance of the nanopatterned array, G_{PbS} at a bias of 0.5 V, from room temperature to 22 K, plotted as a function of inverse temperature and $1/T^{1/4}$ respectively. At this low bias, the differential conductance is expected to be the same as the ohmic conductance. Filled circles represent conductances extracted from the current-voltage characteristics, and empty circles represent the conductances from transient measurements. A linear relationship of the log of the conductance as a function of inverse temperature suggests that the transport follows a nearest neighbor hopping mechanism for that temperature range. From Figure 4-6(a), we see that the conductance deviates from a simple linear relationship at temperatures below $\sim$ 50K. We would not have observed this deviation near zero bias, without our charge-sensing measurements.

The temperature dependence can be well-described by the sum of two simply activated processes, as seen in Figure 4-6(a). We extract two activation energies of 55 meV and 13 meV at high and low temperatures respectively. A lower activation energy at lower temperatures is expected when the conduction mechanism changes from nearest neighbor to variable range hopping. The black dashed line in Figure 4-6(b) shows a fit to Mott's variable range hopping, $G = G_0 \exp(-T^*/T)^{1/4}$, with $T^* = 1.2 \times 10^7$ K. It is difficult for us to make any strong claims about the transport mechanism simply from the temperature dependence. It is possible that there are two conduction

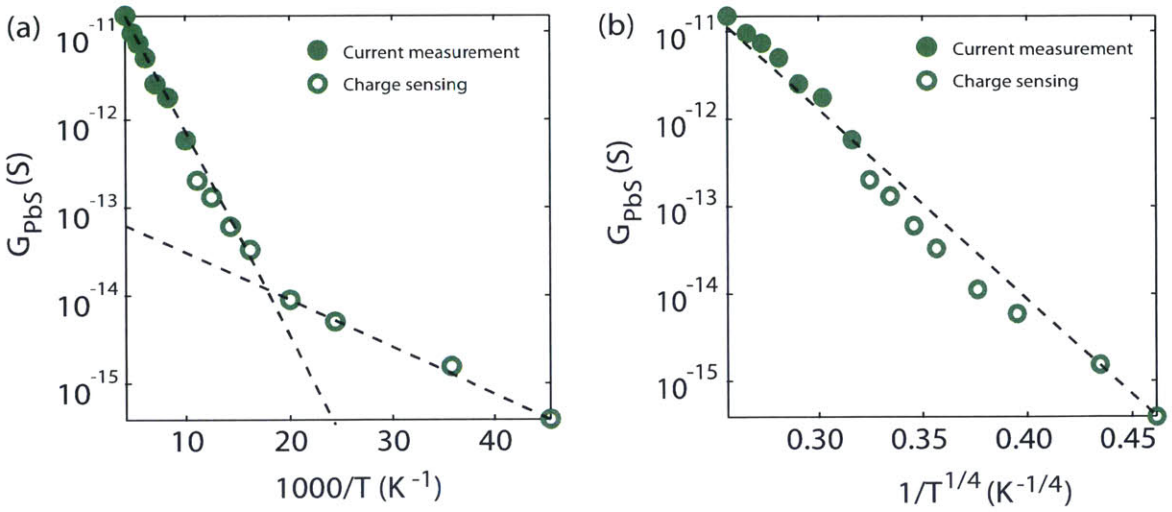

Figure 4-6: (a)Conductance of the butylamine capped PbS dot array, G_{PbS}, as a function of temperature, obtained from charge sensing (open circles) and current measurements (filled circles), measured at a source drain bias of 0.5 V. The black dashed lines are theoretical fits to simply activated transport with two activation energies as described in the main text. (b) Conductance, G_{PbS}, plotted as a function of $1/T^{1/4}$. Black dashed line is a fit to Mott's variable range hopping.

channels in parallel, which give rise to two different activation energies in the system. For variable range hopping, we expect that at some higher temperature there should be a crossover from variable range to nearest neighbor hopping. This transition is expected when the hopping distance becomes equal to the nearest neighbor separation in the array. In order to estimate the hopping distances, we need to calculate the localization length, and to this end we study the electric field or bias dependence of the conductance.

4.3.1 Electric field dependence

As discussed in the previous section, we measure a differential conductance using our charge sensor. For low bias voltages, or low electric fields, this is identical to the conductance, G. However, transport through colloidal dot arrays can be non-ohmic, especially at high fields, and we now distinguish the differential conductance, g_{PbS} = dI/dV at fixed voltage from the ohmic conductance, G_{PbS}. To measure the field dependence of the differential conductance, we apply a negative voltage to one of the

gold electrodes, while the other is held at the same potential as the p-type substrate. Then we rapidly step the voltage on the former electrode by an additional -0.5 V and obtain the conductance from the observed charge transient, as previously discussed. For example, to measure the differential conductance, g_{PbS}, at an applied bias voltage of V_{PbS} = -3.25 V, we apply a fixed voltage V_{PbS} = -3 V to one electrode, and rapidly step the voltage to V_{PbS} = -3.5 V. We have reduced the size of our voltage pulse in order to more finely sample a given voltage range. At high temperatures and high fields, we extract the differential conductance by differentiating the current as a function of source-drain bias.

We study the field dependence at negative source-drain bias here, because of minor MOSFET design constraints. For our MOSFET, we apply a positive gate voltage on the MOSFET gate to form an inversion region underneath, and for positive bias voltages on the gold electrodes, an inversion region will form underneath the gold as well. Because the gold electrodes are placed very close to the narrowest portion of the MOSFET gate, for large positive bias on the gold electrodes, the inversion layers underneath the two metals may connect resulting in a decreased sensitivity. It is possible to measure transients at positive source drain biases, by adjusting the separation between the MOSFET gate and the nanopattern such that the inversion layers don't connect, and this is discussed further in section 4.4. In general, apart from small non-uniform gating effects at large bias voltages, we do not expect a difference in the transport mechanisms at positive and negative bias voltages.

Figure 4-7(a) shows the differential conductance as a function of applied field across the dot array, for different temperatures. The solid symbols are data obtained from current measurements, and open symbols are from charge sensing measurements. We find that the differential conductance increases exponentially with applied field for low fields at all temperatures. However, at lower temperatures, we observe a rollover of the differential conductance beyond a certain field strength. Figure 4-7(b) shows the temperature dependence of the differential conductance for different fields.

We first consider the electric field dependence of variable range hopping. For large electric fields, E, such that $E > 2k_BT/ea$, where a is the localization length,

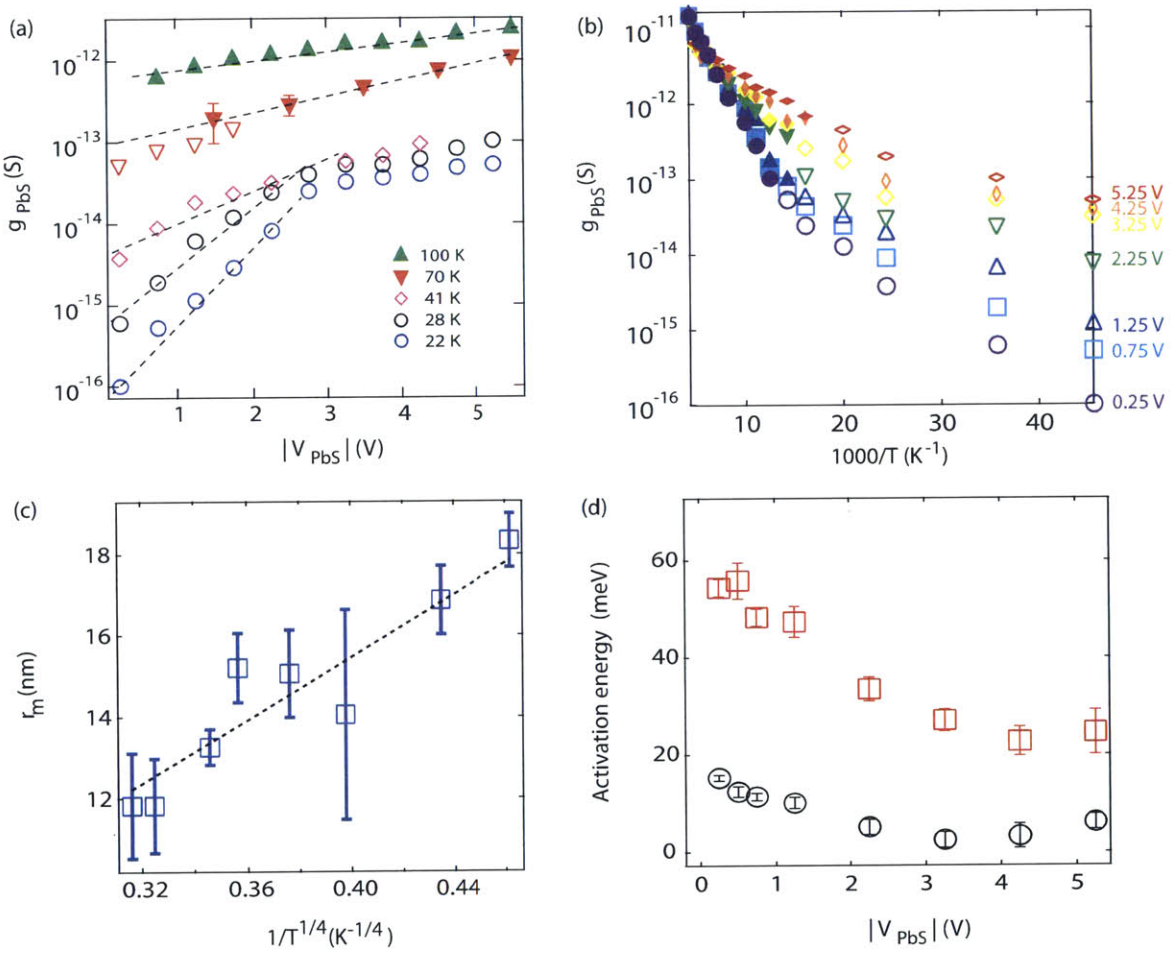

Figure 4-7: (a) Differential conductance, g_{PbS}, of butylamine-capped PbS dots as a function of applied field across the dots, for different temperatures (b) Temperature dependence of the differential conductance of butylamine capped PbS dots for different fields (c) Variable range hopping distances, r_m, extracted from exponential fits to the field dependence of the differential conductance, dI/dV, where the current, I, is described by equation 4.5. (d) Activation energies extracted by fitting the conductance to a sum of two simply activated processes.

the electron can move by downward hops only, emitting a phonon at each hop. The conductance is then temperature independent and only depends on the field as, G $\propto$ $\exp(E^*/E)^{1/4}$. However, not a lot of work has been done to understand the dependence in the moderate or low electric field regime, E < $2k_BT/ea$. The most significant experimental results on the field dependence of the conductance are from Elliot et al [26] on amorphous germanium, because it is the amorphous semiconductor that clearly exhibits variable range hopping. They find an exponential dependence of the conductance on the electric field, which has since been supported by theory from Pollak and Reiss [88].

Within the percolation model proposed by Pollak and Reiss [88], the field is expected to change the percolation path in such a way that the critical impedance is lowered, leading to an exponential increase in the conductance with field. The current in the low field regime is then given by:

$$I \sim exp - \left(\frac{T^*}{T}\right)^{1/4} exp\left(\frac{3}{16}\frac{eEr_m}{k_BT}\right) \tag{4.5}$$

where, r_m, is the variable range hopping distance. We note that the length scale in the exponential (3/16 r_m) is a fraction of the hopping distance, and requires a little clarification. The small length scale can be understood if for low fields, only a fraction of the bonds in the percolation path are affected by the field. The existing field effect can then be thought of as an alteration of the percolation path itself rather than a modification of the critical links.

We extract the hopping distance, r_m, from exponential fits to the conductance measured as a function of field, as given by equation 4.5. At 22K, we get a hopping distance of approximately 20 nm. Given an inter-dot spacing of approximately 5 nm, this would be hopping across 4 dots. In Mott's picture of variable range hopping, the hopping distance, r_m, is weakly temperature dependent, and is given by:

$$r_h = \frac{3}{8}a\left(\frac{T^{*\,1/4}}{T}\right) \tag{4.6}$$

where a is the localization length. Figure 4-7(c) shows the hopping distance as a function of $1/T^{1/4}$, and we find that it fits well to a straight line. As the temperature increases, the hopping distance decreases as $T^{1/4}$. We extract a localization length, as given by equation 4.6, of 1.75 nm, which seems reasonable.

At low temperatures, as we move to higher fields, we will start a transition out of the low field regime for hopping conduction. The flattening of the conductance at low temperatures and high fields likely represents the onset of the expected high field $E^{1/4}$ behavior. At 22 K and 40 K, the quantity $eEa/2k_BT$ starts to become comparable to 1, at field strengths of 2 V/m and 3 V/m respectively, which matches the field at which we start to observe the flattening of the curves reasonably well.

4.3.2 Gate voltage dependence

By changing the voltage difference between the nanopattern and the underlying silicon substrate, the substrate can serve as a back gate, and one can measure the conductance as a function of gate voltage. We apply the same voltage V_{PbS} to both the gold electrodes relative to the p-type substrate, and then pulse the voltage. We do not observe a measurable change in conductance from charge sensing measurements for gate voltages up to 7 V.

We are, however, able to observe a weak gate voltage dependence in current measurements. Figure 4-8(a) shows the current-voltage characteristics for different gate voltages at 100 K. The first observation is that as we apply a more negative voltage in the back gate, the current increases, which means that the dots have holes as majority carriers. This is similar to observations on wider arrays of PbSe dots [70]. The current, and roughly the differential conductance as well, changes by only a factor of 2 by changing the gate voltage from 0 to -10 V.

Figure 4-8(b) shows the current as a function of gate voltage and temperature for a source drain bias of 5V. From this data, we can extract a field-effect hole mobility, μ_{lin}, in the regime where current varies linearly with the gate voltage, according to

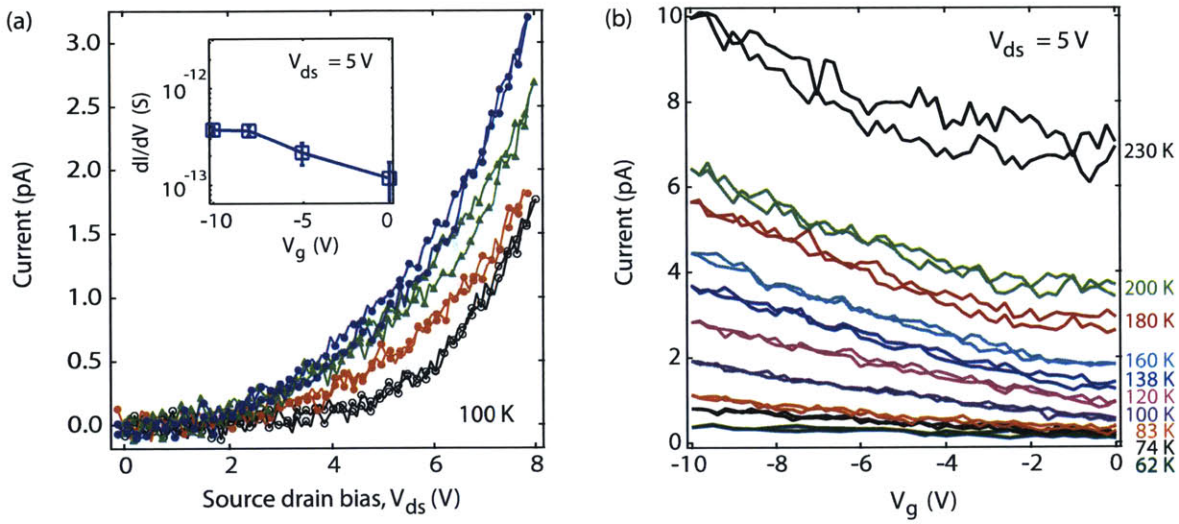

Figure 4-8: Gate voltage dependence for butylamine capped PbS dots (a) Current-voltage characteristics for different gate voltages at 100 K. V_g = 0V for black circles, V_g = -5 V for filled orange circles, V_g = -7 V for green triangles and V_g = -10 V for filled blue circles. Inset shows the differential conductance at around 5 V source drain bias as a function of gate voltage at 100 K. (b) Current as a function of gate voltage and temperature at source drain bias of 5V.

the gradual channel approximation:

$$\left.\frac{\partial I}{\partial V_g}\right|_{V_{ds}=constant} = \frac{wC_{ox}V_{ds}}{L}\mu_{lin} \tag{4.7}$$

where w and L are the width and length of the nanopattern, and C_{ox} is the capacitance per unit area of the gate oxide. We find that the slope of the curves increases with increasing temperature, thereby implying a field effect mobility that increases with temperature. An increase in mobility with temperature is not uncommon for disordered systems [58]. In general, for disordered systems, the field effect mobility should increase with the density of gate-induced carriers At higher temperatures the measurements become dominated by leakage through the gate oxide, and it becomes difficult to see a gate voltage dependence. At 200 K, the field effect mobility at 5V source-drain bias is estimated to be of the order of 10^{-5} cm^2/Vs. The field-effect mobility is a 'filled trap' mobility that depends on device geometry and biasing conditions and is not an intrinsic property of a QD film. So, this value of mobility should be considered as a lower limit rather than an absolute number.

4.4 Transport in Oleic acid capped PbS quantum dot arrays

As discussed in the previous chapter, we have been able to measure current in nanopatterned arrays of oleic acid (OA) capped PbS dots. To our knowledge, these are the first successful transport measurements on unannealed dot arrays with the native ligand. Although the change in the height of the tunnel barrier is difficult to estimate, the inter-dot separation changes from 0.5 nm in butylamine-capped dots to 1 nm in oleic-acid-capped dots, from TEM measurements. The native oleate ligands also form ordered superlattices over relatively large length scales, as discussed in Chapter 2.

Before we discuss the data collected from charge sensing measurements, we briefly focus on the current-voltage characteristics. Figure 4-9(a) shows current-voltage characteristics from room temperature to 60 K for positive source-drain bias voltages. As we go to lower temperatures, the characteristics become highly non symmetric between positive and negative bias voltages, as shown in figure 4-9(b). We are always able to measure a current with a positive source-drain bias, but not with a negative source-drain bias. The inset shows current as a function of applied gate voltage for fixed temperature and source-drain bias. We observe that the current increases as the gate voltage is made more negative, consistent with holes being the majority carriers. If we think about non-uniformly gating the nanopattern with a source-drain bias, a negative source-drain bias is equivalent to a positive voltage on the back gate, thereby depleting the dots for a hole doped array. For a low enough carrier density, even a small effective positive voltage on the back gate may be enough to completely deplete the dots at lower temperatures. As the temperature is increased thermal excitation of the carriers will serve to make the current-voltage characteristics more symmetric. Because of these gate effects, to study transport in oleic acid capped dots with our charge sensor, we only probe the positive source drain bias regime.

For extracting the differential conductance, g_{PbS-OA} at fixed bias voltage V_{ds}, from charge transients, we set the source-drain voltage to a desired fixed value and

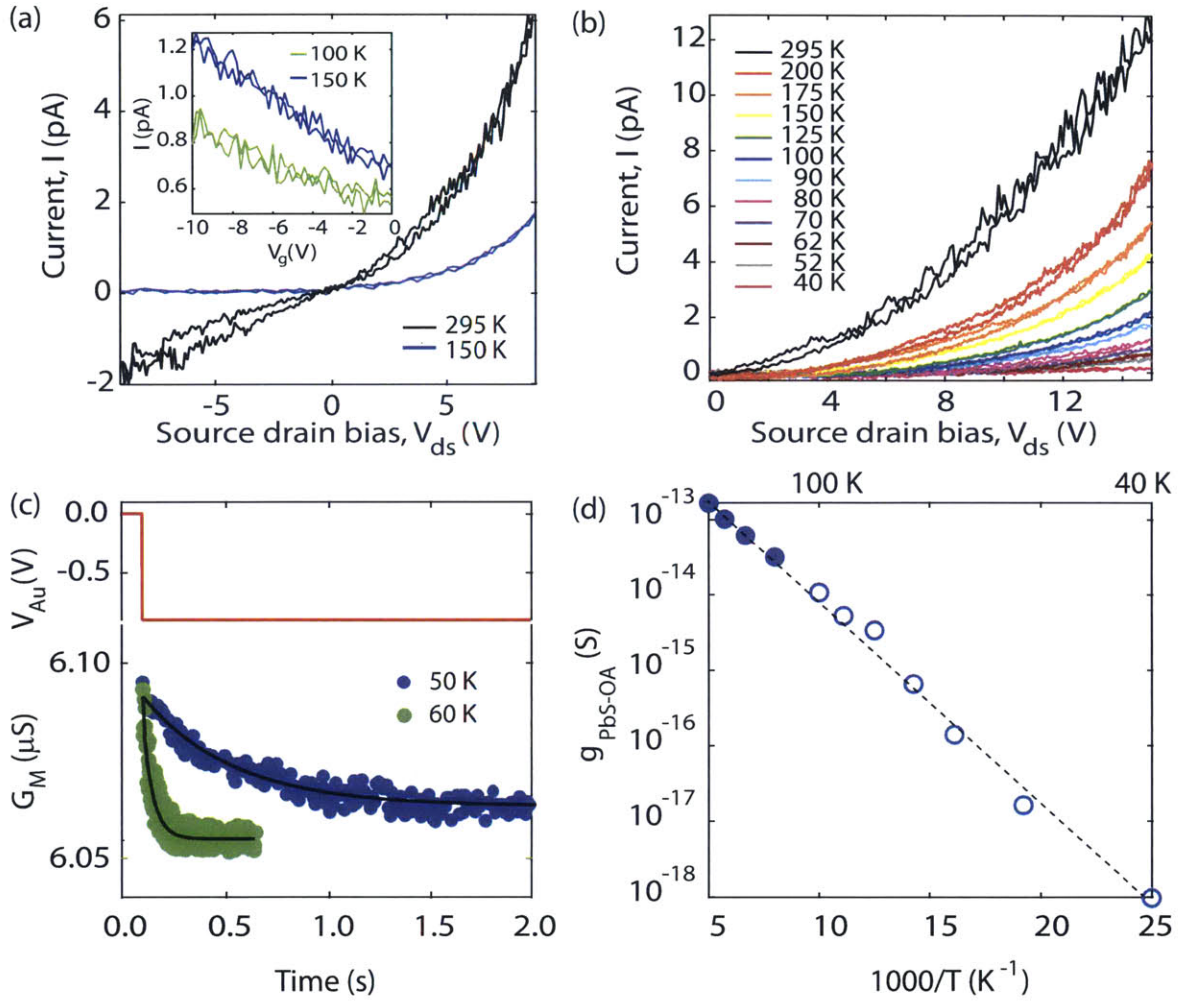

Figure 4-9: Transport in oleic acid capped PbS dots (a) Asymmetry in current-voltage characteristics between positive and negative source-drain bias at lower temperatures. Inset shows the gate voltage dependence at 170 K, the current increases as a negative gate voltage is applied consistent with holes being the majority carriers. (b) Current-voltage characteristics as a function of temperature for positive source-drain bias. (c) The voltage on one of the gold electrodes connected to the nanopatterned array is stepped from 0 to -1. As charge diffuses in the distributed RC network of the array, the conductance of the MOSFET varies exponentially with time. Solid markers show the MOSFET conductance in response to the voltage pulse at 50 and 60K, for a source drain bias of 3.5 V. Solid black lines are fits to $G = G_0\exp(-\Gamma t)$ where $\Gamma = \pi^2 g_{PbS-OA}/wLC$ and g_{PbS-OA} is the differential conductance per square of the nanopatterned oleic acid capped PbS array at 3.5 V. (d) g_{PbS-OA} at $V_{ds} = 3.5$ V, as a function of inverse temperature. Open circles represent differential conductance extracted from charge sensing measurements and filled circles are the data extracted from measuring the current.

then apply a voltage step from 0 to -1 V. As charge diffuses in the distributed RC network of the array, the conductance of the MOSFET varies exponentially with time. Figure 4-9(c) shows the transient response of the MOSFET conductance to the applied voltage pulse. The solid black lines are fits to $G = G_0\exp(-\Gamma t)$ where $\Gamma = \pi^2 g_{PbS-OA}/wLC$. The lowest temperature and source-drain bias we could measure are 3.5 V at 40 K. We find the resistance to be $10^{18}\Omega$. This is the highest resistance ever measured in nanopatterned quantum dot arrays, to our knowledge.

Figure 4-9(d) shows the differential conductance at 3.5 V for oleic acid capped PbS arrays, as a function of inverse temperature. We extract the differential conductance from charge transients at each temperature in the range of 40-100 K (open markers). At temperatures above 100 K, we obtain the differential conductance from derivatives of the current-voltage characteristics. We find that in the temperature range of 40-200 K, the differential conductance fits very nicely to a simply activated form, with an activation energy of 59 $\pm$ 4 meV. We were unable to measure the conductance near zero bias at low temperatures even using our charge sensing measurements due to the very high resistance of the array, and limitations from dielectric relaxation of the underlying oxide.

As discussed in section 4.3.1, we probe the finite bias regime by applying a static field across the nanopattern. Then we rapidly step the voltage on one of the electrodes by an additional -1 V and obtain the differential conductance from the observed charge transient. More specifically for this data set, to measure the differential conductance, g_{PbS-OA} at an applied bias voltage of V_{PbS} = 3.5 V, we apply a fixed voltage V_{PbS} = 4 V to one electrode, rapidly step the voltage to V_{PbS} = 3 V and measure the resulting charge transient.

Figure 4-10(a) shows the measured differential conductance as a function of inverse temperature for different values of electric field or bias voltage across the dot array. As before, the filled markers represent differential conductance extracted from the current-voltage characteristics, and the empty markers represent the differential conductance extracted from charge sensing measurements. Black dashed lines are fits to $G_{PbS-OA} = G_0\exp(-E_a/k_BT)$, where E_a is the activation energy. Because these

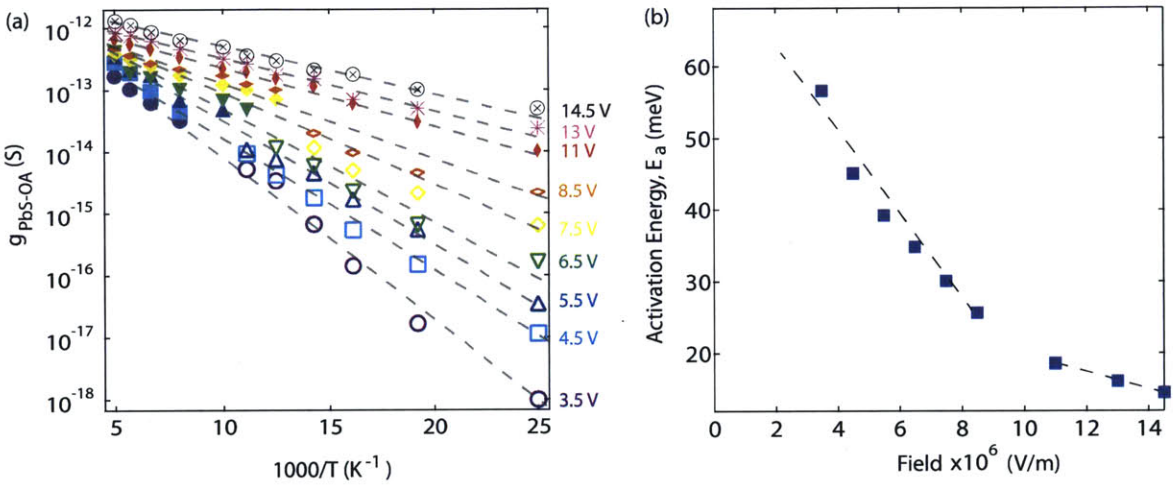

Figure 4-10: (a) Differential conductance of oleic acid capped PbS dots, g_{PbS-OA}, as a function of inverse temperature, for different values of electric field or bias voltages across the dot array. Filled markers represent differential conductances extracted from the current-voltage characteristics, and empty markers represent the differential conductances extracted from charge sensing measurements. Black dashed lines are fits to $g_{PbS-OA} \sim \exp(-E_a/k_BT)$, where E_a is the activation energy. (b) Activation energy, E_a, as a function of the applied electric field. Blue markers indicate the data points and the black dashed lines represent straight line fits to the data. We extrapolate the straight line fit at low fields to zero bias, in order to estimate the activation energy near zero bias.

measurements are performed at positive source-drain bias, when the voltage on the gold electrodes becomes more positive than the MOSFET gate voltage, it introduces a small error in the differential conductance measurements. It is likely that the error lies in estimating the capacitance, but the origin of this effect is not clearly understood. Figure 4-10(b) shows the two slopes observed from the calculated activation energies as a function of the applied electric field. Blue markers indicate the data points and the black dashed lines represent straight line fits to the data. We extrapolate the straight line fit at low fields to zero bias, in order to estimate the activation energy near zero bias, which is approximately 70 meV.

4.5 Discussion

In this chapter we have attempted to study how transport in PbS dots depends on the tunnel barrier between the dots. Our measurements here constitute the highest resistances measured for colloidal quantum dot systems. Colloidal quantum dot arrays are similar to amorphous and doped semiconductors, in the sense that they have localized electronic states, and charge transport is expected to occur via phonon-assisted hopping between localized sites as long as the disorder in site energy is larger than the hopping matrix element between sites. As long as there is a finite density of localized sites near the Fermi energy, transport can occur via thermal activation from a localized state below the Fermi energy to a localized state above the Fermi energy. The probability of this hop is proportional to: the Boltzmann factor, $\exp(-\Delta/k_BT)$, where Δ is the disorder between site energies, a factor depending on the phonon occupation, ν_{ph}, and a factor depending on the wavefunction overlap. According to Mott [75], if the localization is very strong, the electron naturally jumps to the state nearest in space because the term $e^{-2\alpha R}$ falls rapidly with distance. This is the nearest neighbor or Miller-Abrahams hopping.

Charge transport in large scale arrays of annealed PbSe dots [70], has been explained using a simple model of nearest neighbor hopping. As holes are the majority carriers in our array, we assume that they move in the highest energy unoccupied

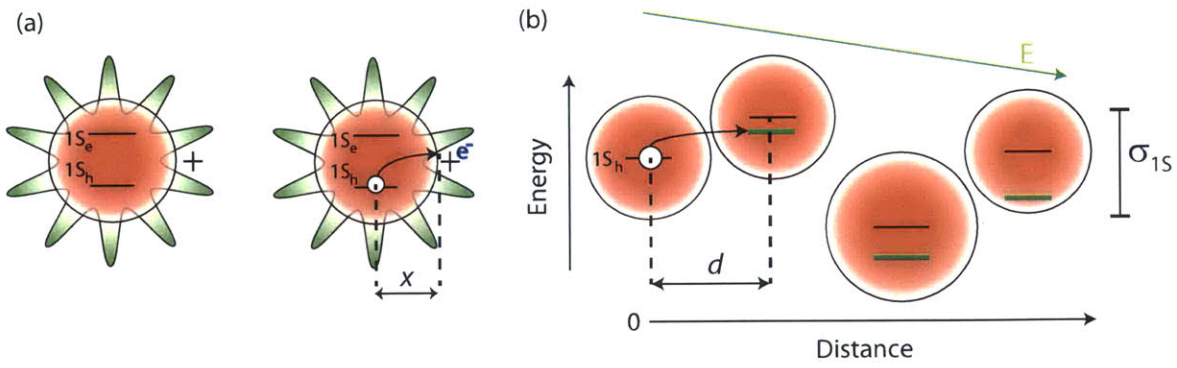

Figure 4-11: (a) and (b) illustrate the two components of the activation energy and the associated length scales. At high field, length scales for the low and high field conductance. 'd' is the inter-dot distance, and 'x' is the separation between the surface of the dot and an adjacent dot.

orbitals of the dots, which we label $1S_h$, and that disorder gives a distribution of these site energies. We also assume that the holes contributing to the dark conductance originate in acceptor states on the surface of some fraction of the dots. At low electric fields, a hole must then overcome two contributions to the activation energy in order to reach the other electrode. Firstly it must overcome the binding energy of the acceptor state, $E_F - E_{1S_h}$ and secondly it must overcome the disorder broadening of the $1S_h$ states,σ_{1S_h} . The activation energy is then given by:

$$E_a = E_F - E_{1S_h} + \sigma_{1S_h} \tag{4.8}$$

As the field strength is increased, the energy of the $1S_h$ states are lowered by the field, and at a critical field, E_c,the activation energy from disorder is completely overcome by the field ($eE_cd = \sigma_{1S_h}$) and only the activation energy for excitation from the acceptor state remains. This gives rise to two length scales in the problem. The activation energy from disorder is reduced by eEd, where d is the distance between neighboring dots, while the activation energy from the acceptor binding is reduced by eEx, where x is the distance from the acceptor state to the 1S state. This is expected to give rise to two slopes of the activation energy as a function of field.The

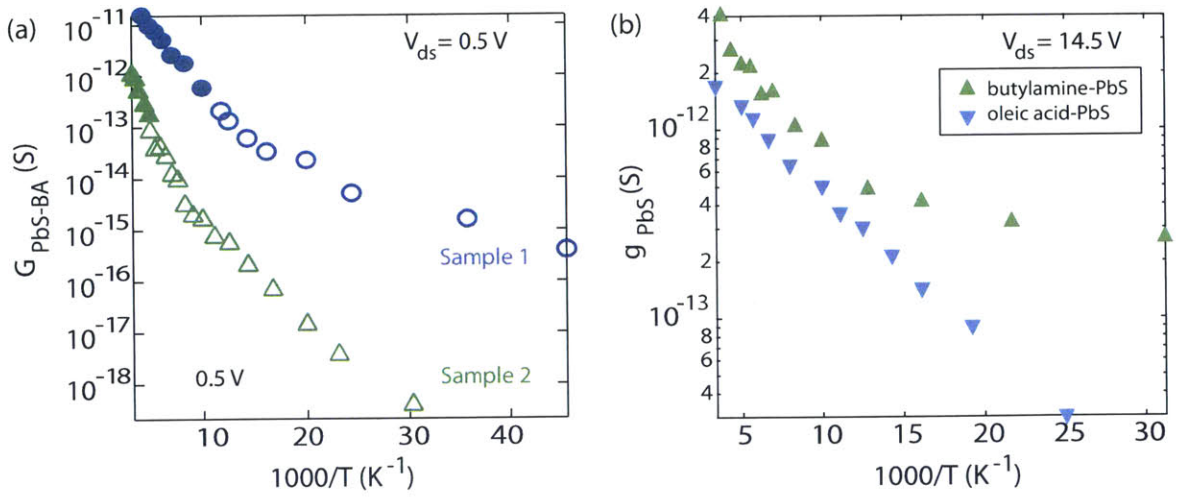

Figure 4-12: (a) Sample to sample variation. Conductance of nanopatterned butylamine capped PbS dots, G_{PbS-BA}, as a function of inverse temperature, for two nominally identical samples, at a source-drain bias of 0.5 V. As before, filled markers represent current measurements and empty markers represent transient measurements. (b) Differential conductance, g, at a bias of 14.5 V, measured from current measurements for butylamine capped nanopatterns (green markers), and oleic acid capped nanopatterns (blue markers), as a function of inverse temperature. We observe that while the resistance of these two samples is comparable at the given field, the temperature dependence is remarkable different.

conductance in the presence of a field may be written as:

$$G = G_0 exp - \left(E_a - \frac{eE(x+d)}{k_B T} \right) \tag{4.9}$$

These processes are illustrated by a cartoon in Figure 4-11.

Our results for oleic acid capped dots are consistent with the model discussed above. The conductance is simply activated, with an activation energy that decreases with field. At the highest fields (11-14 $\times 10^6$ V/m), the slope is given by -ex, from which we extract x = 0.8 $\pm$ 0.1 nm. At the highest fields, the length scale is is dominated by the excitation of an electron from the interior of the dot to an acceptor state on the surface, as illustrated in Figure 4-11. In the low field region, the slope gives us x+d = 6.2 $\pm$ 0.6 nm. Using x = 0.8 nm, we extract d = 5.4 nm $\pm$ 0.6 nm, which is within error of the expected inter-dot separation of approximately 5.5 nm, given the dot diameter between 4.3 and 4.6 nm and size of ligand, roughly 1 nm.

From optical absorption of measurements of the dots in solution, we extract roughly the disorder in site energies to be 100 meV from the full width at half maximum of the first absorption peak. The change in the slope at 10×10^7 V/m indicates that this is approximately the critical field. At this field the activation energy has been reduced by approximately 45 meV, roughly half the variation in energy measured optically, which seems reasonable. A crossover from Ohmic to non-Ohmic conduction is also expected when the field reduces the activation energy by an amount much smaller than k_BT, or more specifically E_a - eE(x + d) << k_BT. At room temperature, this is expected to happen around 5 V source-drain bias, which is consistent with our data shown in Figure 4-9(a). At lower temperatures (40 K), the ohmic region is expected only at bias voltages of less than 1 V. Nearest neighbor hopping therefore provides a self consistent explanation for transport in oleic acid capped PbS dots.

For butylamine-capped dots, we attempt to carry out a similar analysis. We fit the data shown in Figure 4-7(b) to a sum of two simply activated processes and extract both the activation energies. We plot the activation energies as a function of field, as shown in Figure 4-7(d). For two conducting channels in parallel, we would expect both the activation energies to decrease linearly with field. From the evolution of activation energies with field, at low fields we find length scales of 9 nm and 3.1 nm for the larger and smaller activation energy, respectively. The observation of a smaller length scale associated with a smaller energy is then difficult to understand from a picture of nearest neighbor hopping.

The data, however, fit well to Mott's variable range hopping, $G \sim \exp(-T^*/T)^{1/4}$, with $T^* = 1.2 \times 10^7$ K. We find an exponential dependence of the conductance on the electric field, as expected for the low field regime of variable range hopping, and this allows us to extract a localization length of 1.76 $\pm$ 0.2 nm. With this, we correctly predict the onset of the high field regime. Variable range hopping therefore seems to be a self consistent explanation for transport in butylamine capped dots.

As in the previous chapter for 80 nm wide films, we have shown here a significant sample to sample variation even with 200 nm wide patterns. Nonetheless, for all

samples studied, we are able to fit the data to Motts functional form. Figure 4-12(a) shows the conductance as a function of inverse temperature for two nominally identical nanopatterns of butylamine capped dots, at a source-drain bias of 0.5 V. As before, filled markers represent current measurements and empty markers represent transient measurements. Figure 4-12(b) shows a comparison of the most resistive butylamine pattern, and the most conducting oleic acid nanopatterns that we have measured, at a source-drain bias of 14.5 V. We observe that while the differential conductance of these two samples is comparable at the given field at room temperature, the temperature dependence is remarkably different.

The transition of the conduction mechanism from nearest neighbor hopping with oleic acid capped dots to variable range hopping for butylamine capped dots, may result from the change in the wavefunction overlap, or, equivalently, the localization length. The density of states at the Fermi energy, $D(E_F)$, for oleic acid may also be smaller, if the states arise from acceptors. The strong asymmetry in the IV curves, suggests that the hole density, and therefore the acceptor density, is smaller in the oleic-acid capped films. The smaller wavefunction overlap, owing to larger interdot separation, as well as lower density of states, favor nearest neighbor hopping. Increasing the interdot coupling by a ligand exchange, results in variable range hopping for the whole temperature range.

To conclude, we have studied transport in a colloidal quantum dot array as a function of inter-dot coupling. For a stronger interdot coupling, we observe variable range hopping conduction. As the overlap is decreased, we observe a transition to nearest neighbor hopping or simply activated transport for the whole temperature range. These measurements are made possible only by a combination of nanopatterning, and subsequent integration of a charge sensor to measure high resistances. In the next section, we look at charge detection or the study of fluctuations in these nanopatterned arrays using our integrated charge sensor.

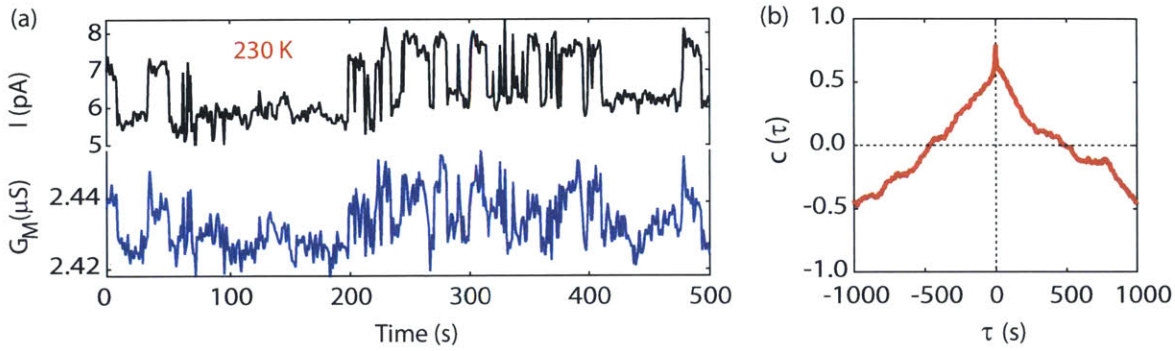

Figure 4-13: Noise correlations measured at 230 K (a)Current, I_{PbS-OA}, at a bias of 8V, as a function of time from oleic acid capped PbS dots, showing clear telegraph noise. (b) Correlation, $c(\tau)$ between the current, I_{PbS-OA} and G_M calculated from data such as that shown in (a), as discussed in the main text.

4.6 Sensing fluctuations with a charge sensor

In this chapter, we discussed how an integrated silicon based charge sensor can be used to study transport in highly resistive quantum dot arrays, by measuring RC time constants. Once the transients become too fast to be measured, our narrow channel MOSFET can then operate as a charge sensor capable of detecting fluctuations in the nearby material. As discussed in the previous chapter, we observe 1/f and telegraph noise from current measurements on nanopatterned PbS dots. The origin of the noise is believed to be conductance fluctuations, caused by the filamentary nature of conduction in the nanoscopic patterns. Discrete switching events were observed at temperatures just below room temperature, in the current through oleic acid capped dots.

At 230 K, where the resistance of the array is not too large, we apply a source-drain bias of 8 V between the two gold contacts and measure the current, I, that flows through the nanopattern. In the top panel of Figure 4-13(a), we plot the current, I, measured as a function of time with a bias of 8V. We measure the MOSFET conductance, G_M as a function of time simultaneously, and this is plotted in the bottom panel of Figure 4-13(a). We see that the two are correlated: When the current through the oleic acid capped PbS nanopattern jumps up, so does the MOSFET conductance, and vice versa. This correlation can be demonstrated explicitly in Figure

4-13(b). Here we measure the current, I, and the G_M simultaneously for a long period of time, and compute the correlation function:

$$c(\tau) = \frac{1}{T}\int_0^T \widetilde{I}_{PbS}(t+\tau)\widetilde{G_M}(t)dt \tag{4.10}$$

Here we define $\widetilde{G}_M$(t) and $\widetilde{I}_{PbS}$ by subtracting their mean values and dividing by their standard deviations. For two completely uncorrelated functions f(t) and g(t), c(τ) = 0. For two perfectly correlated quantities, c(τ) has a peak at $\tau = 0$, and c(0) is equal to either 1 or -1, depending on whether the functions are correlated or anti-correlated. We see that for our data c(τ) has a clear peak at $\tau = 0$ with a value 0.8, indicating a high degree of correlation between the two signals. The triangular background comes from the slowly varying square wave envelope in the two traces, as the correlation function of two square waves, is a triangular wave. From this, data it is clear that the MOSFET can detect conductance fluctuations in a nanopattern adjacent to it.

4.6.1 Dual MOSFET charge sensing

The conductance of a MOSFET channel can also be influenced by electron trapping and de-trapping events in the silicon dioxide nearby, thereby contributing noise to a charge detection measurement. For two distinct MOSFETs, each is subject to charge fluctuations inherent to the sensor but is insensitive to the fluctuations in the neighboring MOSFET as long as the neighboring MOSFET is sufficiently far away. As such, we expect the noise in the two MOSFETs to be uncorrelated. The signal in both MOSFETs arising from electron transport in the nanopattern is expected to be correlated while the noise in the two MOSFETs is expected to be uncorrelated.

We fabricate a dual gate MOSFET device according to the same methods outlined in Appendix A. Figure 4-14(a) shows a false colored scanning electron micrograph of the device. The nanopattern is intended to be placed in the region between the two MOSFETs. Using electron beam lithography, we are able to precisely position a nanopattern in the gap between the electrodes. Our alignment procedure is outlined in Appendix B. Figure 4-14(b) shows a false colored scanning electron micrograph of

the device with a nanopattern. We measure the noise in each of the MOSFETs just as in the prior device. The DC current in the two MOSFET channels as a function of time is displayed in Figure 4-14(c). From examination of the random telegraph noise in each MOSFET, it is evident that the noise is uncorrelated as expected. A correlation analysis (shown in Figure 4-14(d) further confirms that are insensitive to charge fluctuations in the neighboring MOSFET. We note that to maximize the signal in the MOSFETs from charge fluctuations in a nearby nanopattern, the charge sensors should be positioned as close as possible to it.

The electric potential established by an electron in the nanopattern, a distance r from the charge sensor does not scale according to 1/r as one might naively expect. Rather, screening of the electron by an image charge in the silicon substrate causes the electric potential to decrease faster than 1/r. The silicon dioxide is 100 nm thick, which sets the distance between an electron in the thin film and its associated image charge in the silicon dioxide. Thus, we expect the electric potential established by an electron in the material to decrease approximately according to $1/r^3$ for distances greater than 100 nm from the MOSFET. We also note that when an electron hops from one location to another, the signal observed by the charge sensor does not scale according to the absolute electric potential of the electron but according to the change in the electric potential at the sensor. Therefore, the MOSFET sensors displayed in Figure 4-14(a) and (b) will be most sensitive to electron hops that are transverse to the sensor rather than parallel to the sensor.

To conclude, we have shown that our charge sensors can be used to study conductance fluctuations in quantum dot arrays. The incorporation of a second sensor, can help to eliminate sensor noise, and improve the signal to noise. We expect that the improvements in signal to noise will expand the capabilities of our charge sensing technique. In particular, it may enable the measurement of individual electron hopping events in colloidal arrays as well as other nanostructured materials.

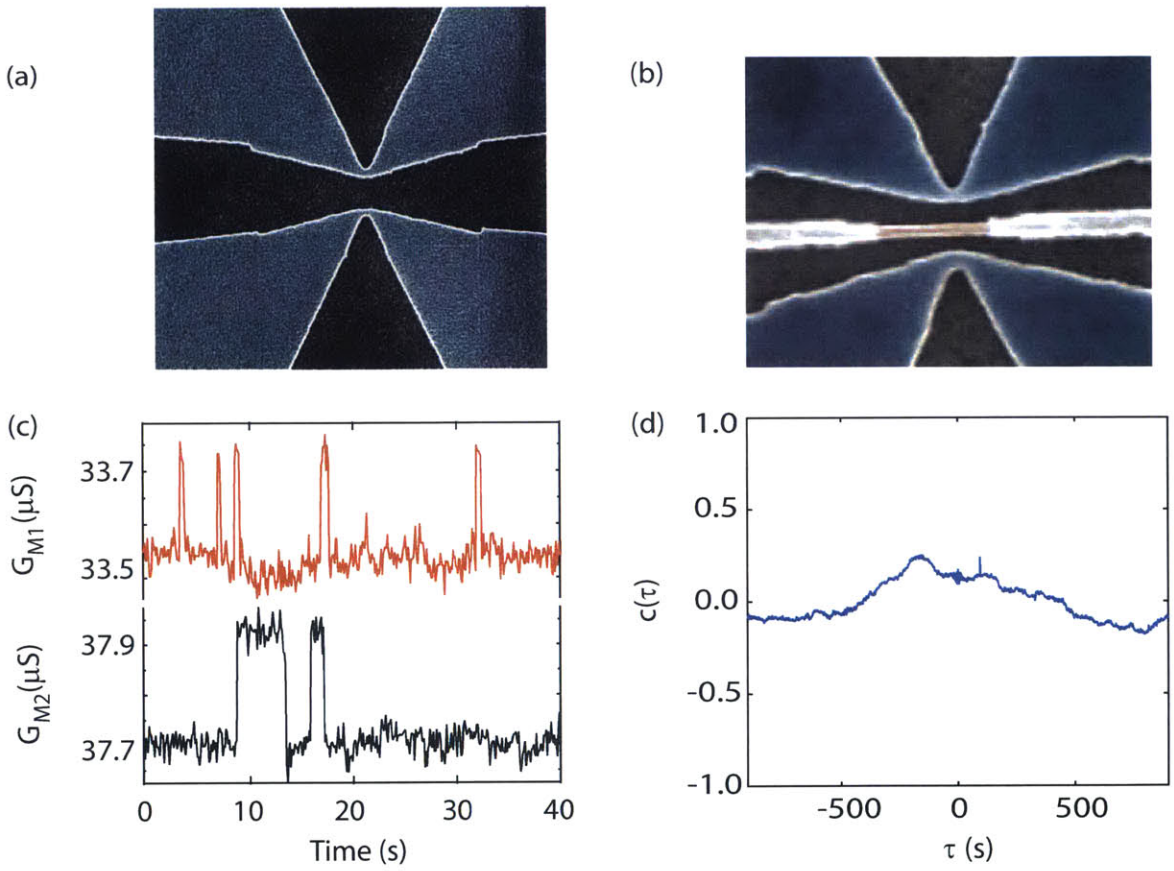

Figure 4-14: Dual MOSFET charge sensing (a) False colored Scanning electron micrograph of two MOSFET gates, placed 200 nm apart. (b) False colored scanning electron micrograph of a nanopatterned PbS array placed 50 nm away from each sensor. The alignment procedure to achieve this configuration is discussed in Appendix B. (c) Conductance of both MOSFETs in (a), measured with a DC bias, as a function of time. The upper and lower panels show conductance of the top and the bottom MOSFET respectively. Telegraph events in each trace originate from electron trapping and de-trapping in the nearby oxide. (d) Correlation analysis between the MOSFET conductances, shows no peaks, confirming that the sensor noise in each of the MOSFETs is uncorrelated.

Chapter 5

Conclusions and Future work

We conclude this thesis by briefly summarizing the results presented in the previous chapters, and by putting forward ideas for future experiments. We have demonstrated the ability to form nanoscale patterns of colloidal quantum dot arrays that are electrically conductive and structurally continuous. Using electron-beam lithography and lift-off, we achieve patterns with nanometer resolution that can be easily integrated into a device structure. The process allows for flexibility in the choice of core material, ligand, and solvent without constraints on the choice or design of the substrate. We have performed the first electrical measurements on nanopatterned quantum dot arrays that are free of the clustering and cracks typically found in films of micrometer dimensions or larger. The electrical conductivity of the patterned, nanoscale films is 180 times higher than the conductivity of larger, drop-cast films in which the dots typically form clusters.

In Chapter 3, we use nanolithography to make arrays as small as 15 dots wide, and find very large noise in the current through them. The noise is proportional to the current when the latter is varied by applying drain-source or gate voltage in a field-effect structure or when changing temperature, showing that it results from a conductance rather than charge fluctuations. The noise scales with the width of the nanopattern, increasing to 75% of the current for 40 nm wide nanopatterns. It is observed for PbS dots with the native oleate ligand as well as butylamine ligand, suggesting a more universal origin. The power spectral density of the noise follows

a power law in frequency. In some cases, the noise is telegraph-like, switching on and off, suddenly. The off-times also follow a power law distribution, also known as Levy statistics, typically observed in fluorescence blinking in individual CdSe dots. All of these observations are consistent with a model, in which the current is carried by quasi-one-dimensional paths that can be interrupted by trapping of charge. Our results suggest that the limitation of the current by quasi-one-dimensional channels and its noise and decay may be general features of colloidal quantum dot arrays.

A natural step forward would then be to find a way to eliminate these fluctuations, possibly by decreasing the number of trap sites on the surface by chemical passivation. The growth of dots with a shell is another approach recently used for suppressing blinking in CdSe dots, as demonstrated by Chen et al [13]. Our collaborators have successfully synthesized PbS dots with a monolayer thick CdS shells, and it would be interesting to study noise in these structures.

In Chapter 4, we study transport in nanopatterned oleic acid and butylamine capped PbS dots using integrated charge sensors. Integrated charge sensors have had a big impact in the study of lithographic quantum dots, enabling the study of slow electron dynamics. To our knowledge, charge sensors had not been previously used to study transport in colloidal dot systems. Our nanopatterns are easily integrated with a narrow channel MOSFET used as a charge sensor. By performing a time resolved measurement of charge, we use the sensors to measure extremely high resistances, using fairly low voltages (~ 0.5 V).

We present the first transport measurements on unannealed, ordered arrays of oleic acid capped PbS dots. We find that the conductance is well-described by a simply activated form, consistent with nearest neighbor hopping between dots. Nearest neighbor hopping is not unexpected, considering the large tunnel barrier between dots, and is also consistent with previous reports on annealed PbSe dots with the same ligand. The transport can be described by a model in which the Fermi energy lies in acceptor states in the bandgap and charge carriers hop between localized sites intrinsic to the dots. We find that holes are the majority carriers, and we expect an activation energy of approximately 70 meV near zero bias. An electric field lowers the

activation energy, and we find two associated length scales. One length corresponds to the distance between the acceptor states on the surface of the dot and the intrinsic state inside the dot, namely the distance over which a hole is excited to the valence state. The second length scale is equivalent to the interdot separation. As we move to butylamine capped PbS dots, we find that the data is inconsistent with nearest neighbor conduction, and instead fits well to Motts variable range hopping form. We find an exponential dependence on the field, consistent with the theoretical model of Pollak and Reiss for variable range hopping in low electric fields. We extract a localization length of 1.7 nm, which seems reasonable. Surprisingly, we do not observe a crossover to nearest neighbor hopping even at room temperature. The transition to variable range hopping when we change the ligand, can be understood in terms of increased wavefunction overlap between the dots.

Our technique to measure high resistances can be applied to a variety of interesting solid state systems. The most intriguing to us are binary nanocrystal superlattices (BNSLs). As the formation of these is stabilized by long ligands, electrical conduction has not been measured in semiconducting binary supperlattices. The charge sensing technique would allow transport measurements on these systems once the challenge of nanopatterning monolayers is met. Our charge-sensing resistance measurement technique is applicable even with blocking contacts. CdSe quantum dots are ideally suited for these measurements, as they form blocking contacts with most metals. CdSe dots also have a smaller dielectric constant, which would imply a large Coulomb energy. To highlight the application of our charge sensor as a technique to study transport we plot the resistance of a material as a function of the observed/expected contact resistance (Figure 5-1). Metals and crystalline semiconductors have low electrical resistance, and can be probed easily with conventional transport techniques. Our technique would be applicable to highly resistive materials such as amorphous and organic semiconductors, colloidal dot arrays, high-k dielectrics, and other materials which have a relatively high electrical resistance and may or may not form blocking contacts.

A primary goal in the study of artificial solids, has been to observe collective

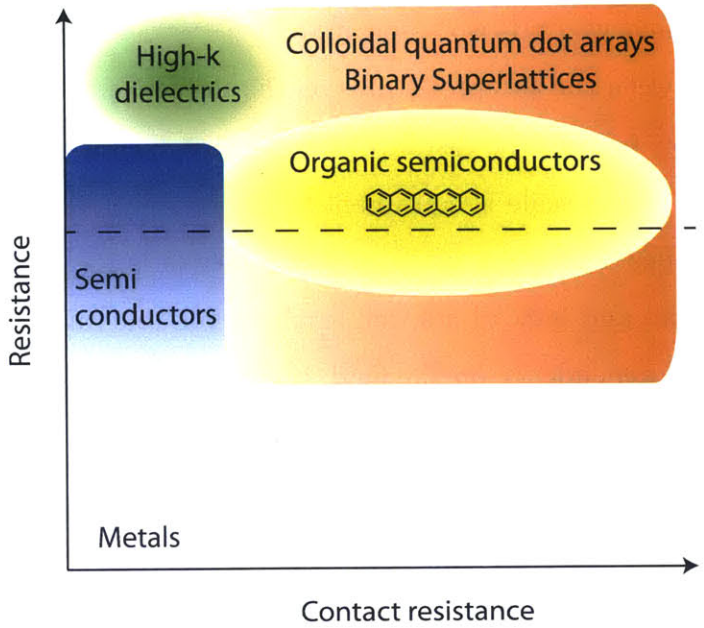

Figure 5-1: Applications of charge sensing to study transport. We plot the resistance of the material under study as a function of the observed/expected contact resistance. Our technique can be used to probe transport for materials above the black dashed line; highly resistive materials, which may have a high contact resistance.

behavior and Mott-Hubbard physics. Even after minimizing the stuructural disorder using nanopatterning, we find that the transport in the arrays is still disorder limited. However, our work highlights the impact of the capping ligand on the transport mechanism. The group of Talapin has made great progress in making highly ordered quantum dot arrays using novel inorganic/organic hybrid ligands, which show higher conductivities and impressive transistor characteristics. The tunnel barrier between the dots is estimated to be $\sim 44\ \mathrm{k}\Omega$. It would be interesting to study transport in these systems at low temperatures, using charge sensing measurements.

A different direction is the study of transport in lithographic arrays [103]. By investigating transport through a finite two dimensional mesoscopic periodic potential, consisting of an array of lateral quantum dots with electron density controlled by a global top gate, a transition from an insulating state at low bias voltages to a conducting state at high bias voltages is observed. The high-bias behavior suggests underdamped transport through a periodic washboard potential resulting from collective motion. In addition to the general question of whether quantum or classical

transport dominates, these artificial periodic potentials may provide further insight into the extensive work on colloidal quantum dot arrays.

Appendix A

MOSFET Fabrication

In this appendix, we give details on MOSFET fabrication. The details are similar to the procedures outlined in Kenneth MacLean's thesis [60], with a few modifications. For completeness sake, we list all of the steps here again. MOSFET fabrication was performed in the Microsystems Technology Laboratory (MTL), at MIT.

The steps listed below are primarily for fabricating n-channel MOSFETs. We were also able to fabricate p-channel MOSFETs using the same basic steps, however, we did not use those owing to very low mobilities. The modification needed for p-channel MOSFETs have been pointed out wherever needed.

The starting material for n-channel MOSFETs are prime 6 inch Silicon wafers, doped with Boron.The resistivity of the wafers was measured to be $\approx 3\Omega$cm.

1. **Define Active region**

   (a) **RCA clean and Field oxide growth** The RCA clean is a standard set of wafer cleaning steps regularly performed before high-temperature processing steps, such as oxidation and diffusion, in Silicon fabrication. The clean has three steps designed to remove organic contamination, native oxide and ionic contamination. After the clean, we grow a wet thermal oxide in tube 5D-ThickOxide in the ICL's diffusion system. The recipe 4W1050 (time= 3 hours 2 minutes), grows $\approx 1\mu$m of thermal oxide. The thickness of the oxide was verified by the ellipsometer (UV1280) in ICL.

(b) **Photolithography** Pattern the field oxide for etching. This step was accomplished using the ICL's coater/developer track and Nikon i-line optical stepper. The masks used for photolithography are chrome on quartz, and were patterned by Microtronics. The first photolithography step defines the active region of the MOSFET.

(c) **Etch Field Oxide** Etch the field oxide in BOE (Buffered oxide etch)for 14 minutes and 25 seconds at the ICL's oxide wet bench. The time needed to etch was calculated based on the etch rate. We overetch by about 20 percent.

(d) **Strip Photoresist** Remove photoresist using ICL's oxygen plasma asher. This takes 3 minutes. However, if photoresist residue can still e seen under the optical microscope, a piranha etch may be needed.

2. **Ion implantation**

(a) **RCA clean and Protective Oxide Growth** After a standard RCA clean, we grow 50nm of protective oxide in tube 5D, using recipe 4D1000. The thin oxide layer serves to protect the Silicon substrate from damage during ion implantation. Excessive surface damage can make it difficult to make good electrical contact to the implanted regions.

(b) **Photolithography** Define the area for ion implantation.

(c) **Ion Implantation** We send the wafers to Innovion for ion implantation. They need to be doped with phosphorous. The dose is 7×10^{15} cm^{-2}, at an energy of 180keV with a 7 degree tilt.

(d) **Strip Photoresist** Following ion implantation, the photoresist is difficult to remove. After ashing for 3 minutes in an oxygen plasma, a double Piranha clean (Blue and Green) is needed to completely remove the resist.

(e) **RCA Clean and Post Ion Implantation Anneal** We clean the wafers in RCA, and anneal for 30 minutes at 1000°C in Nitrogen in tube 5B. The recipe used is 2A1000.

(f) **Etch off Protective oxide** The thin oxide layer is removed by immersing the wafers in BOE for 1 minute.

3. **Gate oxide and MOSFET gate**

(a) **RCA clean and Grow Gate oxide** After a standard RCA clean, we grow 100nm of oxide in tube 5A-GateOx. The recipe used is 1D1000 (time=160 minutes). We leave the wafers in the furnace overnight at 400°C.

(b) **n+ Polysilicon Deposition** We deposit 80nm of phosphorous doped polysilicon using LPCVD (Low Pressure Chemical Vapor Deposition). The deposition is performed in tube 6A-nPoly at 560°C and the recipe used is DOPED PH3 FLAT (time=77 minutes).

(c) **Polysilicon Anneal** This step is intended to reduce the grain boundaries in polysilicon and increase it's conductivity. The recipe 2A900, anneals for 30 minutes at 900°C. We use tube 5B-anneal. The polysilicon color changes from brown to green.

(d) **Polysilicon Oxide Strip** We etch the wafers in BOE for 30 seconds, in order to remove the native oxide on Polysilicon. This step is crucial for subsequent polysilicon etch steps. The native oxide can make reactive ion etching of polysilicon difficult.

(e) **Photolithography** Define alignment marks to be used for electron beam lithography.

(f) **Etch Polysilicon and oxide** We etch the polysilicon using reactive ion etching in AME model P5000 (recipe Keith CP, with main step $\approx$ 60 seconds). We then etch through the oxide for 20 minutes in BOE.

(g) **Strip Photoresist** Using asher (3 minutes Oxygen Plasma).

(h) **Backside Etch** We coat the front of the wafer with photoresist. We etch the back of the wafer using the same recipe used to define the alignment marks (Keith CP for 60 seconds, followed by 20 minutes in BOE).

(i) **Strip Photoresist**

(j) **Electron beam Lithography** We spin on negative e-beam resist 4 % HSQ, and perform electron beam lithography using Raith 150 to define the narrow parts of the MOSFET gate. We write the pattern with a voltage of 30keV, 10nm step size and 100μm write field. The e-beam lithography steps are described in more detail in Appendix B. The patterns are developed in CD 26 for 5 minutes, followed by a DI water rinse.

(k) **Photolithography** Define the large parts of the polysilicon MOSFET gate.

(l) **Polysilicon Etch** We use magnetically enhanced reactive ion etching (RIE)in a Cl_2:HBr chemistry to etch the polysilicon. We use the recipe Keith CP with the following parameters:

- **Gas Stabilization for main etch** Cl_2:HBr 20:20 Scc, t_s, m=10 s, P=200 mtorr, B=50 Gauss, RF=0.
- **Main etch** Cl_2:HBr 20:20 Scc, t_m=22 s, P=200 mtorr, B=50 Gauss, RF = 350 W.
- **Gas stabilization for Overetch** HBr 40 Scc, $t_{s,o}$ = 10s, P=100 mtorr, B=50 Gauss, RF=0
- **Overetch Step** HBr 40 Scc, t_o = 0s, P=100 mtorr, B=50 Gauss, RF=50W

(m) **Strip Photoresist**

4. **Stringer Etch**

(a) **Photolithography** Define area for a stringer etch. The pattern covers the polysilicon gate structure in photresist.

(b) **Stringer Etch** This step is designed to remove any remaining polysilicon from the edges of the active region. We use the same recipe as the gate etch step, except that the time for the first two steps are set to zero, and the time for the overetch step is changed to 900 seconds.

(c) **Strip Photoresist**

5. **Source and Drain contacts**

   (a) **Photolithography** This step patterns holes to be etched in the oxide to contact the ion implanted regions.

   (b) **Etch Oxide** The wafers are etched in BOE for 2 minutes and 30 seconds. Ellipsometry is used to verify that no oxide remains above the implanted regions where the holes are etched. One should move to the next three steps, immediately after the etch, in order to minimize the native oxide that will grow where the holes are etched.

   (c) **Strip Photoresist**

   (d) **Double Piranha Clean followed by HF dip** This is a standard pre-deposition clean. The HF dip is carried out at the Piranha station for 30 seconds, in order to remove native oxide.

   (e) **Deposit Aluminum** We sputter 2.5kÅof pure Aluminum using the Applied Materials Endura system.

6. **Define Al electrodes**

   (a) **Photolithography** This step patterns the Aluminum for the etch in the next step.

   (b) **PAN etch** We etch the Aluminum in PAN Al etchant (H_3PO_4:CH_3C00H:HNO_3:H_2O, 16:1:1:2). Because of the native oxide on the aluminum, the time required for the PAN etch can vary, and so the etch needs to be monitored by eye.

   (c) **Strip Photoresist**

   (d) **Sinter Contacts** The wafer is sintered in forming gas in Tube A3 in TRL, at 425°C for 30 minutes. This step is crucial for making good electrical contact to the implanted regions.

7. **Diesaw** We spin photoresist on the surface to protect the wafer, and then dice it with a 220μm silicon blade.

The MOSFET fabrication is now completed. After this, we need to pattern gold electrodes and the nanopatterned arrays adjacent to the MOSFET gate. These steps require accurate placement with e-beam lithography, and the fine alignment details are discussed in appendix B.

Appendix B

Electron Beam Lithography

For our device fabrication, the most challenging aspect was high precision alignment of features. Among the multiple steps sensitive to alignment, the first is the alignment of the MOSFET gate to optical features already present on the device. Second is the alignment of the gold electrodes to the gate, and finally the alignment of the nanopattern to both, the gate and the electrodes. We use the Raith 150, at the scanning electron beam lithography (SEBL) and the Elionix ELS-125 at MTL for e-beam lithography. In this appendix, we briefly discuss the alignment procedures used for both these tools.

B.1 Electron beam lithography using Elionix-ELS125

The elionix system operates at 125 keV, and can easily provide better than 10 nm alignment for well defined alignment marks. We use the Elionix system to pattern the gold electrodes and the Aluminum MOSFET gate. We also pattern alignment marks that are subsequently used to place the nanopatterned dot arrays. However, this final alignment step is performed using the Raith 150, as discussed in section B.2.

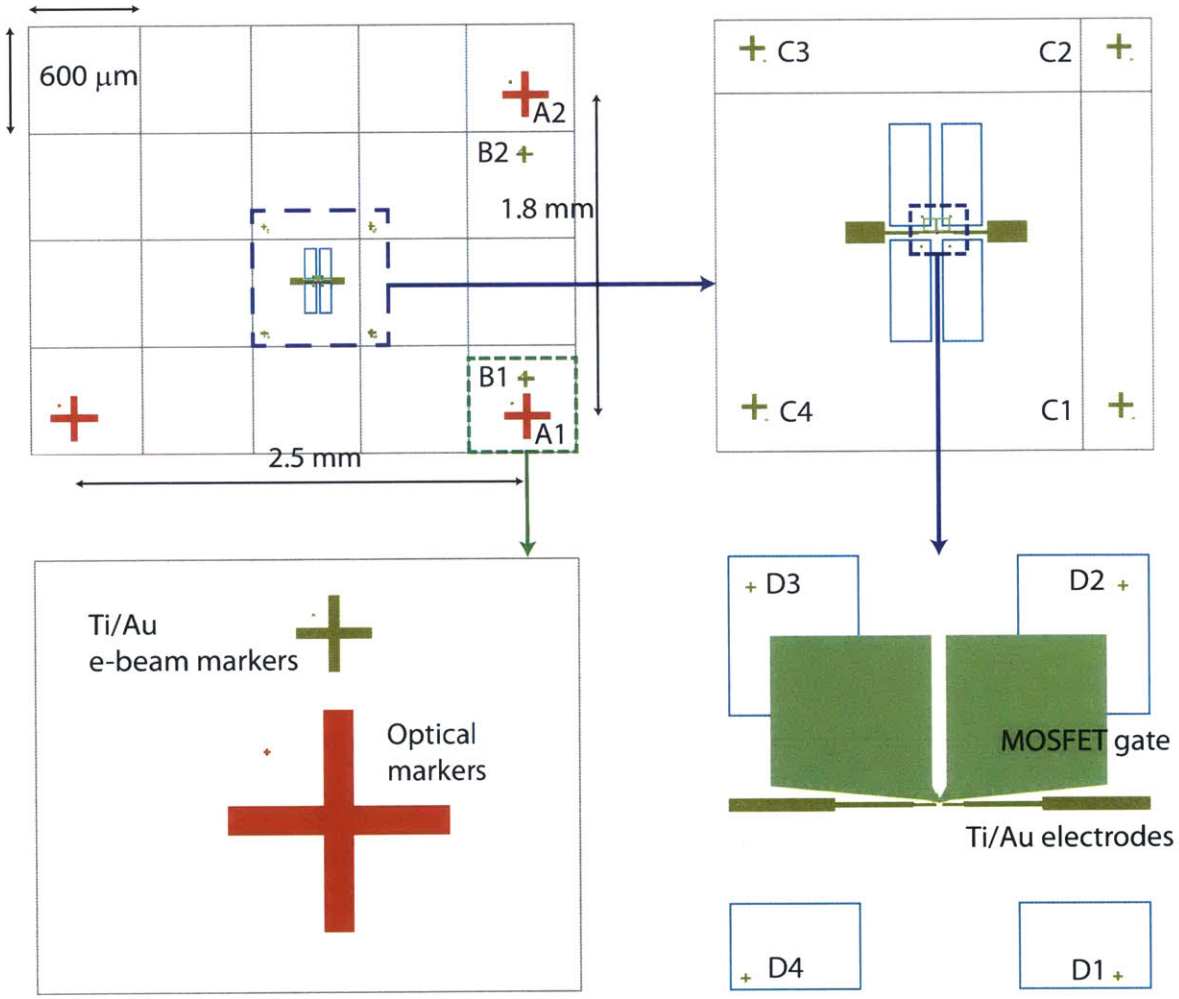

Figure B-1: Layout file for charge sensor adjacent to the nanopattern. The top left box, shows the optical alignment markers (red), A1 and A2, used for patterning the gold electrodes, and the e-beam alignment markers, B1 and B2 (golden), used for the MOSFET gate alignment. Note that both these sets of alignment markers are separated in Y, but have the same X-coordinate. Gray boxes show how the edges of the 600 μm write-fields. The top right design, is a zoom in of the area in the blue box and reveals the markers (golden), C1-C4, used for four-point alignment of the MOSFET gate. Further magnification of the design, reveals the alignment markers used for positioning the nanopattern (D1-D4, bottom right), and the optical and e-beam alignment markers (bottom left).

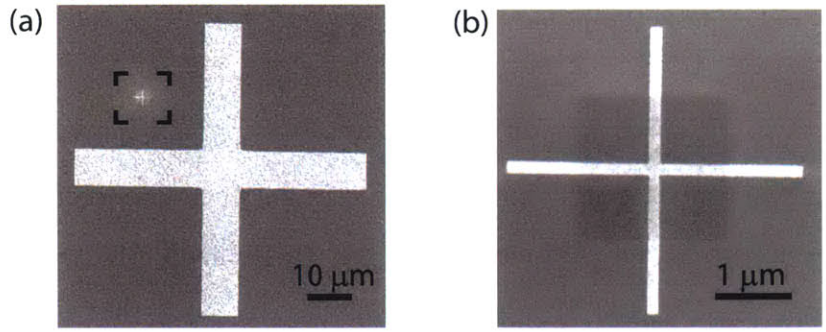

Figure B-2: Scanning electron micrographs of the Ti/Au e-beam electron mark B1 using the Elionix system. The image on the right is the magnified version of the area in the black box from the left image.

Layer design and alignment marks

The first step is the design of the layout file, which is done using Clewin design editor. Every feature is saved as a different layer as shown in Figure B-1. We use optically created alignment marks, which are etched 1 μm deep into Silicon, to pattern the gold electrodes, and also write a new set of alignment marks. This new set, created using Ti/Au layer (7 nm/50 nm) is used to precisely align the MOSFET gate to the patterned gold electrodes.

There are two types of alignment options available in the Elionix system, namely the auto registration and the manual registration mode. In the auto registration mode, the mark is searched automatically by scanning the mark with a beam and determining the mark center by the line profile obtained. This method is highly dependent on the quality of the mark and any deformation results in misalignment or the Elionix being unable to find the mark. The alternative is the manual registration where the center of the mark is determined visually and alignment is done manually. More accurate alignment is obtained by the manual method and is therefore our preferred choice.

For manual alignment, atleast two alignment marks are required and these must have the same X-coordinate and be separated in Y. The larger the separation between the marks, the better is the rotational displacement correction and alignment. The elionix also offers a 4-point correction for further precision, which must be carried

out after the two point alignment. For the 4-point correction, we nest four more alignment marks as close to the area of interest as possible.

Figure B-1 shows parts of the layout file at different magnifications to reveal all the features. The top left box, shows the optical alignment markers (red), A1 and A2, used for patterning the gold electrodes, and the e-beam alignment markers, B1 and B2 (golden), used for the MOSFET gate alignment. Note that both these sets of alignment markers are separated in Y, but have the same X-coordinate. Gray boxes show how the pattern is broken up into 600 μm write-fields. The top right design, is a zoom in of the area in the blue box and reveals the markers (golden), C1-C4, used for four-point alignment. Further magnification of the design, reveals the alignment markers used for positioning the nanopattern (D1-D4, bottom right), and the optical and e-beam alignment markers (bottom left). We write the gold electrodes first, because Ti/Au alignment markers are really easy to image with the Elionix, as seen by the images in Figure B-2.

Coating and preparation for exposure

To prepare the substrate for lithography, we scratch the back of the chip with a diamond scribe, and sonicate in Acetone, Methanol and Isopropanol for five minutes each, in order to remove any organic residue. To pattern the gold electrodes, we spin on a single layer of PMMA (950 A4) at 4000 rpm for 1 minute. At this spin speed, the resist thickness is estimated to be approximately 200 nm. We then soft bake the substrate at 180 °C for five minutes. To pattern the Aluminum MOSFET gate, we spin another layer of PMMA 950 A4 on top of the already baked layer, and bake for another 5 minutes, to get a total resist thickness of $\sim$ 400 nm. In preparation for exposure, we convert the GDSII files generated by Clewin, into .CON files using the Layout Beamer software.

Exposure and development

We carry out the exposure of the desired pattern in accordance with the steps detailed below:

1. **Sample Loading:** We mount the resist coated substrate into the Elionix sample holder, and roughly note the position of the alignment marks. We then follow the standard procedure for loading the sample. We use an acceleration voltage of 125 keV and a beam current of 5 nA. Immediately after loading the sample, we open the isolation valve and recall the 5 nA settings from the beam memory. We then drive to the Faraday cup and measure the current, to ensure that it is close to the expected value.

2. **Focus and Stigmate the beam:** Using the SEM side, we drive to 'Reference', which is the location of nanocrystals on the sample holder, and initiate the auto Focus and Stigmate routine.

3. **Exposure:** We now move to the Elionix side and open the layout file. We identify the locations of the REG-2 (and REG-4, if applicable) in the layout file. We proceed to 'Set Options', and enter the registration/alignment options. Using the SEM side, we drive to the approximate location of the alignment mark with a lower Y coordinate, and center it on the screen. We then overlay the pattern on this location, using the 'Move pattern' and 'Read Stage Position' options. Once the exposure starts, the stage drives to the co-ordinate of the first alignment mark. At this point, we go to the highest magnification possible with the features, and center the alignment marks on screen, scanning with a slow scan speed. We repeat this process at the second alignment mark as well. The stage then drives to the field correction marks, and tries to correct for the calculated rotation angle. After the field correction, the stage again drives to the first alignment mark. At this stage, we basically have to check that the alignment mark is still centered, and we correct for small shifts by shifting the beam rather than moving the stage. If the REG-4 option was selected, the software now moves to the four alignment marks. As these REG-4 marks (C1-C4), are close to other features, we image them only at very high magnification (30-40 KX). After this step, the system calculates the rotation error, and if it is less than the tolerance value entered in the schedule file (typically 0.03 mrad),

it will start the exposure.

4. **Development:** We develop the patterns using 1:3 MIBK:isopropyl alcohol for 90 seconds, followed by a rinse in isopropyl alcohol. As these patterns are written with an acceleration voltage of 125 keV, we found that even small amounts of moisture, can cause the patterns to self develop and distort the nanoscale features. We, therefore, develop the patterns and proceed to deposition, immediately after exposure.

B.2 Electron beam lithography using Raith150

The Raith150 operates at relatively low voltages (10-30 keV), so is the best tool to use for imaging and minimizing radiation damage. We use the tool to align our nanopatterns. A step by step overview of the lithography procedure is given below:

1. **Scratch back of chip:** We use a diamond scribe to scratch the back of the chip so that the chip is well grounded during lithography.

2. **Clean chip:** We sonicate the chips in acetone, methanol and isopropyl alcohol for 5 minutes each, and then blow dry with nitrogen.

3. **Spin on e-beam resist:** For our nanopatterns, we use PMMA 950 A2 from Microchem. We spin two layers of 950 PMMA A2, and the total resist thickness is $\approx$ 100 nm. It is good to examine the chips carefully after spinning to ensure that the resist looks uniform. at 4000 rpm for 1 minute. We bake the chip at 180° C for five minutes to drive off moisture from the surface. Then spin the first layer of resist. We bake the resist for another 5 minutes, and then spin a second layer, followed by another 5 minute bake.

4. **Gold nanocrystal deposition:** We put 100 nm gold nanocrystals on the chip with a micro-pipette. These are used to focus and stigmate the electron beam. We avoid putting the nanocrystals near the edge bead, because if the resist

under the nanocrystals is too thick, it will charge up and make it impossible to focus the beam properly.

5. **Load sample, measure beam current and locate alignment marks:** We make sure to to align the axes of our sample pattern (to which we align the write) with the axes of the Raith stage (by eye), as this generally makes navigating the wafer a lot easier. We follow the appropriate loading procedures measured the beam current at the Faraday cup immediately after loading. If we measure no beam current, then it usually means the sample stage is not properly grounded. This problem can usually be fixed by shaking the stage manually using piezo controllers, but sometimes, one needs to unload and load again. We set the voltage to 10 keV after loading the samples, and record the rough XY positions for the gold nanocrystals and our alignment marks, because imaging is very easy at 10keV.

6. **Focus, Stigmate and Aperture Align:** We ramp up the voltage to 30 keV, switch to the SE2 detector, measure the beam current at the Faraday cup, and drive to the noted XY position of the gold nanocrystals. We focus and stigmate the electron beam here, and record the XY co-ordinates from the Raith software at this acceleration voltage.

7. **Field alignment:** We use the standard field alignment procedures at the gold nanocrystals, with step sizes of 20 μm, 5 μm and 1 μm. This step aligns the electron beam to the stage axes. We record the zoom, shift and rotation values.

8. **Adjust UVW:** We perform a coordinate transformation at our alignment marks, using the Raith side for imaging.

9. **Field alignment:** We drive back to the gold nanocrystals and perform another field alignment, to align the electron beam with the sample. We record the shift and rotation values again. We repeat the adjust UVW procedure followed by the field alignment till the shift and rotation values converge.

10. **Exposure:** Once the values converge, we expose our nanopattern with an areal dose of 600 $\mu C/\text{cm}^2$, and step size of 0.01 μm. Immediately after the write, we move the sample away from the beam. Even though the beam is blanked off after writing, it has been our experience that the blanker sometimes does not work quite as well, which may cause overexposure of the sample sitting directly underneath the beam for extended periods of time.

11. **Develop:** After exposure, we develop the chip in 1:3 MIBK:isopropyl alcohol for 90 seconds, followed by a rinse in isopropyl alcohol. We blow dry the chip and proceed to dropcasting the colloidal dots.

Bibliography

[1] Vinay Ambegaokar, BI Halperin, and JS Langer. Hopping conductivity in disordered systems. *Physical review B*, 4(8):2612, 1971.

[2] MG Ancona, W Kruppa, RW Rendell, AW Snow, D Park, and JB Boos. Coulomb blockade in single-layer au nanocluster films. *Physical Review B*, 64(3):033408, 2001.

[3] Mikhail Artemyev, Dmitry Kisiel, Sergey Abmiotko, Maria N Antipina, Gennady B Khomutov, Vladimir V Kislov, and Anna A Rakhnyanskaya. Self-organized, highly luminescent cdse nanorod-dna complexes. *Journal of the American Chemical Society*, 126(34):10594–10597, 2004.

[4] Wan Ki Bae, Jeonghun Kwak, Jaehoon Lim, Donggu Lee, Min Ki Nam, Kookheon Char, Changhee Lee, and Seonghoon Lee. Multicolored light-emitting diodes based on all-quantum-dot multilayer films using layer-by-layer assembly method. *Nano letters*, 10(7):2368–2373, 2010.

[5] Alexander A Balandin. Low-frequency 1/f noise in graphene devices. *Nature nanotechnology*, 8(8):549–555, 2013.

[6] Moungi G Bawendi, John R Haavisto, Farhad Hakimi, and Richard Tumminelli. Quantum dot laser, November 9 1993. US Patent 5,260,957.

[7] S Bhattacharya, JP Stokes, Mark O Robbins, and RA Klemm. Origin of broadband noise in charge-density-wave conductors. *Physical review letters*, 54(22):2453, 1985.

[8] Aveek Bid, Nissim Ofek, Hiroyuki Inoue, Moty Heiblum, CL Kane, Vladimir Umansky, and Diana Mahalu. Observation of neutral modes in the fractional quantum hall regime. *Nature*, 466(7306):585–590, 2010.

[9] CT Black, CB Murray, RL Sandstrom, and Shouheng Sun. Spin-dependent tunneling in self-assembled cobalt-nanocrystal superlattices. *Science*, 290(5494):1131–1134, 2000.

[10] Ya M Blanter and Marcus Büttiker. Shot noise in mesoscopic conductors. *Physics reports*, 336(1):1–166, 2000.

[11] Patrick R Brown, Donghun Kim, Richard R Lunt, Ni Zhao, Moungi G Bawendi, Jeffrey C Grossman, and Vladimir Bulovic. Energy level modification in lead sulfide quantum dot thin films through ligand exchange. *ACS nano*, 2014.

[12] P Bruschi, F Cacialli, A Nannini, and B Neri. Low-frequency resistance fluctuation measurements on conducting polymer thin-film resistors. *Journal of applied physics*, 76(6):3640–3644, 1994.

[13] Ou Chen, Jing Zhao, Vikash P Chauhan, Jian Cui, Cliff Wong, Daniel K Harris, He Wei, Hee-Sun Han, Dai Fukumura, Rakesh K Jain, et al. Compact high-quality cdse-cds core-shell nanocrystals with narrow emission linewidths and suppressed blinking. *Nature materials*, 12(5):445–451, 2013.

[14] Chia-Hao M Chuang, Patrick R Brown, Vladimir Bulović, and Moungi G Bawendi. Improved performance and stability in quantum dot solar cells through band alignment engineering. *Nature materials*, 13:796–801, 2014.

[15] CP Collier, T Vossmeyer, and JR Heath. Nanocrystal superlattices. *Annual Review of Physical Chemistry*, 49(1):371–404, 1998.

[16] Raoul E Correa, Eric A Dauler, Gautham Nair, Si H Pan, Danna Rosenberg, Andrew J Kerman, Richard J Molnar, Xiaolong Hu, Francesco Marsili, Vikas Anant, et al. Single photon counting from individual nanocrystals in the infrared. *Nano Lett.*, 12(6):2953–2958, 2012.

[17] Susan Cox, J Singleton, RD McDonald, A Migliori, and PB Littlewood. Sliding charge-density wave in manganites. *Nature materials*, 7(1):25–30, 2008.

[18] Richard Dalven. A review of the semiconductor properties of pbte, pbse, pbs and pbo. *Infrared physics*, 9(4):141–184, 1969.

[19] R De-Picciotto, M Reznikov, M Heiblum, V Umansky, G Bunin, and D Mahalu. Direct observation of a fractional charge. *Nature*, 389(6647):162–164, 1997.

[20] Angang Dong, Xingchen Ye, Jun Chen, and Christopher B Murray. Two-dimensional binary and ternary nanocrystal superlattices: the case of monolayers and bilayers. *Nano letters*, 11(4):1804–1809, 2011.

[21] M Drndić, MV Jarosz, NY Morgan, MA Kastner, and MG Bawendi. Transport properties of annealed cdse colloidal nanocrystal solids. *Journal of applied physics*, 92(12):7498–7503, 2002.

[22] P Dutta and PM Horn. Low-frequency fluctuations in solids: 1/f noise. *Reviews of Modern physics*, 53(3), 1981.

[23] J. W. Eberhard and P. M. Horn. Excess 1/f noise in metals. *Phys. Rev. B*, 18:6681–6693, Dec 1978.

[24] Al L Efros and M Rosen. The electronic structure of semiconductor nanocrystals 1. *Annual Review of Materials Science*, 30(1):475–521, 2000.

[25] Alexander L Efros. Nanocrystals: Almost always bright. *Nature materials*, 7(8):612–613, 2008.

[26] PJ Elliott, AD Yoffe, and EA Davis. Hopping conduction in amorphous germanium. In *TETRAHEDRALLY BONDED AMORPHOUS SEMICONDUCTORS: International Conference*, volume 20, pages 311–319. AIP Publishing, 1974.

[27] Yuval Gefen, Wei-Heng Shih, Robert B Laibowitz, and JM Viggiano. Nonlinear behavior near the percolation metal-insulator transition. *Physical review letters*, 57(24):3097, 1986.

[28] Scott Geyer, Venda J Porter, Jonathan E Halpert, Tamar S Mentzel, Marc A Kastner, and Moungi G Bawendi. Charge transport in mixed cdse and cdte colloidal nanocrystal films. *Physical Review B*, 82(15):155201, 2010.

[29] DS Ginger and NC Greenham. Charge injection and transport in films of cdse nanocrystals. *Journal of Applied Physics*, 87(3):1361–1368, 2000.

[30] Meredith J Hampton, Joseph L Templeton, and Joseph M DeSimone. Direct patterning of cdse quantum dots into sub-100 nm structures. *Langmuir*, 26(5):3012–3015, 2010.

[31] Frederik Hetsch, Ni Zhao, Stephen V Kershaw, and Andrey L Rogach. Quantum dot field effect transistors. *Materials Today*, 16(9):312–325, 2013.

[32] Robert M Hill. Hopping conduction in amorphous solids. *Philosophical Magazine*, 24(192):1307–1325, 1971.

[33] FN Hooge. 1/f noise. *Physica B+ C*, 83(1):14–23, 1976.

[34] M. V. Jarosz, V. J. Porter, B. R. Fisher, M. A. Kastner, and M. G. Bawendi. Photoconductivity studies of treated cdse quantum dot films exhibiting increased exciton ionization efficiency. *Phys. Rev. B*, 70:195327, Nov 2004.

[35] Lucian Jdira, Peter Liljeroth, Eric Stoffels, Daniël Vanmaekelbergh, and Sylvia Speller. Size-dependent single-particle energy levels and interparticle coulomb interactions in cdse quantum dots measured by scanning tunneling spectroscopy. *Physical Review B*, 73(11):115305, 2006.

[36] Lucian Jdira, Karin Overgaag, Jan Gerritsen, Daniël Vanmaekelbergh, Peter Liljeroth, and Sylvia Speller. Scanning tunnelling spectroscopy on arrays of cdse quantum dots: response of wave functions to local electric fields. *Nano letters*, 8(11):4014–4019, 2008.

[37] J. B. Johnson. The schottky effect in low frequency circuits. *Phys. Rev.*, 26:71–85, Jul 1925.

[38] John B Johnson. Thermal agitation of electricity in conductors. *Nature*, 119(2984):50–51, 1927.

[39] John Bertrand Johnson. Thermal agitation of electricity in conductors. *Physical review*, 32(1):97, 1928.

[40] Shinae Jun, Eunjoo Jang, Jongjin Park, and Jongmin Kim. Photopatterned semiconductor nanocrystals and their electroluminescence from hybrid light-emitting devices. *Langmuir*, 22(6):2407–2410, 2006.

[41] CL Kane and Matthew PA Fisher. Nonequilibrium noise and fractional charge in the quantum hall effect. *Physical review letters*, 72(5):724, 1994.

[42] Moon Sung Kang, Ayaskanta Sahu, David J Norris, and C Daniel Frisbie. Size- and temperature-dependent charge transport in pbse nanocrystal thin films. *Nano letters*, 11(9):3887–3892, 2011.

[43] Sean Keuleyan, Emmanuel Lhuillier, Vuk Brajuskovic, and Philippe Guyot-Sionnest. Mid-infrared hgte colloidal quantum dot photodetectors. *Nature Photonics*, 5(8):489–493, 2011.

[44] LeeAnn Kim, Polina O Anikeeva, Seth A Coe-Sullivan, Jonathan S Steckel, Moungi G Bawendi, and Vladimir Bulovic. Contact printing of quantum dot light-emitting devices. *Nano letters*, 8(12):4513–4517, 2008.

[45] MJ Kirton and MJ Uren. Noise in solid-state microstructures: A new perspective on individual defects, interface states and low-frequency (1/) noise. *Advances in Physics*, 38(4):367–468, 1989.

[46] Sh.. Kogan. Cambridge University Press, 1996.

[47] Weon-kyu Koh, Sangameshwar R Saudari, Aaron T Fafarman, Cherie R Kagan, and Christopher B Murray. Thiocyanate-capped pbs nanocubes: ambipolar transport enables quantum dot based circuits on a flexible substrate. *Nano letters*, 11(11):4764–4767, 2011.

[48] Ghada I Koleilat, Larissa Levina, Harnik Shukla, Stefan H Myrskog, Sean Hinds, Andras G Pattantyus-Abraham, and Edward H Sargent. Efficient, stable infrared photovoltaics based on solution-cast colloidal quantum dots. *ACS nano*, 2(5):833–840, 2008.

[49] Gerasimos Konstantatos, Ian Howard, Armin Fischer, Sjoerd Hoogland, Jason Clifford, Ethan Klem, Larissa Levina, and Edward H Sargent. Ultrasensitive solution-cast quantum dot photodetectors. *Nature*, 442(7099):180–183, 2006.

[50] Maksym V Kovalenko, Marcus Scheele, and Dmitri V Talapin. Colloidal nanocrystals with molecular metal chalcogenide surface ligands. *Science*, 324(5933):1417–1420, 2009.

[51] M Kuno, JK Lee, BO Dabbousi, FV Mikulec, and MG Bawendi. The band edge luminescence of surface modified cdse nanocrystallites: Probing the luminescing state. *The Journal of chemical physics*, 106(23):9869–9882, 1997.

[52] C Kurdak, J Kim, A Kuo, JJ Lucido, LA Farina, X Bai, MP Rowe, and AJ Matzger. 1/f noise in gold nanoparticle chemosensors. *Applied Physics Letters*, 86(7):073506–073506, 2005.

[53] Xinzheng Lan, Silvia Masala, and Edward H Sargent. Charge-extraction strategies for colloidal quantum dot photovoltaics. *Nature materials*, 13(3):233–240, 2014.

[54] R. B. Laughlin. Anomalous quantum hall effect: An incompressible quantum fluid with fractionally charged excitations. *Phys. Rev. Lett.*, 50:1395–1398, May 1983.

[55] Jong-Soo Lee, Maksym V Kovalenko, Jing Huang, Dae Sung Chung, and Dmitri V Talapin. Band-like transport, high electron mobility and high photoconductivity in all-inorganic nanocrystal arrays. *Nature nanotechnology*, 6(6):348–352, 2011.

[56] Emmanuel Lhuillier, Sean Keuleyan, Heng Liu, and Philippe Guyot-Sionnest. Colloidal hgte material for low-cost detection into the mwir. *Journal of electronic materials*, 41(10):2725–2729, 2012.

[57] Heng Liu, Alexandre Pourret, and Philippe Guyot-Sionnest. Mott and efros-shklovskii variable range hopping in cdse quantum dots films. *ACS nano*, 4(9):5211–5216, 2010.

[58] Yao Liu, Markelle Gibbs, James Puthussery, Steven Gaik, Rachelle Ihly, Hugh W Hillhouse, and Matt Law. Dependence of carrier mobility on nanocrystal size and ligand length in pbse nanocrystal solids. *Nano letters*, 10(5):1960–1969, 2010.

[59] K MacLean, S Amasha, Iuliana P Radu, DM Zumbühl, MA Kastner, MP Hanson, and AC Gossard. Energy-dependent tunneling in a quantum dot. *Physical review letters*, 98(3):036802, 2007.

[60] Kenneth MacLean. *Charge detection in semiconductor nanostructures.* PhD thesis, Massachusetts Institute of Technology, 2010.

[61] Kenneth MacLean, Tamar S Mentzel, and Marc A Kastner. The effect of electrostatic screening on a nanometer scale electrometer. *Nano letters*, 11(1):30–34, 2010.

[62] Kenneth MacLean, Tamar S Mentzel, and Marc A Kastner. Measuring charge transport in a thin solid film using charge sensing. *Nano letters*, 10(3):1037–1040, 2010.

[63] M. P. Maher, T. L. Adelman, J. McCarten, D. A. DiCarlo, and R. E. Thorne. Size effects, phase slip, and the origin of $f^{-\alpha}$ noise in $nbse_3$. *Phys. Rev. B*, 43:9968–9971, Apr 1991.

[64] Klara Maturova, Sanjini U Nanayakkara, Joseph M Luther, and Jao van de Lagemaat. Fast current blinking in individual pbs and cdse quantum dots. *Nano letters*, 13(6):2338–2345, 2013.

[65] Steven A McDonald, Gerasimos Konstantatos, Shiguo Zhang, Paul W Cyr, Ethan JD Klem, Larissa Levina, and Edward H Sargent. Solution-processed pbs quantum dot infrared photodetectors and photovoltaics. *Nature materials*, 4(2):138–142, 2005.

[66] Alan Louis McWhorter et al. 1/f noise and related surface effects in germanium. 1955.

[67] T. S. Mentzel, V. J. Porter, S. Geyer, K. MacLean, M. G. Bawendi, and M. A. Kastner. Charge transport in pbse nanocrystal arrays. *Phys. Rev. B*, 77:075316, Feb 2008.

[68] Tamar S Mentzel, Kenneth MacLean, and Marc A Kastner. Contact-independent measurement of electrical conductance of a thin film with a nanoscale sensor. *Nano letters*, 11(10):4102–4106, 2011.

[69] Tamar S Mentzel, Darcy D Wanger, Nirat Ray, Brian J Walker, David Strasfeld, Moungi G Bawendi, and Marc A Kastner. Nanopatterned electrically conductive films of semiconductor nanocrystals. *Nano letters*, 12(8):4404–4408, 2012.

[70] TS Mentzel, VJ Porter, S Geyer, K MacLean, Moungi G Bawendi, and MA Kastner. Charge transport in pbse nanocrystal arrays. *Physical Review B*, 77(7):075316, 2008.

[71] A Alan Middleton and Ned S Wingreen. Collective transport in arrays of small metallic dots. *Physical review letters*, 71(19):3198, 1993.

[72] David Mocatta, Guy Cohen, Jonathan Schattner, Oded Millo, Eran Rabani, and Uri Banin. Heavily doped semiconductor nanocrystal quantum dots. *Science*, 332(6025):77–81, 2011.

[73] Nicole Y Morgan, CA Leatherdale, M Drndić, Mirna V Jarosz, Marc A Kastner, and Moungi Bawendi. Electronic transport in films of colloidal cdse nanocrystals. *Physical Review B*, 66(7):075339, 2002.

[74] Nicole Yen-i Morgan. *Electronic transport in CdSe quantum dot arrays.* PhD thesis, Massachusetts Institute of Technology, 2001.

[75] Nevill Francis Mott and Edward A Davis. *Electronic processes in non-crystalline materials*. Oxford University Press, 2012.

[76] Christopher B Murray, CR Kagan, and MG Bawendi. Synthesis and characterization of monodisperse nanocrystals and close-packed nanocrystal assemblies. *Annual Review of Materials Science*, 30(1):545–610, 2000.

[77] UN Nandi, CD Mukherjee, and KK Bardhan. 1/f noise in nonlinear inhomogeneous systems. *Physical Review B*, 54(18):12903, 1996.

[78] Zhihong Nie, Alla Petukhova, and Eugenia Kumacheva. Properties and emerging applications of self-assembled structures made from inorganic nanoparticles. *Nature nanotechnology*, 5(1):15–25, 2010.

[79] M Nirmal, BO Dabbousi, MG Bawendi, JJ Macklin, JK Trautman, TD Harris, and LE Brus. Fluorescence intermittency in single cadmium selenide nanocrystals. *Nature*, 383(6603):802–804, 1996.

[80] M Niţă, B Ostahie, and A Aldea. Spectral and transport properties of the two-dimensional lieb lattice. *Physical Review B*, 87(12):125428, 2013.

[81] Dmitry S Novikov. *Transport in nanoscale systems*. PhD thesis, Massachusetts Institute of Technology, 2003.

[82] DS Novikov, M Drndic, LS Levitov, MA Kastner, MV Jarosz, and MG Bawendi. Levy statistics and anomalous transport in quantum-dot arrays. *Physical Review B*, 72(7):075309, 2005.

[83] DS Novikov, B Kozinsky, and LS Levitov. Correlated electron states and transport in triangular arrays. *Physical Review B*, 72(23):235331, 2005.

[84] Harry Nyquist. Thermal agitation of electric charge in conductors. *Physical review*, 32(1):110–113, 1928.

[85] Ylva K Olsson, Gang Chen, Ronen Rapaport, Dan T Fuchs, Vikram C Sundar, Jonathan S Steckel, Moungi G Bawendi, Assaf Aharoni, and Uri Banin. Fabrication and optical properties of polymeric waveguides containing nanocrystalline quantum dots. *Applied physics letters*, 85(19):4469–4471, 2004.

[86] Joseph Orenstein and Marc Kastner. Photocurrent transient spectroscopy: measurement of the density of localized states in a-as 2 se 3. *Physical Review Letters*, 46(21):1421, 1981.

[87] Jong-Jin Park, Prem Prabhakaran, Kyung Kook Jang, YoungGu Lee, Junho Lee, KwangHee Lee, Jaehyun Hur, Jong-Min Kim, Namchul Cho, Yong Son, et al. Photopatternable quantum dots forming quasi-ordered arrays. *Nano letters*, 10(7):2310–2317, 2010.

[88] M Pollak and I Riess. A percolation treatment of high-field hopping transport. *Journal of Physics C: Solid State Physics*, 9(12):2339, 1976.

[89] V. J. Porter, T. Mentzel, S. Charpentier, M. A. Kastner, and M. G. Bawendi. Temperature-, gate-, and photoinduced conductance of close-packed cdte nanocrystal films. *Phys. Rev. B*, 73:155303, Apr 2006.

[90] KS Ralls, WJ Skocpol, LD Jackel, RE Howard, LA Fetter, RW Epworth, and DM Tennant. Discrete resistance switching in submicrometer silicon inversion layers: Individual interface traps and low-frequency (1 f?) noise. *Physical review letters*, 52(3):228, 1984.

[91] Franz X Redl, K-S Cho, Christopher B Murray, and Stephen O'Brien. Three-dimensional binary superlattices of magnetic nanocrystals and semiconductor quantum dots. *Nature*, 423(6943):968–971, 2003.

[92] Françoise Remacle and Raphael D Levine. Quantum dots as chemical building blocks: elementary theoretical considerations. *ChemPhysChem*, 2(1):20–36, 2001.

[93] AL Roest, JJ Kelly, D Vanmaekelbergh, and EA Meulenkamp. Staircase in the electron mobility of a zno quantum dot assembly due to shell filling. *Physical review letters*, 89(3):036801, 2002.

[94] Hugo E Romero and Marija Drndic. Coulomb blockade and hopping conduction in pbse quantum dots. *Physical review letters*, 95(15):156801, 2005.

[95] Matthew Rycenga, Pedro HC Camargo, and Younan Xia. Template-assisted self-assembly: a versatile approach to complex micro-and nanostructures. *Soft Matter*, 5(6):1129–1136, 2009.

[96] Walter Schottky. Über spontane stromschwankungen in verschiedenen elektrizitätsleitern. *Annalen der Physik*, 362(23):541–567, 1918.

[97] R Clayton Shallcross, Gulraj S Chawla, F Saneeha Marikkar, Stephanie Tolbert, Jeffrey Pyun, and Neal R Armstrong. Efficient cdse nanocrystal diffraction gratings prepared by microcontact molding. *ACS nano*, 3(11):3629–3637, 2009.

[98] Elena V Shevchenko, Dmitri V Talapin, Nicholas A Kotov, Stephen O'Brien, and Christopher B Murray. Structural diversity in binary nanoparticle superlattices. *Nature*, 439(7072):55–59, 2006.

[99] Elena V Shevchenko, Dmitri V Talapin, Christopher B Murray, and Stephen O'Brien. Structural characterization of self-assembled multifunctional binary nanoparticle superlattices. *Journal of the American Chemical Society*, 128(11):3620–3637, 2006.

[100] Moonsub Shim and Philippe Guyot-Sionnest. N-type colloidal semiconductor nanocrystals. *Nature*, 407(6807):981–983, 2000.

[101] KT Shimizu, RG Neuhauser, CA Leatherdale, SA Empedocles, WK Woo, and MG Bawendi. Blinking statistics in single semiconductor nanocrystal quantum dots. *Physical Review B*, 63(20):205316, 2001.

[102] BI Shklovskii. 1/f noise in variable range hopping conduction. *Physical Review B*, 67(4):045201, 2003.

[103] NE Staley, N Ray, MA Kastner, MP Hanson, and AC Gossard. Electric-field driven insulating to conducting transition in a mesoscopic quantum dot lattice. *Phys. Rev. Lett.*, (Submitted), 2014.

[104] Dmitri V Talapin, Jong-Soo Lee, Maksym V Kovalenko, and Elena V Shevchenko. Prospects of colloidal nanocrystals for electronic and optoelectronic applications. *Chemical reviews*, 110(1):389–458, 2009.

[105] Dmitri V Talapin and Christopher B Murray. Pbse nanocrystal solids for n-and p-channel thin film field-effect transistors. *Science*, 310(5745):86–89, 2005.

[106] Dmitri V Talapin, Elena V Shevchenko, Maryna I Bodnarchuk, Xingchen Ye, Jun Chen, and Christopher B Murray. Quasicrystalline order in self-assembled binary nanoparticle superlattices. *Nature*, 461(7266):964–967, 2009.

[107] Michela Tamborra, Marinella Striccoli, M Lucia Curri, Juan A Alducin, David Mecerreyes, Josè A Pomposo, Nikolaos Kehagias, Vincent Reboud, Clivia M Sotomayor Torres, and Angela Agostiano. Nanocrystal-based luminescent composites for nanoimprinting lithography. *Small*, 3(5):822–828, 2007.

[108] Zhiyong Tang, Zhenli Zhang, Ying Wang, Sharon C Glotzer, and Nicholas A Kotov. Self-assembly of cdte nanocrystals into free-floating sheets. *Science*, 314(5797):274–278, 2006.

[109] Andrea R Tao, Jiaxing Huang, and Peidong Yang. Langmuir- blodgettry of nanocrystals and nanowires. *Accounts of chemical research*, 41(12):1662–1673, 2008.

[110] Emine Tekin, Patrick J Smith, Stephanie Hoeppener, Antje MJ van den Berg, Andrei S Susha, Andrey L Rogach, Jochen Feldmann, and Ulrich S Schubert. Inkjet printing of luminescent cdte nanocrystal–polymer composites. *Advanced Functional Materials*, 17(1):23–28, 2007.

[111] A Tremblay, B Fourcade, and P Breton. Multifractals and noise in metal-insulator mixtures. *Physica A: Statistical Mechanics and its Applications*, 157(1):89–100, 1989.

[112] Jeffrey J Urban, Dmitri V Talapin, Elena V Shevchenko, Cherie R Kagan, and Christopher B Murray. Synergism in binary nanocrystal superlattices leads to enhanced p-type conductivity in self-assembled pbte/ag2te thin films. *Nature materials*, 6(2):115–121, 2007.

[113] Jeffrey J Urban, Dmitri V Talapin, Elena V Shevchenko, and Christopher B Murray. Self-assembly of pbte quantum dots into nanocrystal superlattices and glassy films. *Journal of the American Chemical Society*, 128(10):3248–3255, 2006.

[114] Alfons van Blaaderen. Materials science: Quasicrystals from nanocrystals. *Nature*, 461(7266):892–893, 2009.

[115] D Vanmaekelbergh, AJ Houtepen, and JJ Kelly. Electrochemical gating: a method to tune and monitor the (opto) electronic properties of functional materials. *Electrochimica Acta*, 53(3):1140–1149, 2007.

[116] Richard F. Voss and John Clarke. 1/f noise from systems in thermal equilibrium. *Phys. Rev. Lett.*, 36:42–45, Jan 1976.

[117] D. D. Wanger. *Translating semiconductor device physics into nanoparticle films for electronic applications.* PhD thesis, Cambridge, MA, 2014.

[118] Darcy D Wanger, Raoul E Correa, Eric A Dauler, and Moungi G Bawendi. The dominant role of exciton quenching in pbs quantum-dot-based photovoltaic devices. *Nano letters*, 13(12):5907–5912, 2013.

[119] Conan Weeks and Marcel Franz. Topological insulators on the lieb and perovskite lattices. *Physical Review B*, 82(8):085310, 2010.

[120] Brian L Wehrenberg and Philippe Guyot-Sionnest. Electron and hole injection in pbse quantum dot films. *Journal of the American Chemical Society*, 125(26):7806–7807, 2003.

[121] Brian L Wehrenberg, Dong Yu, Jiasen Ma, and Philippe Guyot-Sionnest. Conduction in charged pbse nanocrystal films. *The Journal of Physical Chemistry B*, 109(43):20192–20199, 2005.

[122] DR White, R Galleano, A Actis, H Brixy, M De Groot, J Dubbeldam, AL Reesink, F Edler, H Sakurai, RL Shepard, et al. The status of johnson noise thermometry. *Metrologia*, 33(4):325, 1996.

[123] Frank W Wise. Lead salt quantum dots: the limit of strong quantum confinement. *Accounts of Chemical Research*, 33(11):773–780, 2000.

[124] Yadong Yin, Yu Lu, Byron Gates, and Younan Xia. Template-assisted self-assembly: a practical route to complex aggregates of monodispersed colloids with well-defined sizes, shapes, and structures. *Journal of the American Chemical Society*, 123(36):8718–8729, 2001.

[125] Dong Yu, Congjun Wang, and Philippe Guyot-Sionnest. n-type conducting cdse nanocrystal solids. *Science*, 300(5623):1277–1280, 2003.

[126] Dong Yu, Congjun Wang, Brian L Wehrenberg, and Philippe Guyot-Sionnest. Variable range hopping conduction in semiconductor nanocrystal solids. *Physical review letters*, 92(21):216802, 2004.

[127] Ni Zhao, Tim P Osedach, Liang-Yi Chang, Scott M Geyer, Darcy Wanger, Maddalena T Binda, Alexi C Arango, Moungi G Bawendi, and Vladimir Bulovic. Colloidal pbs quantum dot solar cells with high fill factor. *ACS nano*, 4(7):3743–3752, 2010.